Study of polymer film formation and their characterization using NMR, XRD and DSC

Dissertation

zur Erlangung des akademischen Grades

doctor rerum naturalium (Dr. rer. nat.)

Vorgelegt dem Rat der

Fakultät für Mathematik und Naturwissenschaften

der Technischen Universität Ilmenau

von

M. Sc. Sushanta Ghoshal

geboren am 31.01.1980 in Dhaka, Bangladesch

Berichter: Universitätsprofessor Prof. Dr. rer. nat. habil. Siegfried Stapf

Promotionskomission

Vorsitzender: **Prof. Dr. Erich Runge**
(Institut für Physik, TU Ilmenau)

Gutachter: **Prof. Dr. rer. nat. habil. Siegfried Stapf**
(Institut für Physik, TU Ilmenau)

Prof. Dr. rer. nat. habil. Uwe Ritter
(Institut für Chemie und Biotechnik, TU Ilmenau)

Prof. Dr. Ioan Ardelean
(Technical University of Cluj-Napoca, Romania)

weitere Mitglieder: **Prof. Dr. Jörg Kröger**
(Institut für Physik, TU Ilmenau)

PD Dr. rer. nat. habil. Paul Denner
(Institut für Physik, TU Ilmenau)

Tag des Einreichung: 05. December 2011

Tag der wissenschaftlichen Aussprache: 07. March 2012

Study of polymer film formation and their characterization using NMR, XRD and DSC

Dissertation

In partial fulfillment of the
requirements for the degree of

doctor rerum naturalium (Dr. rer. nat.)

at the Faculty of Mathematics and Natural Science,

Ilmenau University of Technology

By

M. Sc. Sushanta Ghoshal

Born on 31.01.1980 in Dhaka, Bangladesh

Supervisor: Universitätsprofessor Prof. Dr. rer. nat. habil. Siegfried Stapf

Ilmenau, Germany

To my parents

Untersuchung und Charakterisierung der Bildung von Polymerschichten mit Hilfe von NMR, XRD und DSC

Zusamenfassung

Die Bildung dünner Polymerschichten aus den umweltfreundlichen Polymeren Gelatine, Stärke und Poly(vinylalkohol) (PVOH) wurde mit Hilfe von Kernspinresonanz (NMR), Weitwinkel-Röntgendiffraktometrie (XRD) und Differential-Scanning-Kalorimetrie (DSC) untersucht. Die Proben wurden durch Abguss wässriger Polymerlösungen hergestellt und ihr Trocknungsprozess bei Raumtemperatur mit Hilfe eines unilateralen NMR-Scanners bis zur vollständigen Erstarrung untersucht. Eindimensionale Tiefenprofile mit mikroskopischer Auflösung wurden zu verschiedenen Stadien des Prozesses aufgenommen. Jeder Profilpunkt wurde dabei aus der Summe mehrerer Spin-Echos gebildet. Weiterhin wurden aus der Abnahme der Echointensitäten für jeden Punkt Spin-Spin-Relaxationszeiten (T_2) bestimmt und in Bezug auf den Trocknungsprozess interpretiert. Darüber hinaus wurden Spin-Gitter-Relaxationszeiten (T_1) gemessen. Abhängig vom Typ und der ursprünglichen Konzentration des untersuchten Polymers wurden während der Verdunstung des Lösungsmittels unterschiedliche molekulardynamische Prozesse in verschiedenen Tiefen der Schicht beobachtet. Die Ergebnisse zeigen eine räumliche Inhomogenität der molekulardynamischen Prozesse während der Trocknung. Im fortgeschrittenen Stadium des Trocknungsprozesses beeinflusst diese Inhomogenität die mikroskopische Anordnung der Polymerketten während der Erstarrung und bestimmt somit die endgültige Struktur der Polymerschicht. XRD-Messungen der vollständig erstarrten Schichten bestätigen die von den NMR-Messungen aufgezeigte strukturelle Inhomogenität.

Study of polymer film formation and their characterization using NMR, XRD and DSC

Abstract

Film formation and their characterization of three eco-friendly polymers, namely gelatin, starch and poly(vinyl alcohol) (PVOH) were studied using nuclear magnetic resonance (NMR), wide-angle X-ray diffractometry (XRD) and differential scanning calorimetry (DSC) techniques. Polymer solutions were prepared using water as a solvent followed by casting. The drying process of the cast sample was monitored at room temperature with a single-sided NMR scanner until complete solidification occurred. Depth-dependent NMR profiles with microscopic resolution were acquired at different stages of sample drying. Each profile point was accumulated from the echo decay. Spin-spin relaxation times (T_2) were measured from the echo decays at different layers and were correlated with the drying process during film formation. Additionally, spin-lattice relaxation times (T_1) were determined. Depending on the polymer studied and the initial concentration of each polymer, different types of molecular dynamics were observed at different heights during evaporation of the solvent. The study indicates that each polymer shows a spatial heterogeneity in the molecular dynamics during drying. In the advanced stage of drying process, the microscopic arrangement of the polymer chains during their solidification is influenced by this dynamic heterogeneity and determines the final structure of the film. XRD of the film in its final state confirmed the structural heterogeneity identified by the NMR.

Contents

Chapter 1

Introduction

Who has begun has half done.
Have the courage to be wise. Begin!

Quintus Horatius Flaccus

In this modern era, polymers touch our lives from the daily household materials to the sophisticated artificial heart. According to their origin, polymers can be grouped as natural or synthetic. Synthetic polymers are established and abundantly used mainly due to their low price, availability, physical and chemical properties. However, they are responsible for producing enormous amount of waste in daily life, a problem of ever growing importance to mankind. Furthermore, the future availability of fossil resources, which is the nonrenewable source of synthetic polymer, is said to be restricted within a practical time scale. In contrast, biopolymers originated from natural resources have inherent properties, unique functionality and applicability. Consequently, it is worthwhile to explore the new applications of biopolymers as an alternative of synthetic type petroleum based polymers, which not only will protect the environment but also make use of our most abundant renewable resources. There are two main classes of biopolymers, for example, those which are obtained from the plant origin (cellulose, starch, alginate, etc.) and those which are obtained from the animal sources (gelatin, shellac, chitosan, etc.) [1]-[4].

In our daily life we are exposed to myriad applications of polymer films, for instance, food wrapping, the packaging of various items, protective coating on the surface of materials and so on. Over the past few decades impressive advances have been made in the production and application of these films which are mainly synthetic in nature. In

1

recent years, biopolymer films are showing promising aspects in different applications as mentioned above [3]-[5]. Moreover, films obtained from biopolymers and environmentally friendly synthetic polymers find potential applications even in the biomedical and biotechnological fields. These include biocompatible coatings, thin films for tissue engineering and drug delivery [6]. However, biopolymer films have some inherent properties like hydrophobicity, low mechanical properties and aging which are not suitable for most of their applications [7]-[9]. Widespread works have been performed to diminish these shortcomings by modification of the films for different applications. At the same time, mechanical, thermal, electrical and structural properties of different biopolymer films have been studied [3], [4], [10]. Despite these extensive studies on films, not much attention has been given to studying the film formation process. The drying process during the formation of the polymer film is important because the final structure and the characteristic properties of the film depend on this process [11]. The conformation of the polymer chains, as well as their dynamical properties, change during drying as the solvent evaporates. Note that non-uniform drying takes place in many processes of film formation as it can be seen in different colloidal systems like latex dispersions and paints [12]-[14]. In case of biopolymer, information which can be acquired from the film formation study may have an enormous implication in the application and tailoring of the film.

The aim of this thesis is to study, for the first time to the best of our knowledge, the drying process during the biopolymer film formation using NMR technique. To accomplish this goal, two biopolymers are selected based on their sources. Due to difference in chemical structure and the properties when mixed with water, unlike molecular dynamics during the film formation of these biopolymers is presumed. Firstly, gelatin [15] is chosen which is one of the abundant natural biopolymer from animal origin and has a complex structure. Different amino acids are the repeating unit in this biopolymer. Gelatin forms gel or solution in water when dissolved depending on the initial concentration. Starch [16] is the second biopolymer which is used to study the film formation in this thesis. It is the second most abundant natural biopolymer after cellulose from plant origin having glucose unit as the monomer. On the contrary to gelatin, starch forms suspension when mixed with water.

To study the film formation of a polymer having relatively simple structure compared to the complex structure of the biopolymer, poly(vinyl alcohol) (PVOH) [17], a synthetic but environmentally friendly polymer is chosen. Since the proper modification of the biopolymers is yet to achieve a certain level to compete with the synthetic polymers, increasing interest on the use of eco-friendly synthetic polymers as like as PVOH are developing. PVOH forms viscous solution when it is dissolved in water. In contrast with

gelatin and starch samples, the film formation of PVOH has been studied previously using different approaches [11], [18]-[22].

In this study, low-field nuclear magnetic resonance (NMR) technique is used to follow the drying process in terms of relaxation behavior of the sample. In recent years, low field [23] as well as high field [24]-[26] NMR techniques have been employed to characterize biopolymer gels and films. On the other hand, there are few experimental techniques, for instance, atomic force microscopy (AFM), spectroscopic ellipsometry, X-ray photoelectron spectroscopy (XPS), X-ray diffractometry (XRD) or ultrasound reflection that have been employed in order to follow the film formation of different polymer or inorganic materials [27]-[30], but none of them offers a spatially resolved dynamical information as well as density profiling at the same time which are employed in this study using low-field single-sided NMR scanner. A single-sided NMR scanner combines the open magnets and surface radio frequency (RF) coils to generate a magnetic field to measure an object external to the scanner and inside the object under investigation [31]. In this study, the main advantage of using low-field NMR scanner over the conventional high-field NMR spectrometer is its capability to extract a manifold of information during depth dependent *in situ* film formation study without interrupting the drying process. X-Ray diffractometry (XRD), which is capable of providing information on the structure of the final state of a film at a molecular level, is used to characterize the dried polymer films. The thermal properties of the films are investigated using differential scanning calorimetry (DSC). XRD and DSC studies of the film in its final state strengthen our results as observed during the film formation study using NMR technique.

The structure of this dissertation is as follows.

In chapter 2 the theoretical backgrounds of the methods used in this study are introduced. In this context, firstly, the basic of NMR from the semi-classical point of view is described along with the relaxation mechanism of the nuclear spin system. The particular pulse sequences used in this study are presented. Later on, without going in great detail, the basics of XRD and operational technique of DSC are explained.

Chapter 3 presents a brief introduction of the polymers investigated in this work and the sample preparation techniques. The basic experimental setup of the NMR, XRD and DSC techniques used during the course of the study are then discussed.

In Chapter 4 to 6, the experimental results from investigations of the film formation of three different polymers and their characterizations are presented and discussed. In each case, low-field single-sided NMR scanner was used to follow the real time film formation at a molecular level. Chapter 4 presents observations of gelatin film formation

starting from three different samples based on initial concentrations (1%, 2% and 10% gelatin in H_2O/D_2O). A further gelatin film formation study using high-field NMR along with the DSC technique is then presented. Finally, the effects of concentration and the humidity on the gelatin film studied by NMR, DSC and thermogravimetric analysis (TGA) techniques are illustrated in this chapter. The following Chapter 5 focuses on the film formation of starch using a micro camera and the single-sided NMR technique. In this study, film formation of 1% and 5% starch suspension in water and the dried film characterizations are demonstrated. For poly(vinyl alcohol) (PVOH) film formation study, 25% PVOH solution in H_2O/D_2O was prepared varying the molecular weight of PVOH. These results are described in Chapter 6.

In Chapter 7 the general conclusion on the film formation observed in three different types of environmentally friendly polymers is addressed. A set of brief remarks on areas where further investigations is needed based upon the results are presented at the end.

Chapter 2

Methods and Theoretical Background

*All the effects of Nature are only the mathematical consequences of
a small number of immutable laws.*

Pierre-Simon Laplace

This chapter reviews some general aspects of the techniques closely related to this thesis. In this work, the problems and open questions concerning formation of polymer films and their characterizations, as discussed in chapter 1, are mainly investigated with nuclear magnetic resonance (NMR), X-ray diffractometry (XRD) and differential scanning calorimetry (DSC) techniques. The NMR basics, described in section 2.1 in their general forms, are the basis for the NMR experiments performed throughout this work. More detailed descriptions of the NMR theory could be found in textbooks [32]-[37]. In sections 2.2 and 2.3, the working principles of XRD [38]-[39] and DSC [40]-[42] techniques are discussed, respectively.

2.1 Nuclear Magnetic Resonance (NMR)

Nuclear magnetic resonance (NMR) signal was first successfully observed by two research groups, independently to each other, led by F. Bloch and E. M. Purcell in 1946. Since then, NMR has developed into an indispensable tool to scientists of different branches. It offers non-invasive and non-destructive studies to identify the bulk property of the material without special preparations or unpredictable modifications of the sample caused by the measurement.

Basics of NMR

The nuclear magnetic resonance phenomenon occurs when the sample containing NMR-active nuclei is placed in a static magnetic field and excited by a time-dependent magnetic radio frequency (RF) irradiation. The resonance signal depends on the magnetic properties of the particular nucleus. Most atomic nuclei, assumed to be spherical according to the classical picture, possess angular momentum. Since a spinning charge generates a magnetic field, a magnetic moment (μ) is associated with this angular momentum. The nuclear magnetic moment can be written as

$$\mu = \hbar \gamma I ,\tag{2.1}$$

here $\hbar = h/2\pi$ where h is Planck's constant ($= 6.6256 \times 10^{-34} Js$), I is the angular momentum quantum number or nuclear spin and γ is magnetogyric ratio which is a constant for each nuclide. As stated in Equation 2.1, the nucleus has no magnetic moment when $I = 0$. Only isotopes with an odd number of protons and/or an odd number of neutrons possess nonzero nuclear spin. For this reason, some very common isotopes, such as ^{12}C, ^{16}O and ^{32}S having no magnetic moment, cannot be observed by NMR whereas nuclei having nonzero nuclear spin such as proton ^{1}H, ^{13}C, ^{14}N and ^{19}F are used for the NMR detection. These nuclei adopt $2I+1$ spin orientations when immersed in a magnetic field as explained by the *Nuclear Zeeman Effect*. The orientation can be described by means of a set of magnetic or directional quantum numbers m given by the series, $m = I, (I-1), (I-2)..., -I$.

From now on, attention to nuclei with spins of $1/2$ will be confined to simplify the subsequent discussion, if not mentioned otherwise. For a particular nucleus of $I = 1/2$, there will be two orientations or states, $m = +1/2$ and $m = -1/2$ with nuclear moment aligned with and against the magnetic field (B_0), respectively. The energy of these two states of a spin can be written as

$$E_{+1/2} = -\frac{1}{2}\hbar\gamma B_0 \text{ and } E_{-1/2} = \frac{1}{2}\hbar\gamma B_0 ,\tag{2.2}$$

From which the difference between two adjacent spin energy levels can be calculated as

$$\Delta E = \hbar\gamma B_0 = \frac{h\gamma B_0}{2\pi} ,\tag{2.3}$$

When a sample containing nuclei of $I = 1/2$ (e.g. ^1H or ^{13}C) is placed in a magnetic field (B_0), each spin aligns in one of the two possible orientations as described above. At thermal equilibrium, the number of spins in the lower and upper energy levels, denoted by N^+ and N^-, respectively, are not the same (figure 2.1 (a)).
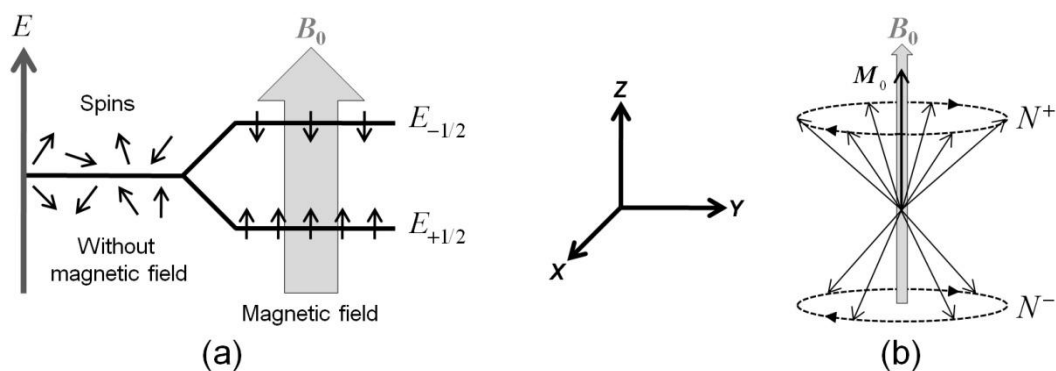

Figure 2.1: (a) *Schematic drawing of the distribution of the nuclear dipoles in absence and in presence of the magnetic field.* **(b)** *Distribution of the nuclear dipoles gives rise to a net nuclear magnetization M_0.*

This distribution of spins can be expressed using the Boltzmann statistics as given below

$$\frac{N^-}{N^+} = e^{-\Delta E/k_B T} \approx 1 - \frac{\Delta E}{k_B T} = 1 - \frac{\hbar \gamma B_0}{k_B T} \ , \qquad (2.4)$$

where k_B is the Boltzmann constant ($= 1.3805 \times 10^{-23} JK^{-1}$) and T is the temperature in Kelvin. From the Equation 2.4, one can observe that the lower energy level is slightly more populated than the higher energy level. This small difference in the number of nuclei/spins is sufficient to allow an NMR signal to be detected which can be favored by a stronger magnetic field (B_0), a larger magnetogyric ratio (γ) and a lower temperature.

According to the classical picture, when placed in a magnetic field, the magnetic moment of a spin precesses on a cone around the field axis z, keeping a constant angle between the spin magnetic moment and the field. Since N^+ is greater than N^-, the net nuclear magnetization M_0, which is the vector sum of the z-components of all the individual nuclear magnetic moments in a sample, aligned parallel to the B_0 field direction (figure 2.1 (b)). In this circumstance there is no transverse (x or y) magnetization (all x-y components averages to zero). The characteristic angular frequency at which a magnetic moment vector of a nuclei in a magnetic field precesses is called the Larmor frequency (ω, in radians/second) which is given by

$$\omega = \gamma B_0, \tag{2.5}$$

This can be transformed into linear frequency (ν_{Larmor}, in Hertz or cycle/second) as

$$\nu_L = \frac{\omega}{2\pi} = \frac{\gamma B_0}{2\pi}, \tag{2.6}$$

A combination of Equation 2.3 and 2.6 gives

$$\Delta E = h\nu_L, \tag{2.7}$$

If an electromagnetic radiation of frequency ν_1 is applied such a way that the resonance condition $\nu_1 = \nu_L$ is fulfilled, then the transitions of the spins between the energy levels can occur as the following Equation is satisfied

$$\Delta E = h\nu_1, \tag{2.8}$$

Absorption of energy occurs during the transition from the lower to the upper energy level whereas those in the reverse direction correspond to an emission of energy. As described before, the number of spins in the lower energy level is higher than the upper energy level which leads to the absorption of energy from the irradiating field as the dominant process. The intensity of the obtained signal (see below) is proportional to the difference of the population of the spins which means that it is also proportional to the total number of spins in the sample. When there is no difference in spin population between the two adjacent energy levels, no signal is observed as the absorption and emission cancel each other which is known as saturation.

The electromagnetic radiation in resonance with the Larmor frequency creates a second magnetic field $\boldsymbol{B}_1$, which is applied to the sample along the direction of x-axis. Because of this radiofrequency (RF) pulse, the net magnetization $\boldsymbol{M}_0$ flips a certain angle on a plane, perpendicular to the direction of $\boldsymbol{B}_1$. This gives rise to components of both longitudinal and transverse magnetization relative to $\boldsymbol{B}_0$. The angle of tipping, α is called the pulse angle which is proportional to the magnetogyric ratio of the nuclei and to the strength and duration of the pulse as given below

$$\alpha = \gamma B_1 \tau_p, \tag{2.9}$$

90° and 180° are the two major pulse angles that are used in the NMR experiments as illustrated in figure 2.2. When the pulse is switched off, the net magnetization M_0 reverts to its equilibrium state (parallel to the B_0 field direction) by the relaxation of the spins. This process involves the discharge of the excess energy which is introduced in to the system by the RF pulse.
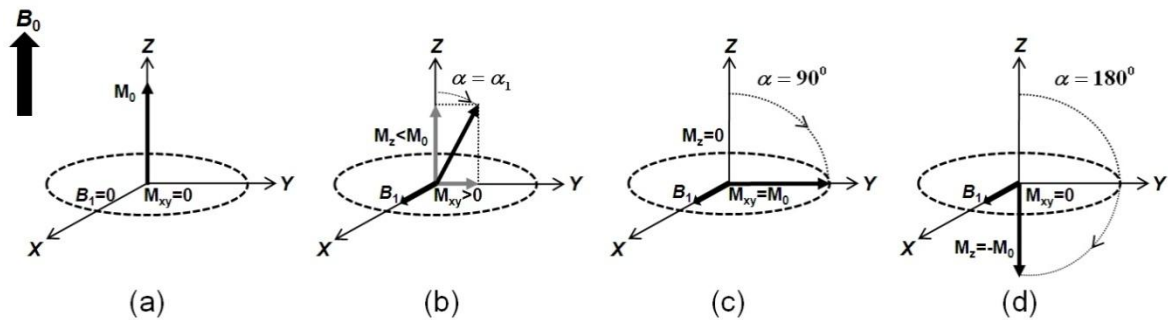

Figure 2.2: *Graphical depiction of the flipping of the net nuclear magnetization M_0 under the influence of radiofrequency pulse at resonance. (a) The net magnetization M_0 is aligned along the external magnetic field B_0 direction and the transverse magnetization component, M_{xy} is zero. (b) and (c) An RF filed B_1 is applied perpendicular to B_0 to tip the net magnetization by 90°. As a result, the longitudinal magnetization component, M_z becomes zero and the transverse magnetization component grows to its highest value. (d) After the 180° pulse, the net magnetization flips to –Z axis.*

In general, there are two types of relaxation process: longitudinal (or spin-lattice) relaxation and transverse (or spin-spin) relaxation characterized by the constants T_1 and T_2, respectively. The decay of the transverse magnetization is known as free induction decay (FID). The signal can be detected in the receiver as the induced voltage which is $\sim dM/dt$, a consequence of precessing (transverse) magnetization. FID is a time domain spectra. Fourier transformation (FT) is applied to the FID in order to observe the spectra in the frequency domain.

Nuclear spin relaxation is caused by the distribution of local interactions experienced by the nuclear spins. In general, the rotational relaxation and translational displacement of nuclear spins influence the relaxation time. The relaxation is a consequence of local fluctuating fields and it can be expressed via the FT of the autocorrelation function of spin vectors.

Spin-lattice relaxation time

The recovery time at which the longitudinal component of the magnetization M_z comes into thermodynamic equilibrium is characterized by the spin-lattice relaxation time,

T_1 (figure 2.3). The value of T_1 covers a broad range depending on the nuclei type, the location of the nuclei (i.e. atom) within a molecule, the size and the physical state of the molecule and the temperature.
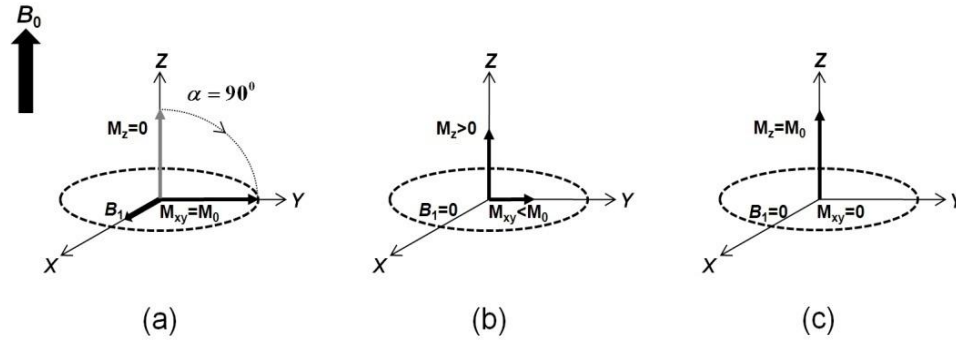

Figure 2.3: *Graphical presentation of the recovery of the longitudinal magnetization, M_z. **(a)** After the 90° pulse, M_z=0. **(b)** and **(c)** Recovery of M_z when the B_1 field is switched off.*

In this work, two common pulse sequences, namely, the saturation recovery and the inversion recovery sequences are used to measure T_1. Two 90° pulses are used for the saturation recovery sequence (figure 2.4 (a)) whereas an initial 180° pulse followed by a 90° pulse is applied in the inversion recovery method (figure 2.4 (b)).
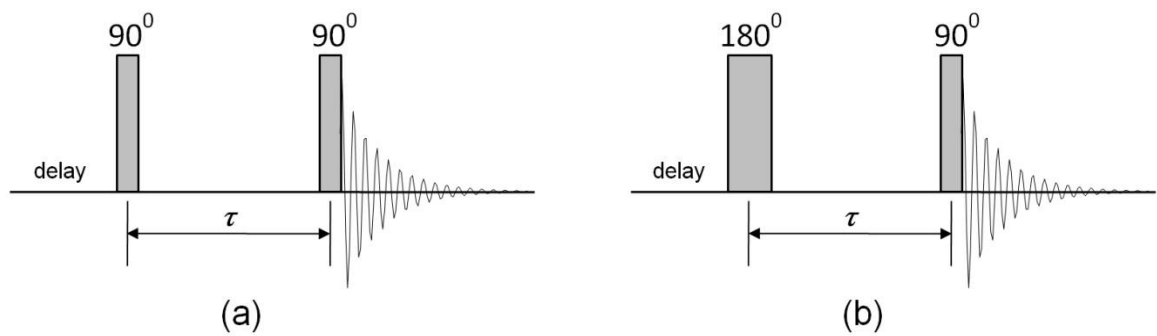
Figure 2.4: *Pulse sequences for measuring T_1 relaxation times using **(a)** Saturation recovery and **(b)** Inversion recovery sequences.*

During the T_1 measurement, the delay time (τ) between two pulses, are varied and the recovery of the corresponding longitudinal magnetizations is recorded. The magnetization recovery can be expressed as

For the saturation recovery: $M_z(\tau) = M_0(1 - e^{-\tau/T_1})$,   (2.10)

For the inversion recovery: $M_z(\tau) = M_0(1 - 2e^{-\tau/T_1})$,   (2.11)

The experimentally obtained magnetization recovery data can be fitted with an exponential function to determine the corresponding T_1 value which is the characteristic time at which 63% of the net magnetization is recovered (figure 2.5).
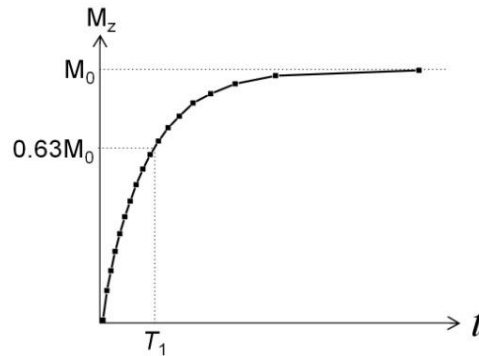
Figure 2.5: *Determination of the T_1 relaxation time.*

During signal accumulation of an NMR experiment, the non-equilibrium steady state at the beginning of an NMR experiment can be avoided by using approximately five times of T_1 as the repetition time.

Spin-spin relaxation time

The net magnetization rotates about the z axis at the Larmor frequency in the transverse (xy) plane following perturbation of the spin system by an RF pulse. At this point, the individual magnetic moments begin to lose their phase coherence due to their spin-spin interaction. The loss of magnetization in the transverse plane is described by the spin-spin relaxation time, T_2 (figure 2.6) which is usually faster than the spin-lattice relaxation time.

Figure 2.6: *Determination of the T_2 relaxation time.*

T_2 can be expressed by

$$M(t) = M_0 e^{-t/T_2},$$ (2.12)

The homogeneity of the magnetic field, the pulse sequence and characteristic properties of the sample may have influence on the T_2 relaxation process. For example, because of the inhomogeneity of the magnetic field, the characteristic transverse relaxation t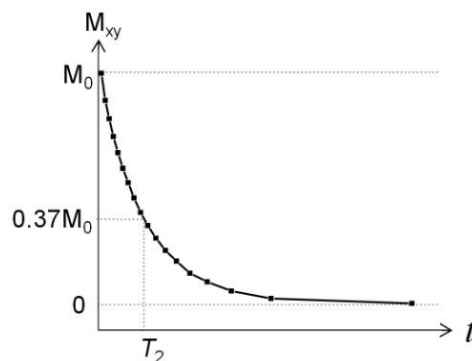ime constant (labeled as T_2^*) differs from that caused by the pure T_2. In presence of the inhomogeneities of the magnetic field, the loss of phase coherence may arise from the diffusion. These effects can be reduced by using the Carr-Purcell-Meiboom-Gill (CPMG) pulse sequence. The CPMG sequence is used in the present work for the determination of transverse relaxation time (more details in section 3.3). The sequence is illustrated below in figure 2.7.
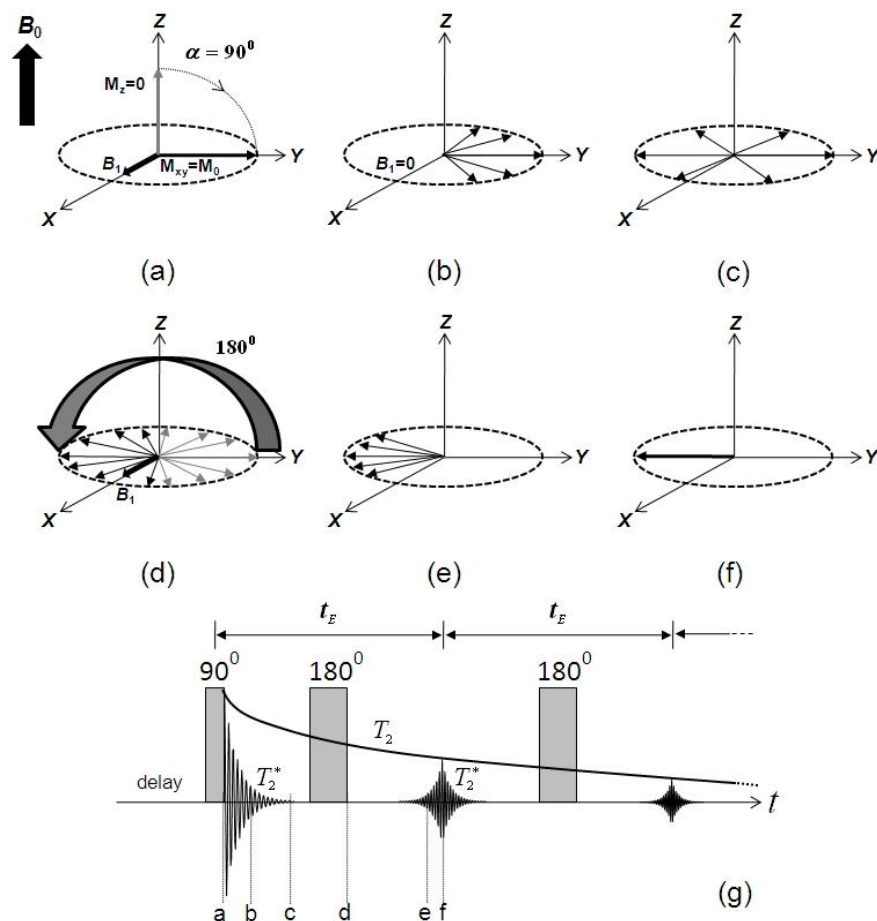
Figure 2.7: *CPMG pulse sequence.* **(a)**, **(b)** *and* **(c)** *represent the formation of FID after the 90° pulse as different spins dephase in time which can be seen in* **(g)**. **(d)** *After the application of the 180° pulse, the spins start to refocus.* **(e)** *and* **(f)** *represent the formation of an echo due to refocusing of the spins. The separation between the echoes is called the echo time t_E. It is twice the separation between the 90° and the first 180° pulse.*

In a strong inhomogeneous magnetic field, the characteristic relaxation time T_2^* of the FID might be very short. In the CPMG sequence, an initial 90° pulse is applied followed by a series of 180° pulses. The successive echoes are formed in between each of the 180° pulse pair and the decay of the amplitude of the direct echo will be dominated by a longer characteristic time constant as can be seen in figure 2.7.

Diffusion

In the present work, the stimulated echo sequence in combination with the static magnetic fixed gradient is used to determine the diffusion coefficient, D. In this pulse sequence, three 90° pulses are used as shown in figure 2.8. The first 90° pulse dephases the spin system. The magnetization is sent back along the z axis when the second 90° pulse is applied. In the delay between the second and third RF pulses, the spins along the z axis do not dephase in the presence of the gradient, because only spins in the transverse plane are affected by the gradient. The third 90° pulse brings the spins into the transverse plane in such a manner that they refocus under the same gradient conditions to form the stimulated echo [43].
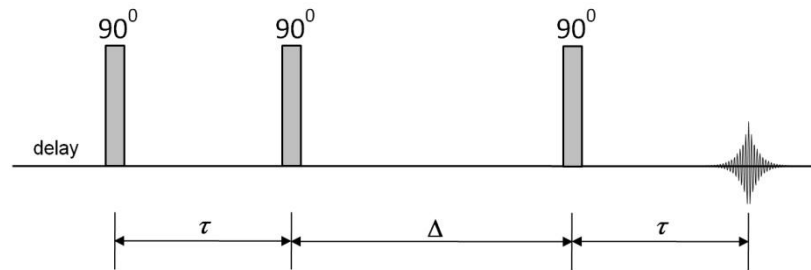
Figure 2.8: *Stimulated echo pulse sequence.*

The diffusion attenuation in the static magnetic fixed gradient can be written as [44]

$$A_{diff}\left(\tau\right) = A \exp\left\{-KD - \left(\frac{2\tau}{T_2} + \frac{\Delta}{T_1}\right)\right\},\qquad(2.13)$$

where $K = \left(\gamma G \tau\right)^2 \left(\Delta + \frac{2\tau}{3}\right)$. γ, G, τ and Δ represent gyromagnetic ratio of the nuclides, gradient strength, encoding time and diffusion time, respectively.

2.2 X-ray Diffractometry (XRD)

The German Physicist Wilhelm Conrad Röntgen discovered X-rays in 1895. It is a high-energy electromagnetic radiation having a wavelength from about 0.001 to 10 nm. However, X-rays used to study the structure of the materials have a narrow range of wavelengths of 0.05 to 0.25 nm. For the production of X-rays, electrons are generated by heating a cathode (e.g., tungsten filament) in a vacuum chamber. These electrons are accelerated towards an anode (e.g., copper) and collide with it at a very high velocity. If the incident electron possesses sufficient energy to eject an inner-shell electron (having lower average energy than that of outer-shell) from the atom of the anode metal, the atom will be left in the excited stage. This inner-shell is filled by an electron from an outer-shell of the atom and an X-ray photon is emitted as the atom returns to the ground state. When an experimental set up is made such a way that the monochromatic X-ray beam hits a sample, it generates scattered X-rays with the same wavelength as the incident beam. The atomic arrangement of the sample is responsible for the intensities and spatial distribution of the scattered X-rays. If the scattered waves are in phase, there is a constructive interference which forms a spatial diffraction pattern in a specific direction. These directions are governed by the wavelength (λ) of the incident beam and the structure of the sample.

The diffraction of X-rays is described by the Bragg's law as given in Equation 2.14 which was formulated by W. H. Bragg and W. L. Bragg in 1913.

$$n\lambda = 2d \sin\theta \ ,$$
(2.14)

Where d is the distance between each adjacent crystal planes (d-spacing), θ is the angle between the incident beam and the particular planes under consideration, also known as Bragg angle. A diffracted peak can be observed when the condition given by the Bragg's law is satisfied. This can be derived using figure 2.9 as below.
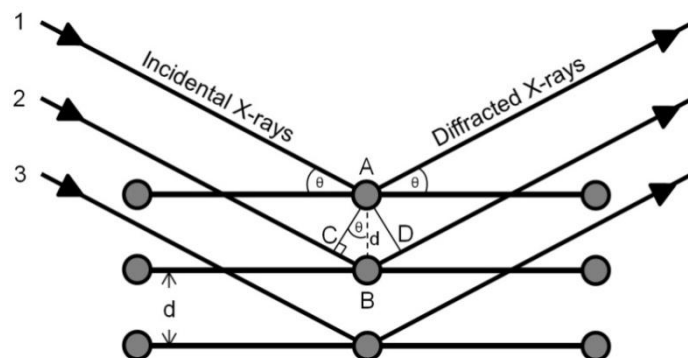

Figure 2.9: *Derivation of Bragg's law showing the diffraction of X-rays.*

As shown in the figure, the top X-ray beam 1, which is in-phase with the beams 2 and 3, is scattered by the atom A when it hits the top layer of the sample. On the other hand, the beam 2 goes deeper until it strikes the atom B and scattered as well. The second beam travels extra distance (known as path difference) of $CB + BD$ which is equal to $2d\sin\theta$ if the beams 1 and 2 are to continue to travel parallel in the same direction. Now the criterion for the existence of the diffracted wave is that the scattered X-rays should all be in phase. For this, the path difference $CB + BD$ must be equal to an integral number (n) of the wavelength (λ) of the incident beam. This is the Bragg's law as stated in (2.14). The angle between the incidental beam and the diffracted beam is 2θ which is usually measured during the experiment. Depending on the lattice planes of the crystal structure, diffracted X-rays produce constructive interference at a certain Bragg angle. Different crystal planes in a lattice can be described by Miller indices which are represented by three integers (hkl).These indices are important for the interpretation of X-ray diffraction pattern.

X-ray diffraction peaks can be used to determine the size of small crystallite in the sample. The expression is known as Scherrer Equation which is given by

$$L = \frac{k\lambda}{B\cos\theta},$$ \hfill (2.15)

Where L is the average crystallite size measured in a direction perpendicular to the surface of the specimen, λ is the wavelength of the X-ray used, B is the full width at half maximum (FWHM) of the characteristic crystalline peak, θ is the Bragg angle and k is the Scherrer constant. k has been determined to vary between 0.89 and 1.39, but is usually taken as close to unity.

2.3 Differential Scanning Calorimetry (DSC)

DSC is the most widely used thermal analysis technique available which provides quantitative calorimetric measurements of the sample. Determination of the characteristic thermal properties of the materials, for example, glass transition (T_g), crystallization (T_c) and melting (T_m) temperature are among the main applications of DSC. It is widely used for sample purity determination, characterization of the thermosets, measurements of liquid crystal transition. In this technique, the energy changes are measured that occur when a sample is heated, cooled or held isothermally, together with the temperature at which these changes occur.
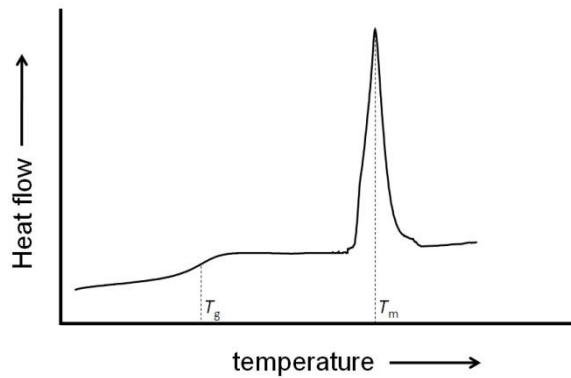
Figure 2.10: *A typical DSC plot where T_g and T_m are the glass transition and melting temperature, respectively.*

During the DSC measurement, two types of pans, namely, a sample pan and a reference pan are used in the sample holder. Generally the reference pan is kept empty where as the sample to be analyzed is placed in the sample pan. Using the computer controlled heater, both the pans can be heated exactly at the same rate throughout the experiment. Because of the sample content, flow of heat to the sample pan will be different than the reference pan to maintain the same temperature in the both pans. At a certain temperature the required heat flow for the sample pan depends on the thermal properties of the sample. The DSC curve is acquired from the difference in the heat flow rate to the sample and the reference while they are subjected to a controlled temperature program. A typical DSC experimental curve showing the glass transition (T_g) and melting temperature (T_m), two characteristic thermal parameters of the sample mainly studied in this work, is illustrated in figure 2.10.

Chapter 3

Experimental

I didn't think; I experimented.

Wilhelm Röntgen

This chapter consists of a short description of the polymer materials used in this work (section 3.1), followed by the sample preparation techniques (section 3.2). Afterwards, the single-sided NMR scanner, the low field NMR instrument mainly used to study the polymer film formation and the data acquisition process are described in brief along with the other NMR, XRD and DSC instruments which are used in this study (section 3.3).

3.1. Materials

3.1.1. Introduction of the polymers

Gelatin

Gelatin is a water-soluble protein which is a hydrolyzed product of collagen. Similar to the cellulose of plants, collagen is the abundant protein constituent in the animal kingdom. The collagen structure consists of three distinct polypeptide chains, each twisted in a left-handed helix (α chain) of about 0.9 nm pitch which are supercoiled together to form a right-handed triple-helix with a pitch of about 8.6 nm. This triple-helix structure is stabilized mainly by the intra and inter chain hydrogen bonding, close van der Waals

interactions and covalent crosslinking. The hydrogen bonding may be either between –CO and –NH groups or between two –CO groups of two polypeptide backbones. Each of the polypeptide chains consists of a repeating motif, Gly-Xaa-Yaa, where Gly is the Glycine, Xaa and Yaa may be any amino acid residue. However, proline and hydroxyproline are most frequently found in the Xaa and Yaa position. The subunit of collagen is called "tropocollagen" which is approximately 300 nm long and 1.5 nm in diameter. Gelatin is a denatured collagen which means that the preparation of gelatin involves the breaking of the collagen tertiary triple-helix structure (γ chains) and the secondary structure (β chains) by the disruption of the hydrogen bond. The primary structure (α chains) of the protein survives in this case to form a random coil configuration of gelatin. For this reason gelatin can be considered as a more disordered or amorphous state of collagen lacking either partially or completely the tertiary and secondary structures. Nevertheless, amino acid sequences of gelatin are almost identical to the parent collagen. Both collagen and gelatin contain 18 different amino acids in their structure [45]-[46].
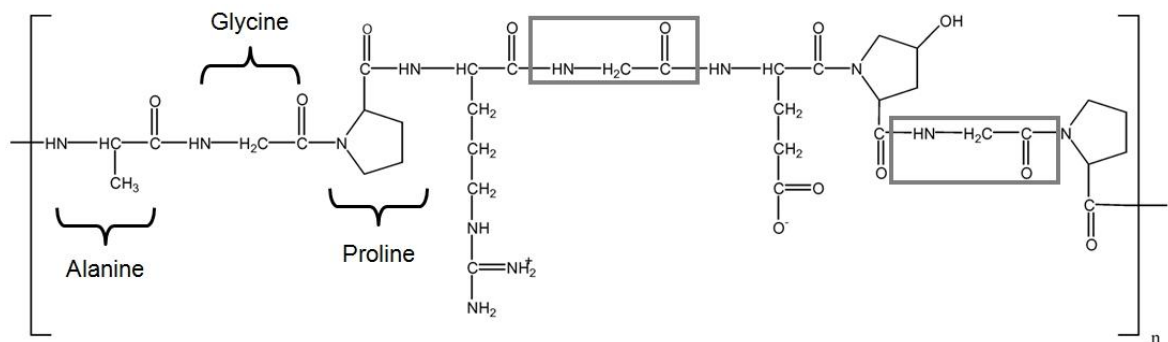
Figure 3.1: *Chemical structure of gelatin [47] showing different amino acids as the monomers and the repetition of glycine in the repeating motif.*

Gelatin is extracted from the skin, bones, hides and other organs of animals. The number average molecular weight (M_n) and the weight average molecular weight (M_w) of non-hydrolyzed gelatins can be ranged from $5 \times 10^4 - 1 \times 10^5$ g/mol and $10^5 - 10^6$ g/mol, respectively. There are two types of gelatin available in the market depending on the method of hydrolysis used during the conversion of collagen into gelatin which can be done using an acid (type A gelatin) or a base (type B gelatin). Commercially available gelatin is characterized by the Bloom strength which varies from 30 to 300. Bloom strength represents the gel strength of gelatin [48]. Gelatin normally contains 12-15% water, 1-4% inorganic salts and trace amount of grease [15].

Gelatin is an extensively studied and well characterized biopolymer. It is of great interest to various fields which include food industry (as an edible film, in different food products), pharmaceutical industry (as a binder in tablet, in hard and soft capsule shell

production), biomedical field (for wound dressing, three-dimensional tissue regeneration, adsorbent pads for surgical use, microspheres, sealants for vascular prostheses) and leather industry (in tanning). The wide interest behind the increasing use of the gelatin film is due, to a large degree, to its suitable mechanical properties combined with biocompatibility, biodegradability and moisture sensitivity [4], [49]-[50].

Starch

Starch biopolymer is an extremely abundant polysaccharide from the plant source which consists of glucose (D-glucopyranose) unit, the only monomer presents in the starch with two main constituents, amylose (figure 3.2 (a)) and amylopectin (figure 3.2 (b)) and two connecting glycosidic $\alpha-(1\rightarrow4)$ and $\alpha-(1\rightarrow6)$ linkages that construct the polymer backbone and branching points, respectively [51].
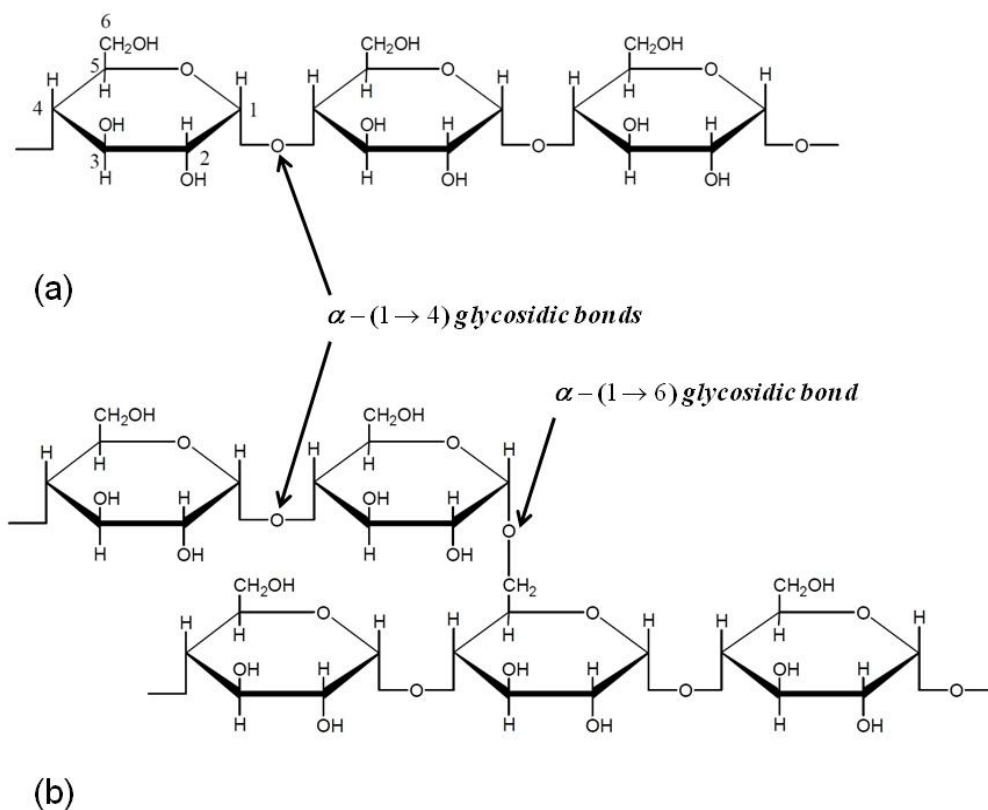

Figure 3.2: *Molecular structures of* **(a)** *amylose and* **(b)** *amylopectin [52].*

Amylose (molecular weight 10^4-10^6 g/mol) is defined as the linear molecule which contains $\alpha-(1\rightarrow4)$ linkage with some slightly branched molecules by $\alpha-(1\rightarrow6)$ linkage. On the other hand, Amylopectin (molecular weight 10^6-10^8 g/mol) is the highly

branched component of starch which is composed mostly of $\alpha - (1 \rightarrow 4)$ D-glucopyranose units with $\alpha - (1 \rightarrow 6)$ linkages at intervals of approximately 20 units [53].

Starch can be found in various parts of a plant, such as seeds, leaves, roots, tubers and the fruit pulps. Based on plant origin or source, there are different kinds of starch, for example, corn or maize starch, potato starch, rice starch, wheat starch etc. The ratio of amylose to amylopectin in the starch granules varies with the plant source. However, the amylose content in the commercially available starch granules is 20-30%. There are some amylose-rich starches, for example, rice, wrinkled pea having amylose content of over 50%. Proteins (up to 0.3%), minerals and lipids (up to 1.0%) are the other components which are present in starch in very small quantities and have minor effect on starch properties. Native starch granules have a crystallinity which varies from 12-45% [16]. Amylopectin mainly forms the semi-crystalline zone in the starch granules which consists of ordered double helical lamellar structure and rigid amorphous branching zones. Some of the amylose may take part in this semi-crystalline zone by the formation of double helices with amylopectin side chains [51], [54]. On the other hand, both amylose and amylopectin contribute to the random ordered amorphous zone [55]. Depending on the origin, the native starch has three crystalline patterns. For example, most cereal starches have the so-called A-type pattern whereas B-type pattern appears in some tuber and cereal starches rich in amylose. Legume starches generally give a C-type pattern. A-type pattern has relatively more dense packed double helices than the B-type [16].

Application of starch film is steadily emerging, including biodegradable packaging materials, as an alternative coating material in the food industry, barrier against gases (O_2, CO_2), in the pharmaceutical industry as a carrier and so on [56]. Films prepared by the starch are often very fragile. Hence, low molecular plasticizers such as polyols are used to decrease interactions between the polymer chains [57]-[59]. The mechanical properties such as tensile, bending and elongation properties of the film depend on starch source, amylose-amylopectin ratios, moisture and plasticizer contents and film formation parameters such as initial concentration, temperature, film formation time and relative humidity.

Poly(vinyl alcohol) (PVOH)

There is a small number of synthetic polymers which are known for their environment friendly behavior. Poly(vinyl alcohol) (PVOH), synthesized by Herrmann and Haehnel in 1924, is one of those synthetic polymers which is biodegradable, biocompatible and possesses good mechanical properties [60]. It is obtained from the partial or complete hydrolysis of polyvinyl acetate. PVOH thermally degrades at about 150

°C although the crystalline melting point is 180-240 °C [61]. Poly(vinyl alcohol) is a tasteless, odorless hydrophilic polymer. In the solution it forms inter- and intramolecular hydrogen bonds between –OH groups which is available in its monomer unit (figure 3.3). Although PVOH is an atactic linear polymer which means the position of the –OH group in the side chain is random, it is crystalline in nature as the small size of the –OH group does not disrupt the crystalline lattice structure [17].
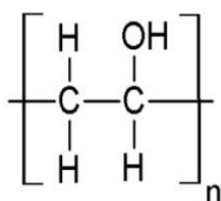

Figure 3.3: *Molecular structure of poly(vinyl alcohol) showing three non-exchangeable protons (^1H) in the main chain and one exchangeable (labile) proton in its structure.*

Commercially available PVOH has a broad range of hydrolysis and degree of polymerizations which open the field of versatile applications in fibres, cosmetics industry, adhesives, textile and paper sizing, asbestos alternatives, in pharmaceutical and biomedical materials [62]-[64]. PVOH is a good film forming polymer which has applications in different industrial sectors, for instance, as a high oxygen barrier film, membranes, packaging materials and polarizing film as PVOH-iodine complex. It is also readily blended with a number of natural materials, for example, gelatin, starch, chitosan and alginate for new applications [65]-[67].

3.1.2. Materials used in this study

Gelatin

Gelatin from porcine skin containing 12-14% moisture (calculated from dry weight basis) was used as received from Carl Roth GmbH + Co., Germany. It is an extra pure A type gelatin (140 bloom), i.e. it is obtained from acid treated collagen. As shown in figure 3.4, it is a granular solid having a faint yellow color.

Starch

To study the film formation, maize (or corn) starch was chosen which is the most common starch produced (more than 80% in the world market [55]) for different

applications. Unmodified extra pure corn starch (Carl Roth GmbH + Co.) containing 13% moisture (dry weight basis) was used to follow the film formation in this work.

Figure 3.4: *Polymer samples* **(a)** *Gelatin* **(b)** *Starch* **(c)** *Poly(vinyl alcohol).*

Poly(vinyl alcohol)

PVOH (MOWIOL grade) was obtained from Sigma-Aldrich, Germany and used without further purification. Three different molecular weights of PVOH, 27000, 61000 and 125000 were used in this study with a degree of hydrolysis > 98% for all the samples. All the samples contain around 15% of moisture which was calculated from dry weight basis.

Water (H_2O)

In this study, water was used as the solvent of choice due to its ability to make solution/suspension with the studied polymers. Mono distilled water was obtained from the GFL-2002 water distillation unit (Gesellschaft für Labortechnik mbH, Germany) and used to dissolve the polymer samples.

Deuterium oxide (D_2O)

Deuterated water was used as a solvent in order to selectively follow the dynamics of the backbone of the polymer molecules during the NMR experiments. D_2O (100 atom-% D) was purchased from Chemotrade, Chemiehandelsgesellschaft mbH, Leipzig, Germany and Carl Roth GmbH + Co., Germany.

Glycerol

Anhydrous glycerol (Merk-Schuchardt, Germany) was used as a plasticizer. It is a monosaccharide-based polyol which is widely used as a plasticizer due to its low molecular weight in edible film applications. In the starch film, it is used to enhance the flexibility and elasticity of the film as well as to prevent pore and crack formation [57].

3.2. Methods

3.2.1. Sample preparation

Drying of the samples

All the polymer samples contain a certain amount of moisture which can contribute to the total NMR signal and was removed by oven-drying at 105 °C. This treatment was important especially for the NMR experiments where D_2O was used as a solvent to obtain NMR signal only from the NMR sensitive nuclei of the polymer. The weight of the polymer was measured periodically using a micro balance (Sartorius MC1 AC 210P, Data Weighing Systems, Inc., USA) during this treatment until a constant weight was achieved. Each sample was then kept in a desiccator in moisture free atmosphere at ambient temperature for storage.

Gelatin sample

Solvent (D_2O or H_2O) was added to a precalculated amount of desiccated gelatin to prepare the gelatin-D_2O or gelatin-H_2O solution of different initial concentrations (w/v). A hot plate containing a magnetic stirrer (RH basic 2, IKA-Werke GmbH & Co. KG, Germany) was employed for one hour (h) to obtain a homogeneous mixture at 50 °C with the beaker being covered completely (but not sealed) during this period in order to avoid H-D exchange with the air humidity for the D_2O containing sample and to reduce the effect of increase in concentration due to evaporation for both of the samples.

Starch sample

Aqueous dispersions of 1% and 5% (w/v) corn starch were prepared in presence of glycerol (20g/100g of starch) plasticizer. The protocol for sample preparation is the following: precalculated amount of starch and solvent (D_2O or H_2O) mixture was heated and stirred at 70 °C for 40 minutes (min) in the covered beaker to obtain a homogeneous mixture. The starch dispersion was then heated to nearly 95 °C and kept in this temperature for about 20 min to allow gelatinization. It was seen that the 1% starch containing sample forms precipitation when it is allowed to cool without agitation. On the other hand, 5% starch sample forms a white gel [68]. Consequently, both samples were

agitated to maintain a homogeneous mixture until the sample temperature was reduced to about 40 °C and cast afterwards.

Poly(vinyl alcohol) (PVOH) sample

For the preparation of the samples, either water or deuterium oxide was added to a precalculated amount of desiccated PVOH to prepare the 25% (w/v) PVOH-H_2O or 25% (w/v) PVOH-D_2O solutions, respectively. In order to obtain a homogeneous mixture and to avoid local gelation, each of the PVOH samples was heated and stirred at 90 °C for one h, with the beaker being covered completely during this period. Following this step, the covered beaker containing the homogeneous mixture was placed in an oven and was kept at the same temperature for further 5 h to eliminate air bubbles. The viscous solution was then ready to cast.
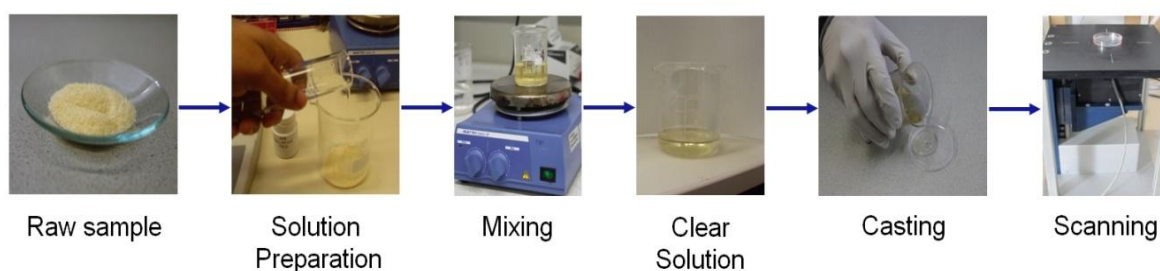

Raw sample → Solution Preparation → Mixing → Clear Solution → Casting → Scanning

Figure 3.5: *Illustration of the sample preparation and casting in general.*

3.2.2. Casting

One of the most popular methods for the preparation of polymer film is solution casting which involves two main steps, namely, preparation of the solution using an appropriate solvent at a temperature above the melting temperature and then to spread the solution evenly on a suitable non-adhesive smooth, flat and level substrate for a certain drying time. The film structure is grown as a result of solvent evaporation with time which depends mainly on the temperature and air humidity of the environment. Film preparation by casting solution on flat surfaces is adequate for laboratory test and in some cases for batch productions [4]. Polystyrene Petri dish of 55 mm diameter, which is non-adhesive to the studied polymers, was used to cast the samples. This allows pill-out the dry film once is formed and performed further NMR, XRD and DSC studies. All cast samples were kept at the same room humidity and temperature (40±5% RH, (21±2) °C) and characterized using different techniques.

3.3. Instrumentation

Single-sided NMR scanner

The polymer film formation was followed using a single-sided NMR scanner which is so-called profile NMR MOUSE (MObile Universal Surface Explorer, ACT GmbH, Germany). In this sensor, four permanent magnet blocks are positioned on a ferromagnetic base plate. The magnetic field is inhomogeneous but possesses a well-defined constant field gradient of 11.5 T/m along only Y direction (with the other directions being negligible). A magnetic field B_0 at a certain height above these magnets in the Z direction (parallel to the surface) is created which is known as sensitive volume (figure 3.6) having a sensitive area of about 10 mm by 10 mm. The device is operated at the proton (^{1}H) Larmor frequency of 11.7 MHz. When the RF pulse is applied, the second magnetic field B_1 in the xy plane is created by a surface RF coil of about 10 mm by 10 mm which is integrated to a resonate circuit tuned to 11.7 MHz [69].
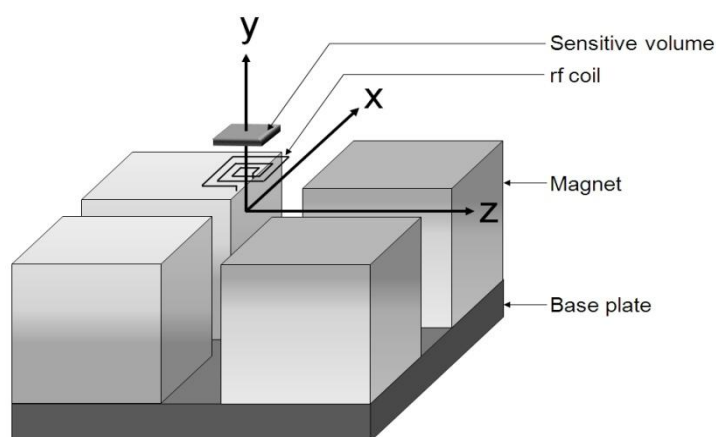
Figure 3.6: *Scheme of the magnet geometry of the profile NMR-MOUSE showing the surface RF coil and the sensitive volume. The direction of polarization of the magnetic field is indicated by the gray scale.*

Spacers of different thicknesses can be used to change the distance between the magnet and the RF coil. The choice of accessible sample height depends on the thickness of the spacer. Most of the measurements of this work were carried out using the thickest available spacer of 9 mm which has the minimum distance between the sensitive volume and the coil and allows an accessible vertical range of 2.1 mm. The Petri dish containing the precalculated amount of aqueous polymer sample was placed on a fixed platform on top of the movable sensor to follow the film formation process. The detailed experimental set up is illustrated in figure 3.7. When the magnet is moved to the vertical

(a)   (b)

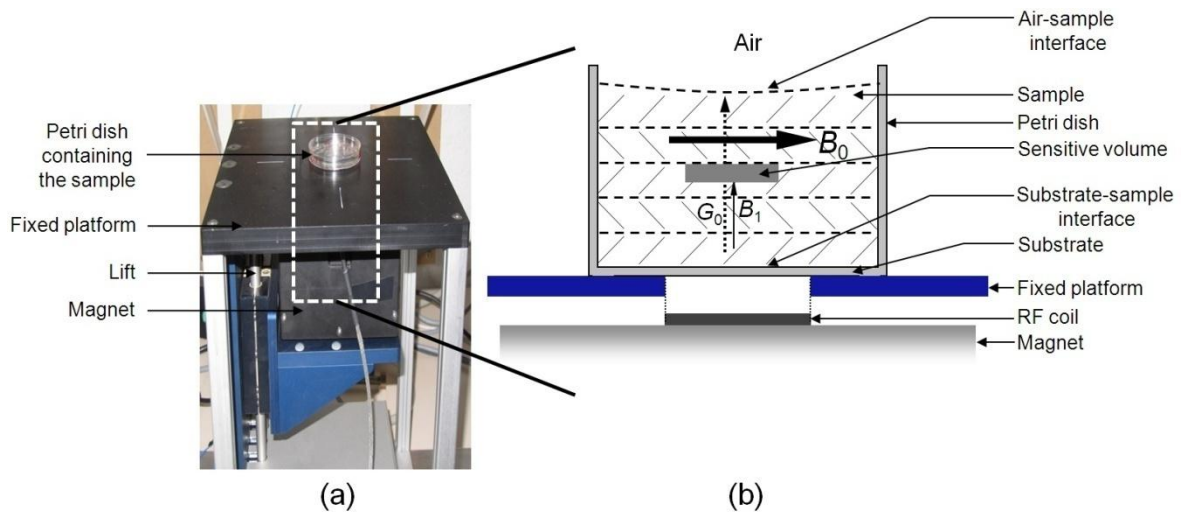**Figure 3.7:** *Illustration of the experimental set up **(a)** Petri dish containing the sample is placed on top of the profile NMR-MOUSE **(b)** Scheme showing the different layers of the sample.The sensitive volume remains at a fixed distance from the magnet (**B_0**, magnetic field; **B_1**, radiofrequency field; **G_0**, magnetic fixed gradient).*

(a)   (b)

                                             (c)
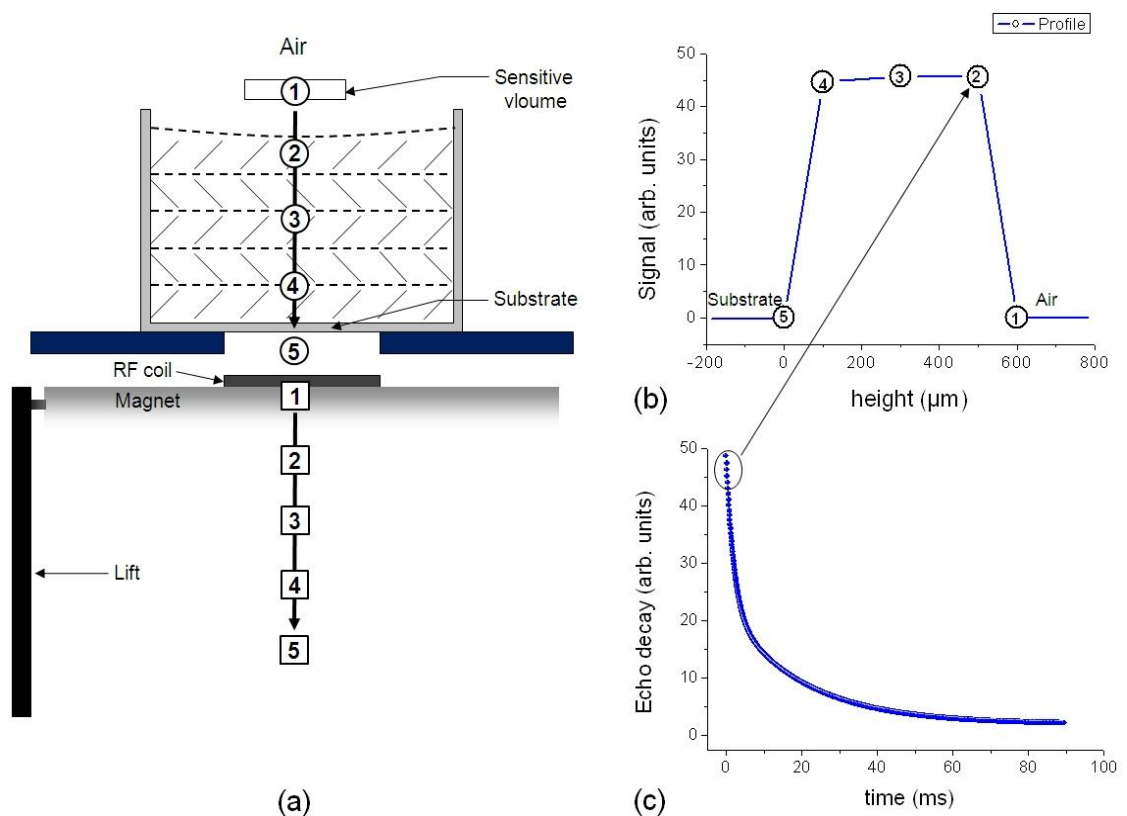
Figure 3.8: *Scheme showing the formation of the profile **(a)** When the magnet is moved along with the RF coil in preset steps (shown by the numbers in boxes), the sensitive volume moves in the same direction and distance (shown by the numbers in circles). The direction of scanning is from top (air-sample interface) to bottom (substrate-sample interface). **(b)** The profile is obtained when the sensor receives a signal from the sample. For example, in the position 2,3 and 4, the sensitve volume is inside the sample giving the rise of the signal while it can not acquire any signal in the position 1 (in the air) and 5 (in the substrate/platform). Each point of the profile is the sum of the area of the preset number of echos obtained from the echo decay **(c)** using the CPMG pulse sequence.*

direction using a precision lift controlled by a step motor, the RF coil as well as the sensitive volume move accordingly through the sample and a profile [70] can be obtained (figure 3.8). Because of the inhomogeneity of the magnetic field (section 2.1), the characteristic transverse relaxation time T_2^* of the FID is very short (in the order of few µs) and cannot be detected in this scanner. Instead, with the application of Carr-Purcell-Meiboom-Gill (CPMG) pulse sequence (section 2.1 and [71]), one can overcome this problem because the FID is refocused at a time that is longer than the dead time. Hence, the CPMG pulse sequence was applied to obtain the vertical profiles and to accumulate T_2-weighted echo trains by moving the scanner relative to the sample as well as to measure the effective time of echo decays. Accordingly, T_2 relaxation time data obtained from the single-sided scanner will be considered as the effective T_2 time. In the scanner, the resolution is set by controlling the acquisition time T. This approach requires to set the RF pulse to the shortest duration to maximize the excited region and then to set the acquisition time to achieve the desired resolution inside the excited slice (by acquiring signal during a time T the frequency resolution in the spectrum is $\Delta v = 1/T$). The thickness of the selected slice is $\Delta z = 2\pi\,\Delta v\,/\,\gamma G$, where γ and G are the magnetogyric ratio and field gradient, respectively [31], [72]. For the slice thicknesses of 30, 50, 100, 200 and 300 µm, the 180° pulse separation is set to 114.5, 87.5, 66.5, 56.5 and 53.5 µs, respectively, in this work.

For the profile measurements, the position of the sensor was moved in steps of 100 µm with a slice thickness of 100 µm or 50 µm from the beginning. Each point in the profile corresponds to the sum of the area of the second to fifth echo. Necessary echoes were acquired for computing the transverse relaxation times T_2 layer by layer. The signal decays, thus obtained, for each point in the profile followed either single (Equation 3.1) or double exponential (Equation 3.2) behavior and were fitted accordingly to determine T_2.

$$S(t) = A\exp(-t/T_2)\,,\tag{3.1}$$

$$S(t) = A_{short}\exp(-t/T_{2,short}) + A_{long}\exp(-t/T_{2,long})\,,\tag{3.2}$$

where $S(t)$ is the area under the echo signal.

The waiting time between pulse trains, as well as the number of repetitions, was adjusted according to the longest T_1 at a particular time in the experiment, in order to keep the signal unaffected by longitudinal relaxation weighting and maximizing signal-to-

noise ratio for a given experimental run. This is due to the fact that the signal intensity is proportional to $[1 - \exp(-t_{rep}/T_1)]$. If the repetition time (t_{rep}) is long enough, the T_1-contrast [73] is suppressed, and in consequence the signal intensity at different times of the drying process is not affected. A saturation recovery pulse sequence $[90° - \tau - 90°]$ (section 2.1 and [74]) was used with 18 τ values (logarithmically spaced) and CPMG sequence for acquisition [70] for determining the T_1 value. The number of steps for each profile was reduced with drying time accordingly with the reduction of the thickness. This permits more acquisition without increasing the time necessary to make a complete profile. T_2 values of the fully dried films were also measured as a function of height using CPMG pulse sequence in separate experiments. The 90° RF pulse length was set to 3.5 µs.

For the diffusion measurements, the stimulated echo sequence (section 2.1 and [75]) in combination with the static magnetic gradient of the sensor was used. For this measurement, if not mentioned otherwise, an encoding time τ = 0.0055 to 1.9 ms, diffusion time Δ = 2 ms, repetition time of 3 s to 5 s depending on the sample were used. All experiments were performed at room temperature. The temperature of the magnet was followed during the whole process, possessing a variation of ± 0.5 °C. At the position of the sample, a minor increase in the temperature was detected due to the heating of the RF coil. This heating was well below 0.5 °C.

Bruker minispec

The Minispec unit (Bruker Optics, Germany), a commercial low-field NMR instrument operating at 40 MHz ^{1}H Larmor frequency and equipped with a temperature controller, was used to perform the proton relaxation measurements. This instrument provides a simple tune-up system and a monotonically decaying on-resonance real FID with negligible contributions in the imaginary part can be obtained with the proper adjustment of the 90° pulse length, offset and receiver phase [76]. The samples were measured using sealed 8 mm NMR tubes avoiding both evaporation and proton exchange with the atmospheric humidity. To ensure sufficient magnetic field homogeneity, the midpoint of the sample was adjusted to the center of the RF coil. All measurements were carried out at (21.5 ± 0.5) °C. An inversion recovery pulse sequence $[180° - \tau - 90°]$ (section 2.1 and [77], [78]) was used with 30 τ values (logarithmically spaced) to measure the spin-lattice relaxation time (T_1). The spin-spin relaxation time (T_2) was obtained applying the CPMG pulse sequence with a 90° - 180° pulse separation of 40 µs at a 180° pulse width of 3.5 µs. The number of points, corresponding to number of echoes and the number of scans were varied depending on the nature of the sample analyzed.

FIeld cycling relaxometer

The Stelar SPINMASTER FFC2000 relaxometer was used to obtain spin-lattice relaxation times, T_1 over a wide range of Larmor frequency. The curves of T_1 in function of frequency are called T_1 relaxation dispersion. In this method, the sample is polarized at a polarization magnetic field B_p for a time τ_p (figure 3.9) enough for the nuclear magnetization to reach the saturation. The relaxation process then takes place after the fast switching τ_{s1} to a lower magnetic field B_r (relaxation field) in the interval time labeled as τ_r. At the end, the magnetic field is switched to a value of the higher acquisition field B_{aq} and the signal is acquired after a 90° RF pulse which has a frequency $\omega = \gamma B_{aq}$. At a certain magnetic field T_1 relaxation time is acquired by varying the time interval τ_r. By this way, T_1 relaxation dispersion is obtained by changing the field B_r and measuring the corresponding T_1 relaxation time [79].
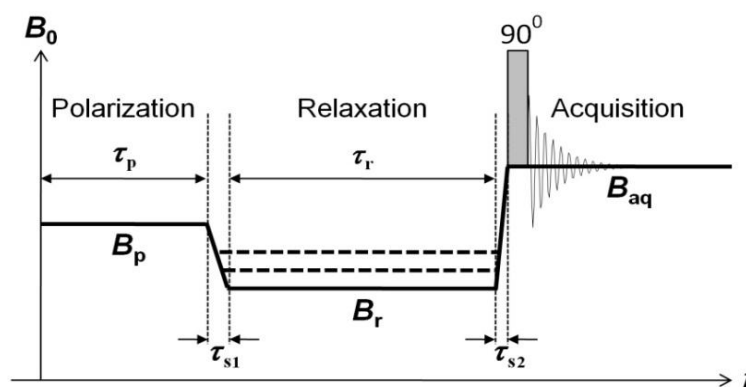
Figure 3.9: *Schematic representation of a typical cycle of the main magnetic field B_0 employed with field-cycling NMR relaxometry, where τ_{s1} and τ_{s2} represent the switching times to decrease and increase the magnetic field, respectively.*

The relaxation dispersions obtained in this study were measured in the interval between 10 kHz and 20 MHz proton resonance frequency. All measurements were carried out at (20.0 ± 0.5) °C.

X-ray diffractometer

The XRD patterns were acquired with a Philips X´Pert PRO diffractometer, equipped with a wide-range PW 3050/6X goniometer which is capable to measure

0.001°/step. The calibration was carried out prior to each of the measurements and a minimum offset for Ω (incident angle) and 2θ (diffraction angle) were achieved. The experiment was carried out at room temperature using Cu K-α radiation (λ = 0.154 nm) generated at a voltage of 35 kV and 30 mA current. The sample was scanned between 2θ = 1.5 to 60° (for most of the samples) with a step size of 0.050°, scanning speed of 2°/min and a count time of 100 s per point. Structural details of the polymer films were examined by comparing the XRD pattern of both sides of the same film. The fixed angle incident beam method was mainly used for this kind of experiments where Ω = 0.5° was fixed throughout the experiment. Powder diffraction spectra were collected as well to characterize the raw polymer samples. Prior to the measurements, the sample was stored in the same environmental conditions as employed for the NMR experiments.

Differential scanning calorimeter

Differential scanning calorimetry (DSC) curves of the polymer samples were recorded with a DSC 7, TAC7/DX instrument (Perkin Elmer, USA) equipped with liquid nitrogen cooling accessory. The transition temperature and enthalpy were calibrated using indium standard. Each sample (5-8 mg) was accurately weighted into a 30 μl or 50 μl standard aluminum pan containing the cover. The pan was perforated by a sealer. The measurements were performed at different temperature ranges and rates as it will be described in the corresponding sections.

Micro camera

A digital microscopic camera (Somikon, Pearl Agency Allgemeine Vermittlungsgesellschaft mbH, Germany) was employed to capture real time frames at a rate of 30 frames/h. In case of gelatin, a series of frames showing the reduction of the sample height until the formation of film due to the solvent evaporation was processed using a MATLAB routine. For the starch samples, still pictures were acquired at different stages of film formation to visually compare different samples.

Other instruments

A Bruker MSL-300 Spectrometer at 300 MHz ([1]H Larmor frequency) and a Mettler Toledo TGA/SDTA 851e thermogravimetric analyzer (TGA) were also used to study the polymers at different stages of this work. More experimental details using these instruments will be provided in the corresponding chapters.

Chapter 4

Study of gelatin film formation and its characterization

Learn from yesterday, live for today, hope for tomorrow.
The important thing is not to stop questioning.

Albert Einstein

4.1. Introduction

Gelatin forms a solution consisting of flexible individual random coils in water. When this solution is dried above the helix-coil transition temperature (~40 °C), the film produced rarely contains any helix structure similar to the native collagen. On the other hand, below the coil-helix transition temperature, the viscosity of this gelatin solution gradually increases in time which results, even without evaporation, in a thermoreversible transparent gel. The gelling of the gelatin solution results in the formation of three-dimensional cross-linked networks through the development of triple-helix structure which later can pack into fibrils similar to, but not as ordered as, the native tropocollagen fibrils [80]. The gel becomes more structurally stable with time although it is not possible to reach a permanent equilibrium phase due to the physical aging of the polymer. When the gel is dried as a result of solvent evaporation, it becomes a rigid film that shows good mechanical properties (the mechanical strength of gelatin film is comparable to some synthetic polymers like polyethylene and polypropylene) and very little optical scattering [81]. As the triple-helix content plays a vital role in the rigidity of the film, it is obvious that the gelatin film prepared below the helix-coil transition temperature possesses different thermo-mechanical properties than the film obtained from the higher temperature drying.

The study of the physical gelation process has attracted considerable research attention for many years [82]-[83]. It is known that the preparation conditions such as the temperature and humidity during gelatin film formation are crucial. The mechanical properties of this film depend also on those conditions and have been investigated in the context of the water content [84], crystallinity and aging enthalpy [85]. Thermal properties of different types of gelatin and their films have been reported in literature. From these studies, it is evident that unbounded as well as the bound water present in the gelatin determine their structural properties [86]. This can be investigated using NMR techniques and a number of works has been reported in characterizing gelatin gels and films using NMR spectroscopy [23]-[26]. All these studies however, give not much insight into the mechanism of gelatin film formation process. In this work, the film formation of gelatin was studied using a time-dependent low-field NMR 1D-microimaging (profile) measurement to understand the gelatin-water system at molecular level starting from the different initial concentrated solutions. By this way, a biopolymer film was traced during its formation using an NMR experiment from the beginning until the end with microscopic resolution for the first time (section 4.3.1). Furthermore, gelatin film formation was investigated using high-field NMR spectrometer together with the differential scanning calorimetry (DSC) using a different approach (section 4.3.2).

Another purpose of this work was to study the dried gelatin film using different techniques like NMR, XRD and DSC (section 4.4). The results obtained from these studies along with the results of gelatin film formation study are explained using a proposed mechanism (section 4.5). In section 4.6, a study on gelatin film prepared varying the initial concentration of gelatin in the solution is demonstrated at different relative humidities.

4.2. Samples

Solutions starting from different initial concentrations of gelatin in water solvent were prepared as described in section 3.2.1 and cast on the polystyrene Petri dishes at room humidity and temperature (40% RH within 5%, (21$\pm$2) °C). Table 4.1 shows the composition of the gelatin samples and the related studies. These samples were mainly used to study the gelatin film formation and their characterization (section 4.3 and 4.4). Beside these, a number of other samples were prepared which will be described in the corresponding sections. The initial thickness of sample *a*, *b* and *c* were around 11, 8 and 1 mm, respectively. The thickness of sample *a* and *b* were more than the sample *c* which were initially calculated (roughly) to obtain the final gelatin films of around 100 µm of minimum thickness for the later characterization. An immediate gel formation of gelatin

solutions was not observed for sample *a*, *b*, *d* and *g* because the solutions were not concentrated. However, for sample *c, e* and *f* the relatively concentrated solution immediately turned into a gel at room temperature, as is described for example in [80]. The final thickness of the films was measured using a digital micrometer (TOOLCRAFT 820918, Conrad Electronic GmbH, Germany).

Table 4.1: *Different gelatin samples prepared using H_2O or D_2O as a solvent.*

Sample	Initial concentration (%) of gelatin in the solvent (w/v)	Solvent	Initial physical status of the sample	Study	Thickness of the final film (µm)
a	1	D_2O	solution	Profiling at 11.7 MHz (^{1}H) and XRD	100 ± 2
b	2	D_2O	solution	Profiling at 11.7 MHz (^{1}H) and XRD	112 ± 3
c	10	D_2O	gel	Profiling at 11.7 MHz (^{1}H) and XRD	120 ± 10
d	2	H_2O	solution	Profiling at 11.7 MHz (^{1}H) and DSC	100 ± 8
e	10	D_2O	gel	T_1 study at 11.7 MHz (^{1}H)	---
f	10	H_2O	gel	FID at 300 MHz (^{1}H) and DSC	---
g	1	H_2O	solution	Using micro camera	---

Note that exchange with the protons of the atmospheric humidity, i.e. partial condensation occurring simultaneously with evaporation, was found to be slow on the timescale of film formation for the samples prepared using D_2O. A separate set of experiments under identical conditions but replacing D_2O by H_2O was carried out in order to test a possible dependence of gelatin signal behavior on the solvent properties. An example of this kind of experiment is demonstrated using sample *d*. Special sample preparation technique was required for sample *f* which will be described in section 4.3.2. Sample *g* was used to follow the film formation using a micro camera from an initial solution until the end of the film formation.

4.3. Film formation study

4.3.1. Real time film formation study using single-sided NMR scanner

Profiling of the samples

The sample was placed on top of the single-sided NMR scanner and the vertical profiles were obtained by moving the scanner from the air-sample interface to the substrate-sample interface i.e., from top to bottom of the sample as shown in figure 3.8. The time when the gelatin sample is placed on to the scanning device, having a height of approximately 1 mm following partial evaporation of D_2O, is considered as time, t=0. For sample *a*, 194 h elapsed starting from the cast time and the concentration was ~11.6% whereas this concentration was ~14.6% after 72 h had elapsed for sample *b*. For sample *a, b, c* and *d*, 15 representative runs are shown in figure 4.1 out of more than 25 consecutive complete profiles.
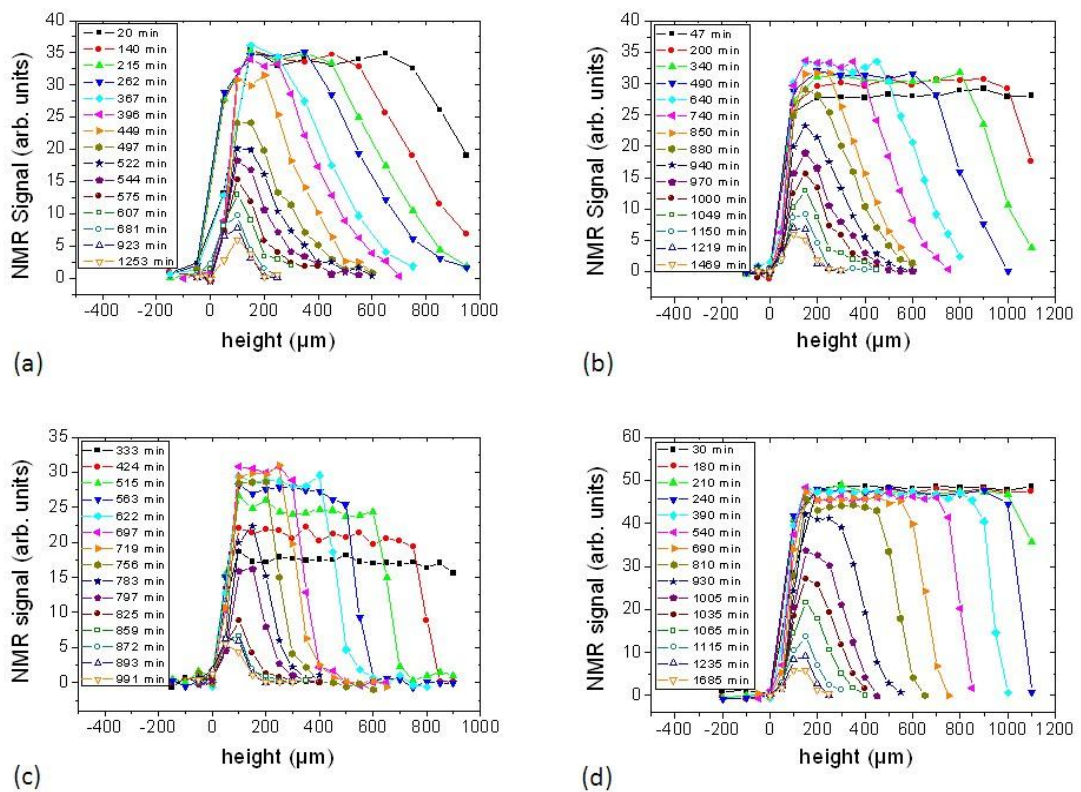

Figure 4.1: *NMR profiles of the gelatin-water solution system at different drying times:* **(a)** *Sample a containing 1% gelatin in D_2O (w/v)* **(b)** *Sample b containing 2% gelatin in D_2O (w/v)* **(c)** *Sample c containing 10% gelatin in D_2O (w/v) and* **(d)** *Sample d containing 2% gelatin in H_2O (w/v).*

From the figure, it is clear that the height of the sample *a* at the beginning of the experiment is inside the field of view of the scanner whereas that of other three samples exceed the field of view. The substrate-sample interface is represented by "zero" on the horizontal axis in figure 4.1. For sample *a* and *b*, the number of steps was reduced from 100 µm to 50 µm which can be seen at 396 min and 640 min of drying time, respectively, to obtain more information when the change in the molecular dynamics of the samples was more obvious. For this reason the profile points of the substrate-sample interface of the first few experiments appear to be shifted towards the left in figure 4.1 (a). On the other hand, the position of the sensor was moved in steps of 50 µm for sample *c* from the beginning and 22 points were required to cover the space beginning from the substrate in this sample.

For sample *a*, the 180° pulse separation used was 66.5 µs for a slice thickness of 100 µm. Sixteen scans and 6 s repetition time give a total time of 96.2 s for the acquisition of data at one position, i.e. one individual slice. That means the time for scanning the full profile was about 20 min. In the sample *b*, the same 180° pulse separation was used but the number of scans and the repetition time were increased to 32 and 6.8 s, respectively. In this case, each profile took about 47 min to be completed. For sample *c*, with a pulse separation (echo time) of 87.5 µs, 32 scans, 1024 echoes and 7 s repetition time, a total time of approximately 227 s was required for the acquisition of data at one position, i.e. one individual slice. That means the time for scanning the full profile was 83 min at the starting of the experiment. This period was followed by a waiting time of 7 min before the beginning of the following slice. As stated in the experimental part (section 3.3), the repetition time and the experimental delay for each of the experiments were maintained such a way that the NMR signal recovers completely before a new scan, i.e. the recovery is within one slice from one CPMG train to the next.

From the figure 4.1, it is seen that only a weak increase of intensity in the profiles is observed for sample *b* but absent for sample *a*. In this case, the signal intensity is weighted by the concurrent decrease of T_2 (see below) and does, for the experimental conditions chosen in the experiment, not represent the true gelatin concentration. In contrary, the amplitude of the signal represented for each point in the profile, is varying in intensity for sample *c*. It is increasing, reaching a maximum around 700 min and decreasing at later stages of the experiment. This increase is occurring due to the change in concentration because of evaporation of the solvent, the later not contributing to the signal. This fact becomes obvious from the profiles of sample *d* as can be seen in figure 4.1 (d). There is no increase in signal intensity in the profile as like as the other sample profiles. This sample is prepared using H_2O instead of D_2O. As a result, the increase in concentration of the polymer due to evaporation may not be distinguishable as the NMR

signal is dominated by the proton of H_2O. From a particular evolution time on (around 400 min, 800 min and 720 min for sample *a, b* and c, respectively) the signal intensity begins to decrease noticeably, a process simultaneously involving evaporation and shrinking, but also the reduction of the constant T_2.

After sufficient evaporation, the gel starts to become what is normally called "film". It is important to mention that the first echo is forming at 87.5 μs. For solid-like samples, a large portion of the signal may have decayed during this period [87]. A fast decaying component (characteristic of solid like signals) can be distinguished in the samples. This was checked by monitoring the free-induction decay (FID) on a solid-state high-field NMR system operated at 7.05 T (section 4.3.2). After this first decay, the signal decays exponentially with a longer time constant. Any information contained in the first part of the FID is thus no longer recovered at the time of the first echo. Note that the slopes at the air-gel interface are different. This can be explained due to the distribution of the solid content in the sample induced by the drying process. This point is discussed below.

Determination of sample shrinking rate

In figure 4.2 the decrease in the sample height as a function of evolving time is shown. The sample heights for sample *b* (2% gelatin in D_2O (w/v)), *c* (10% gelatin in D_2O (w/v)) and *d* (2% gelatin in H_2O (w/v)) have been calculated as the width of the profiles is defined by the values of 5% of the maximum intensity where the signal can still be distinguished reliably from the noise level. For sample *a* (1% gelatin in D_2O (w/v)), 8% of the maximum intensity was used to calculate the sample height where the signal can be distinguished. The rate of evaporation ($\dot{E}$) was calculated from the slope of the fitted lines for the all four samples. It can be observed that the samples have a single evaporation regime which means that the evaporation process has not been interrupted (see below) during the experiment period. For the poly(vinyl alcohol) system, two distinct evaporation regimes were found which will be discussed in the chapter 6. The profile width decreases uniformly with time, yielding the evaporation rate of 2.82×10^{-8} m/s, 1.93×10^{-8} m/s, 2.63×10^{-8} m/s and 1.50×10^{-8} m/s for sample *a*, *b*, *c* and *d*, respectively. Although the sample *b* and *d* have the same polymer concentration, the corresponding rates of evaporation are not the same which indicates that the humidity and temperature of the laboratory may influence the average drying time as they were not controlled but tend to be comparable (checked time to time during all the experiments). Another observation is that the final profile width of these samples is 150 to 200 μm although the final thickness of the films obtained is in the range of 130 μm as can be seen in table 4.1.
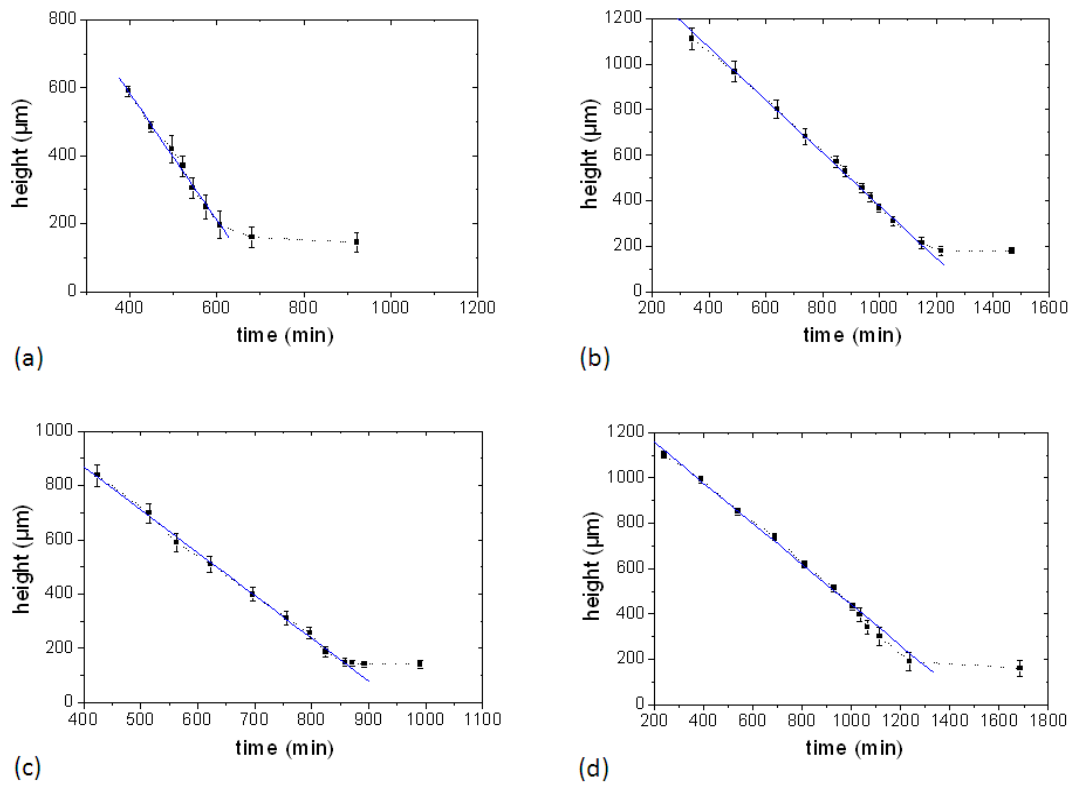
Figure 4.2: *Profile width of the gelatin-water solution system as a function of drying time:* **(a)** *Sample a containing 1% gelatin in D_2O (w/v)* **(b)** *Sample b containing 2% gelatin in D_2O (w/v)* **(c)** *Sample c containing 10% gelatin in D_2O (w/v) and* **(d)** *Sample d containing 2% gelatin in H_2O (w/v). The solid line is the linear fit to the experimental data.*

After the profile experiments, all the films were stored in the same environmental conditions as it was during the drying period and this process ensured the complete drying of the film.

Determination of T_2 at different heights

The CPMG echo decay from each profile point is fitted with mono- and biexponential functions (Equation 3.1 and 3.2, respectively) to obtain the spin-spin relaxation time constant (T_2). A mono-exponential function is fitted to the experimental data whenever possible. At a later stage of drying, the decay curves obtained from the samples prepared from relatively less concentrated solutions (sample *a* and *b*) could only be described sufficiently by taking a second exponential component into account. Figures 4.3 (a), (b) and (c) illustrate the depth-dependence of sample *a* (1% gelatin in D_2O (w/v)), *b* (2% gelatin in D_2O (w/v)) and *c* (10% gelatin in D_2O (w/v)), respectively, where the T_2 values are plotted as a function of the layer position at different drying times.
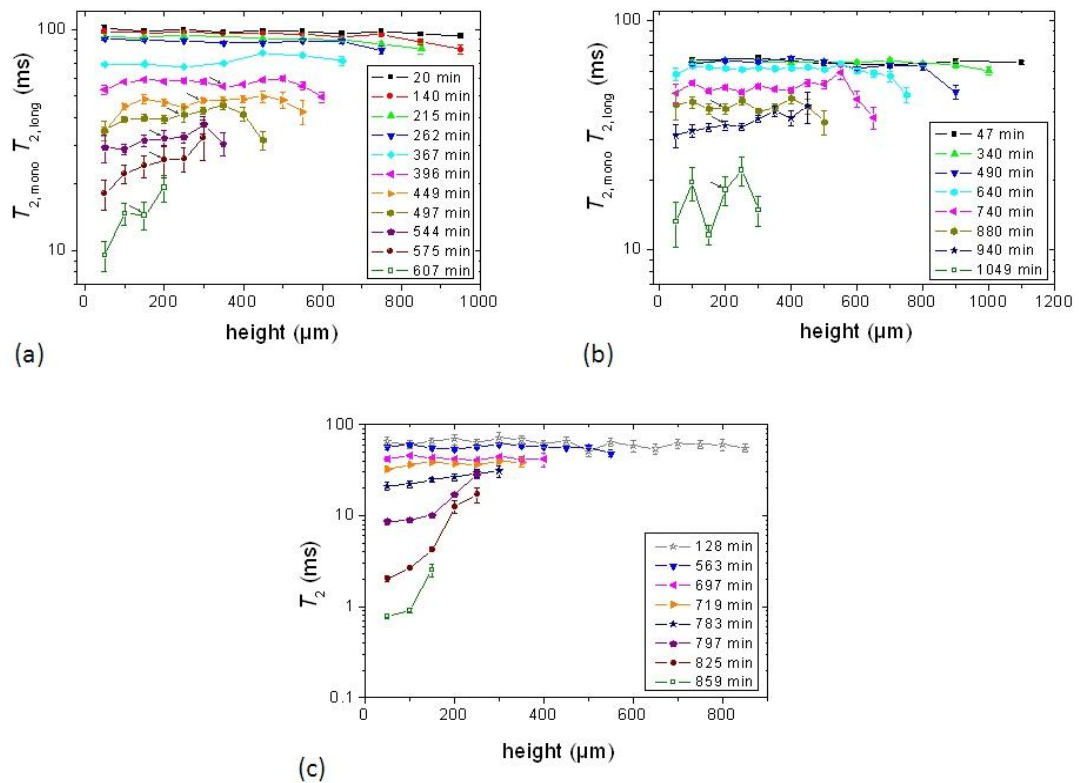
Figure 4.3: *T_2 constants at different heights of the sample. Layer positions correspond to coordinates introduced in figure 4.1:* **(a)** *Sample a containing 1% gelatin in D_2O (w/v)* **(b)** *Sample b containing 2% gelatin in D_2O (w/v) and* **(c)** *Sample c containing 10% gelatin in D_2O (w/v). At the later stage of drying for sample a and b, the echo decay were fitted with Equation 3.2 from the bottom of the sample to a certain height, which is shown by the arrow. In the case of biexponential decay, the effective T_2 data shown in figures (a) and (b) correspond to the slow decaying component. T_2 data shown in figure (c) were obtained from the single exponential decay throughout the experiment.*

From figure 4.3 it is clear that the values of T_2 are almost the same within the experimental error (~101 ms for sample *a* and ~67 ms for sample *b* and ~70 ms for sample *c*) for all heights of the first profile. The T_2 of sample *a* shows a longer value than that of sample *b* although sample *a* was placed at a later time compared to sample *b*. As mentioned before, at t=0, the concentration of sample *a* and *b* were 11.6% and 14.6%, respectively, which may explain the difference in T_2 value. Sample *c* was placed immediately after casting which shows ~70 ms of T_2 after 128 min of drying. Generally, the evolution of the relaxation constant T_2 shows a distinct trend. It decreases with the time of film formation. At a later stage, however, a dependence of T_2 on the position within the sample is developing, and its reduction becomes more pronounced in the bottom part. For example, at the height of 50 μm for sample *a* in figure 4.3 (a), the initial T_2 is ~101 ms at the beginning of the measurement. It is then reduced to 9.5 ms after 607 min of drying

time. On the other hand, T_2 reduces from ~100 ms to 19.2 ms during the same drying time at the height of 200 µm. This effect is most prominent at the substrate-sample interface. A close look at the T_2 values in figure 4.3 (a) up to ~500 min reveals that a similar, but less pronounced, effect is observed at the top surface. For example, the T_2 value after 140 min is ~96 ms at 450 µm which is reduced to ~81 ms at 950 µm height. The variation with height in the vicinity of the air-sample interface is showing slightly more apparent effect in figure 4.3 (b) up to 880 min. On the other hand, for sample *c*, the values of T_2 behave almost the same at different layers, decreasing from ~68 ms to ~43 ms for all heights in the first 697 min as can be seen in figure 4.3 (c). It means that the time scale of the duration of the experiment is shorter than that of the characteristic time scale of the process being studied, i.e. the formation of the film. After that, T_2 begins to vary from layer to layer in the sample. From 719 min onwards, T_2 decreases sharply in the bottom part of the sample. For example, in the bottom layer at 50 µm, initial value of T_2 is ~68 ms which is decreased to ~800 µs after 859 min whereas it is reduced to ~2.5 ms at 150 µm height starting from the same T_2 at 563 min. For this sample, no T_2 effect is observed at the top surface as it was seen for sample *a* and *b* which means that the T_2 variation with height in the vicinity of the air-sample interface can be observed only in the dilute sample.

In sample *a*, the echo decays show one component up to 367 min. From 396 min of the measurement time the short component as well as a long component is detected from the bottom of the sample up to 350 µm and one component is observed from 400 µm to 600 µm. In sample *b*, short and long components are observed from 880 min onwards. Hence, the T_2 values presented in figure 4.3 (a) and (b) are either the relaxation time of the single component at an earlier stage or a combination of single and long component at later stage. When the film is approaching the final drying stage, the T_2 of the film near the substrate is significantly lower compared to the vicinity of the air-sample interface. For sample *b*, this effect is less pronounced. Any effect here would be masked because of the larger experimental error shown in the scatter of the data.

The dynamic heterogeneity of the sample can be seen directly from the raw echo decays, for example, sample *b* as illustrated in figure 4.4. Here the echo decay for two different layers, i.e. for 200 µm (from 47 to 970 min) and 400 µm (from 47 to 940 min) are shown. From the figure, it becomes immediately obvious that the echo decays at 400 µm remain monoexponential throughout the complete measurement period whereas the echo decays at the height of 200 µm develop non-exponential behavior at later stages of drying.
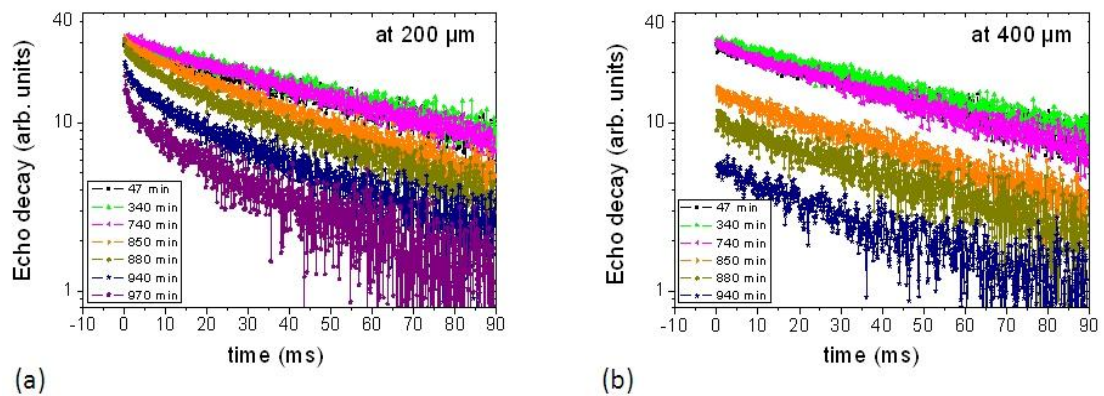
Figure 4.4: *Example of echo decays at 200 and 400 μm height in sample b.*
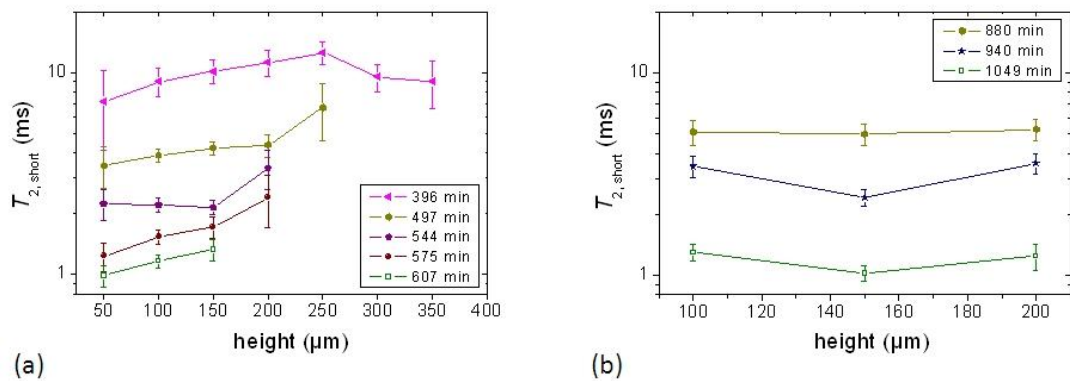

Figure 4.5: T_2 *constatns of the fast decaying component at different heights of the sample. Layer positions correspond to coordinates introduced in figure 4.1:* **(a)** *Sample a containing 1% gelatin in* D_2O *(w/v) and* **(b)** *Sample b containing 2% gelatin in* D_2O *(w/v).*

The short components obtained by analysis of the echo decay using Equation 3.2 are depicted in figure 4.5. In this study, the fast relaxing components giving rise to the shorter T_2 (named as $T_{2,short}$) are considered to be the protons from the rigid backbone corresponding mainly to renatured collagen during the formation of the film. Figure 4.5 (a) shows $T_{2,short}$ of sample *a* between 396 and 607 min. It is seen that $T_{2,short}$ is showing the same type of depth dependence as was found for $T_{2,long}$ (figure 4.3). This means that the fast decaying component is also different at the bottom of the sample than the top of the sample. $T_{2,short}$ of sample *b*, however, does not show such a clear tendency as seen in figure 4.5 (b). For sample *c*, a monoexponential echo decay was observed throughout the drying period which may be considered as the average signal contribution from the polymer backbone proton and the exchangeable proton. Note that control experiment with H_2O as solvent (sample *d*) led to very long and well-separable proton relaxation

contributions, while the gelatin proton relaxation times assumed, within experimental errors, identical values at given times and depths as those in the D_2O prepared solution.

Since the NMR relaxation time, in this case the transverse relaxation constant (T_2), probe the molecular dynamics of the system [32], any change in the molecular mobility will be sensed by this parameter. In liquids and solutions, the relaxation rate will be proportional to an average reorientation time τ of the molecule as well as to the viscosity, i.e. $T_2^{-1} \approx \tau$ and $T_2^{-1} \approx \eta$. Consequently, it must be concluded that during evaporation of the system, the molecular mobility in the vicinity of the air-sample interface decreases. This kind of effect is well known in most latex dispersions [88] where the latex particles accumulate at the surface, a consequence of the evaporation of the solvent together with the capillary force. A macroscopic skin could then be formed because the capillaries are closed as a result of compression. In the present experiment, the T_2 curves (figure 4.3) of the samples suggest that there is indeed a decrease of mobility in the outer layers of the gel. But a formation of a "skin" as it was suggested for the case of latex film, for example, in reference [89] is improbable because it should change the evaporation tendency and persist until the final stages of film formation. However, there is no change in evaporation tendency as can be seen in figure 4.2. Furthermore, the NMR relaxation results show that at the upper surface, the decrease of T_2 vanishes at long times close to the end of the film formation process. At these times, the T_2 constant decreases only in the direction of the substrate-sample interface at the bottom.
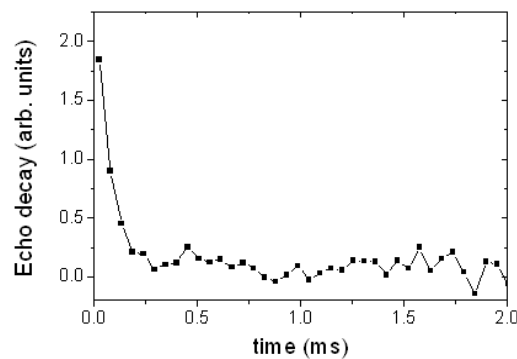

Figure 4.6: *Echo decay obtained from the polystyrine Petri dish.*

Note that Petri dish made of polystyrene gives rise to a signal which decays within 300 µs as can be seen in figure 4.6. The intensity of this echo decay is much lower than that of the signal of the sample at the early stage of film formation which will not affect the sample signal. However, this effect may become crucial at the later stage of drying process when the signal intensity obtained from the sample is less. Taking into account

that the signal obtained from the lowest part of the sample was 50 µm above the Petri dish and the slice thickness used at the later stage of the film formation process is 50 µm with a pulse separation of 87.5 µs, it was affirmed that the effect is negligible by comparing the echo decay obtained from the Petri dish to the echo decay of bottom part of the sample during the analysis.

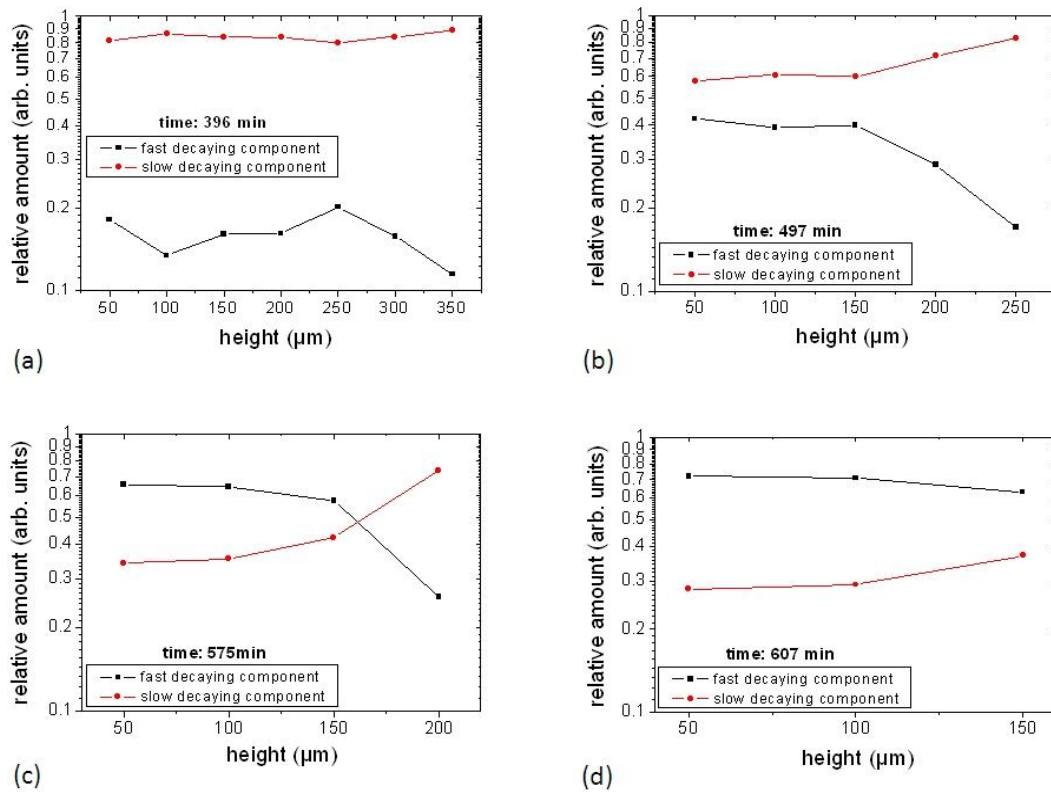## Relative weight fraction of T_2 components at different heights

Figure 4.7: *Change in relative amount of fast and slow decaying components with time in sample a.*

The coefficient A_{short} and A_{long} are obtained from the echo decay analysis of the samples using Equation 3.2. The relative amounts $A_{(i,j)} / (A_i + A_j)$ as obtained for sample a where $\{i, j\} = \{short, long\}$, are plotted in figure 4.7. Here the component with a shorter relaxation constant may be assigned to the more rigid region, while the slow decaying component is assigned to the amorphous region corresponding to the denatured collagen [25]. From figure 4.7 (a) it is seen that the relative amount of the fast decaying component remains between 10 and 20 % at 396 min, no particular trend regarding different heights of the sample is observed. At 497 min, a tendency is seen where relative amount of the slow decaying component is lower at the bottom of the sample than the top of the sample

as illustrated in figure 4.7 (b). Comparing to figure 4.7 (a), the relative amount of the fast decaying component is increasing with time whereas it is decreasing for the slow decaying component. Figure 4.7 (c) shows that the tendency of both components remains the same. These results support the notion that the bottom part of the sample is drying faster than the top part at this stage of drying. In figure 4.7 (d), it is seen that the relative amount of the shorter component is higher than that of the longer components in all heights of the sample after 607 min of drying.

Determination of T_1 at different heights

During the profiling of samples, no spin-lattice relaxation time (T_1) measurement as a function of different sample layers was carried out since its duration would compromise the temporal resolution of the profile experiment. Instead, in order to obtain T_1 data at different layers during film formation, sample *e* containing 10% gelatin in D_2O (w/v) was used as a reference. In this experiment, the parameters like repetition time, the number of steps and number of scans were also changed accordingly with the continuation of the drying process as it was done for acquisition of the profiles.
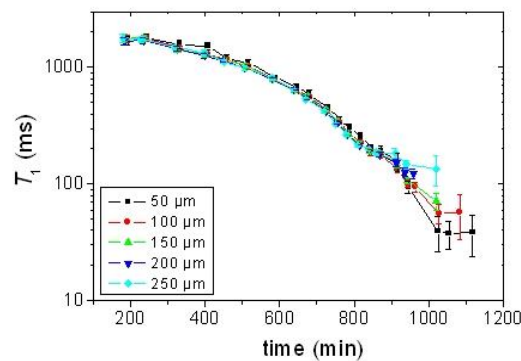

Figure 4.8: *Evolution of T_1 with drying time in sample e. Layer positions correspond to coordinates introduced in figure 4.1.*

T_1 was measured inside the sample as a function of evolution time at different layers of the sample as has been done for T_2. The result is shown in figure 4.8. It is seen that T_1 decreases as well with the evaporation of the sample. Note that the total drying time possibly differs from the conditions of sample *c*, so that a direct comparison of states at identical times is not feasible. However, the final film thickness appears to be reached at approximately 1000 min so that the variation of T_2 and T_1 values over time and layer

thickness can be compared at least qualitatively. At the beginning, the maximum T_1 is about 1700 ms. But after 200 min of drying, it begins to decrease significantly by more than one order of magnitude. Considering different layers, there is no significant difference in T_1 for times up to about 800 min. Then T_1 values start to vary between the layers. For example, after 1025 min of drying, T_1 is 135 ms at 250 µm height but only 40 ms at the height of 50 µm. This change in T_1 in different height of the sample confirms that the drying of the gelatin film is inhomogeneous after a certain time period.

H-D Exchange

Because the system is prepared using D_2O as a solvent, H-D exchange is expected [90] but it is not introducing any systematic error in this experiment. Upon dissolving gelatin in D_2O, all exchangeable protons of the gelatin will exchange with D_2O molecules, thus producing a certain amount of HDO molecules. The relative fraction of exchangeable protons can be estimated to about 15% [23], this results in a fraction of approximate 0.25% of all deuterium oxide molecules to possess one proton; likewise, 99.75% of the exchangeable sites are now deuterated. Due to the fast exchange time between the exchangeable protons and water (well below one second), this equilibrium is maintained while D_2O and HDO molecules are removed by evaporation (neglecting different evaporation rates between these two). These HDO protons are responsible for the long (about 6-7 seconds) component in T_1 and mostly suppressed by the repetition time, with the remaining contribution being a few % at most. This contribution is not observed within the experimental error. Assuming fast exchange and the fact that the T_2 of protons in HDO is also several seconds, its influence on the measured ^{1}H relaxation times is negligible. The ^{1}H distribution is expected to assume equilibrium in the early stages of sample preparation. Only those approximate 15% of nuclei in exchangeable sites in the gelatin may potentially be affected; the remainder does not exchange and manifests the dominant signal contribution. It is this contribution that also undergoes the strong reduction in T_2, which can only be explained by a considerable reduction in mobility. The limiting value of T_2 ~300 µs (shown below in figure 4.14) suggests that a fraction of the protons do not assume a rigid state but retain some degree of mobility.

The effect of exchange on the measured T_2 value is minimized by the small concentration of protons in the aqueous phase (HDO). Detailed studies, using pure H_2O and isotopic dilution, have been carried out by Hills *et al* [87] and suggest exchange rates on the order of 2000 s^{-1}. The echo times used in this study are shorter than the

corresponding times and would lead to the measurement of the individual components of T_2 if they carried a sufficient signal contribution.

4.3.2. Gelatin film formation study using high-field NMR and DSC

Renaturation process of gelatin at room temperature is of great interest to the scientists for over 50 years [91]-[92]. Polarimetry, differential scanning calorimetry (DSC), ultra-violet (UV) spectrometry, ultrasonic absorption, rheology and X-ray diffractometry (XRD) are the common techniques which have been widely used to study the gelatin renaturation. Flory and Weaver (1960) observed the renaturation of gelatin using polarimetry and proposed a first order kinetics model of this process which had been the most commonly accepted mechanism [93]. Later on, investigation of gelatin renaturation mechanism has been carried out varying different parameters, for example, source of gelatin, concentration of the solution and drying temperature [80], [94]-[96]. The focus of these studies, in general, was to understand renaturation process of the gelatin keeping the system in gel or solution state below the helix-coil transition temperature or from the characterization of the final film. In this present study, gelatin film formation process was followed using a combination of the high-field NMR spectroscopy and DSC methods while the sample was under continuous evaporation and information on the renaturation process for this kind of system was obtained.

A series of Petri dishes (35 mm diameter) was used to cast exactly the same amount (by weight) of sample f (10% gelatin in H_2O) in each Petri dish. All the Petri dishes were placed in the same environmental conditions (40% RH within 5%, (19±2) °C) and let them evolve. The samples immediately turned into a gel at room temperature. After predetermined interval of time, one of the Petri dishes was collected for sample preparation allowing the rest to further evolve. A required amount of gelatin sample was prepared for NMR and DSC studies to measure immediately. It was assumed that the evaporation tendency as well as the gel system would be disrupted due to the collection of the sample from a Petri dish and it was not used further.

The initial amount of the gelatin sample was selected such a way that the drying process continued for a long period and the required number of experiments was possible to carried out to obtain sufficient data as a function of drying time. The optimized experimental design also allowed conducting the successive NMR and DSC experiments in each interval and repeating the experiments if necessary. It was found that the cast sample became opaque at later stage (around 60 h) of evaporation although the experiments were carried out until 100 h.

NMR spectroscopy study

The samples were measured immediately after preparation using a Bruker MSL-300 Spectrometer with a magnetic field strength of 7.05 T (300 MHz proton (^{1}H) Larmor frequency), suitable for wide-line solid-state NMR experiments. A double-resonance probe (Bruker) with a short dead time characteristics was used for the static ^{1}H NMR measurements. Typical 90° pulse length was 5 µs which was optimized for the gelatin samples. A single pulse (or Bloch-decay) sequence [97], which uses a 90° pulse followed by detection of the free induction decays (FID), was employed at room temperature. The recycle delay used in this measurement was 6 s with minimum number of scans of 256.
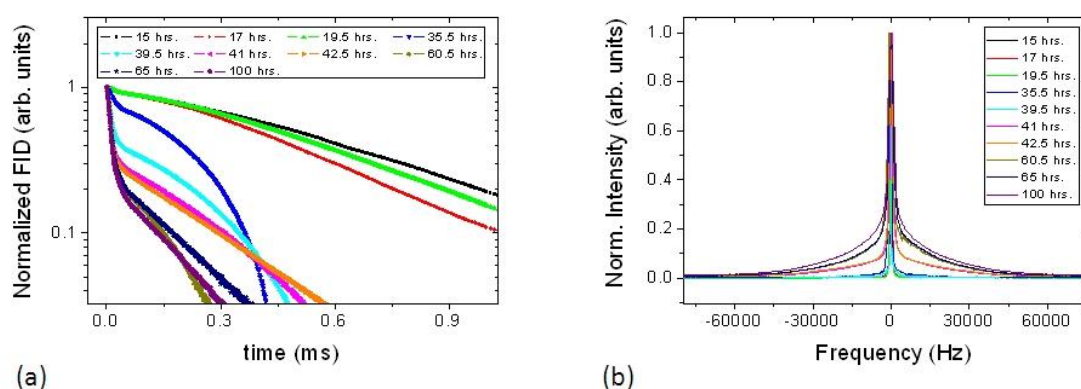

Figure 4.9: (a) *The free induction decay (FID), normalized to the initial point in the decay, as a function of drying time and* **(b)** *^{1}H wideline spectra of gelatin sample obtained from the FID as a function of drying time.*

Figure 4.9 (a) compares the normalized FID obtained at different drying times. The FID contains two different decays which can be seen clearly after 20 h of drying. Both decays become shorter with evolution time. The components having the shortest decay may be assigned to the protons of the solid like protein chains. The slow decay components correspond to the combined contribution of the water protons and the protein side-chain protons which able to exchange with water proton. The mobility of these protons is affected by the evaporation process which is the reason for the reduction of the corresponding decay with time. At around 40 h of drying time, the fast decaying components decay within 100 µs after the pulse which is the signature of the solid like components [87]. From figure 4.9 (a), it is seen that the long tails of the FID are affected more by the off-resonance condition which can be clearly seen in the decays of the FID at 35.5 h and 39.5 h. Figure 4.9 (b) shows the frequency domain spectra which is obtain by the Fourier transform (FT) of the time dependent FID. The FT is a linear process which means that if the time domain is a sum of functions, the frequency domain will be a sum of Fourier transforms of those functions [98]. In order to make a quantitative analysis of these spectra, dmfit program [99] was used.
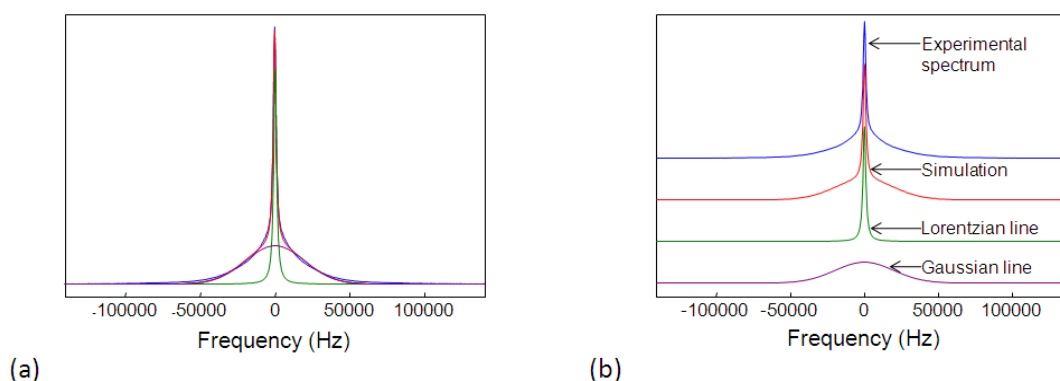
Figure 4.10: *Example of the deconvolution of a spectrum of the gelatin sample as obtained from the figure 4.9b.* **(a)** *The experimental spectrum together with the simulation and fitted lines and* **(b)** *The fittings are illustrated in detail.*

The spectrum of each sample was fitted with two components which correspond to two peaks having a broad and a narrow linewidths, respectively. As shown in figure 4.10, the wide-line spectra consisting of superposition of two peaks with significantly different linewidths. A Gaussian function, which has the broad linewidth, was fitted as a characteristic of the solid like protein chain whereas a Lorentzian function was used for the mobile proton of the sample [100] . The linewidth of the Gaussian and Lorentzian line at half-height, also known as FWHM (full width at half maximum) of the two fitted peaks are shown in figure 4.11 (a) and 4.11 (b), respectively, as a function of drying time. From figure 4.11(a) it is seen that until 35.5 h, FWHM value of the broad peak is around 3 KHz which grows about two orders of magnitude until 41 h of drying time. After this time, the FWHM value does not change significantly until 100 h. As explained in section 4.1, when gelatin film formation is carried out at room temperature, partial renaturation of the gelatin takes place. This means the formation of collagen like triple-helix structure which will give rise to the solid-like NMR signal in the gelatin sample. If this phenomenon is combined with the result obtained in figure 4.11 (a), one can conclude that partial renaturation during the gelatin film formation is not a continuous process which is taken place for a short period of time after a certain time of evaporation. From a recent optical rotation study by Gornal *et al.* [80], it can be seen that the initial secondary helix formation in a gelatin solution, which is quenched from 50 °C to 11 °C, may take place in around 45 min when the gelatin concentration is as high as 38% (w/v). On the other hand, Busnel *et al.* [101] observed that a stable value of helix content cannot be achieved after 85 min gelation time when a set of very diluted gelatin solution samples (0.05 to 0.8% (w/v)) was studied at 10 °C using the same method. Djabourov *et al.* [102] pointed out that total renaturation of a gelatin solution may take years if it is allowed to a long period of aging depending on the quench temperature. Taking into account that the concentration of gelatin is very high

after 35 h of drying (initial concentration was 10%) in this present study, it is remarkable that the renaturation starts after a certain evaporation time (about 35 h in this case) and this process may take few hours to complete when the gelatin film is prepared at room temperature.
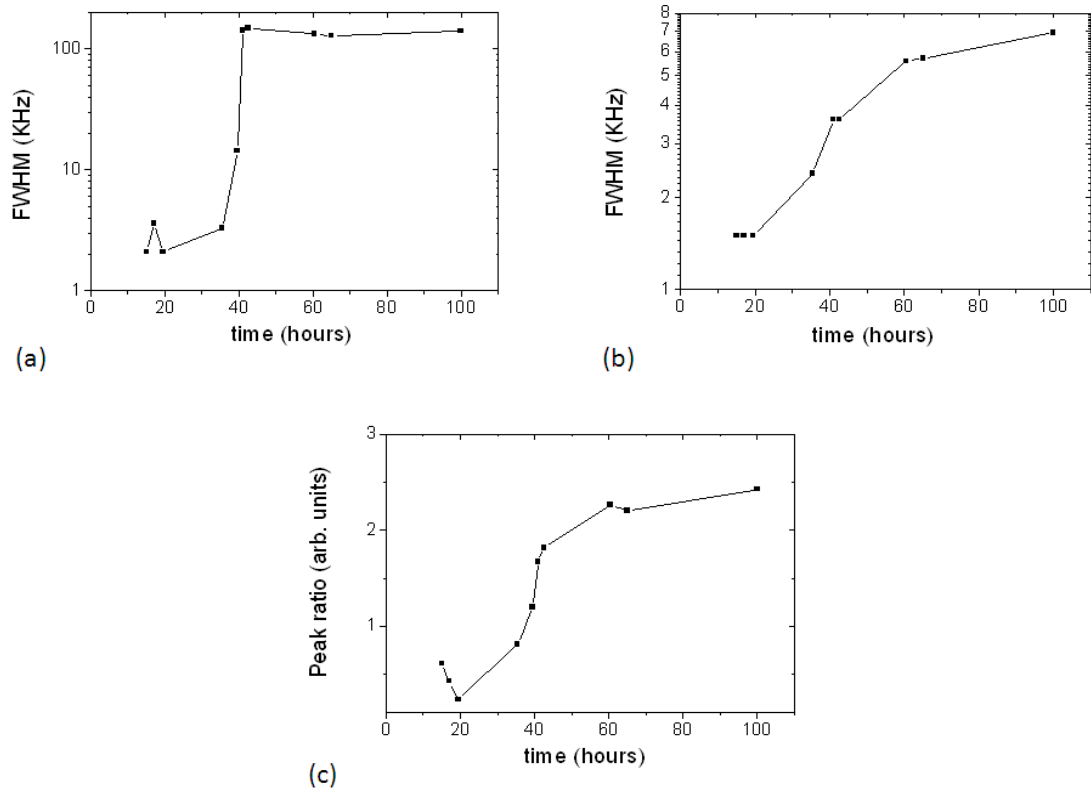

Figure 4.11: *Full width at half maxima (FWHM) of the* **(a)** *Gaussian line* **(b)** *Lorentzian line as obtained from the fittings (figure 4.10) of spectra (figure 4.9b)at different drying times* **(c)** *Ratio of the Gaussian to the Lorentzian peak area as a function of drying time.*

After 15 h of drying, on the other hand, the FWHM value of the sample presented in figure 4.11 (b) is in the range of 1.5 KHz. Consequently, the motion of the exchangeable protons is not isotropic in the system. Note that the free water molecules in fluid show a linewidth of less than 100 Hz [26]. From figure 4.11 (b) it is evident that the FWHM value of the narrow peak increases after 20 h of evaporation until the end of film formation study (100 h) although the growing rate decreases in the last 40 h. The FWHM value increases from around 1.5 KHz to 7 KHz during the whole drying period which means that unlike to the protons involved in the partial renaturation process, the mobility of the protons responsible for the slow decay decrease with evaporation of the solvent.

Figure 4.11 (c) represents the values of A_{broad} / A_{narrow} as a function of drying time where A_{broad} and A_{narrow} are the derived areas of the Gaussian (broad) and the Lorentzian (narrow) peaks, respectively. Before around 38 h, $A_{broad} < A_{narrow}$ whereas it is vice versa

after this evaporation time. Renaturation process continues at this drying time as can be seen from figure 4.11 (a) which is responsible for the increases in the peak area of the Gaussian line. At the same time, peak area of the Lorentzian line decreases due to the evaporation of the solvent.
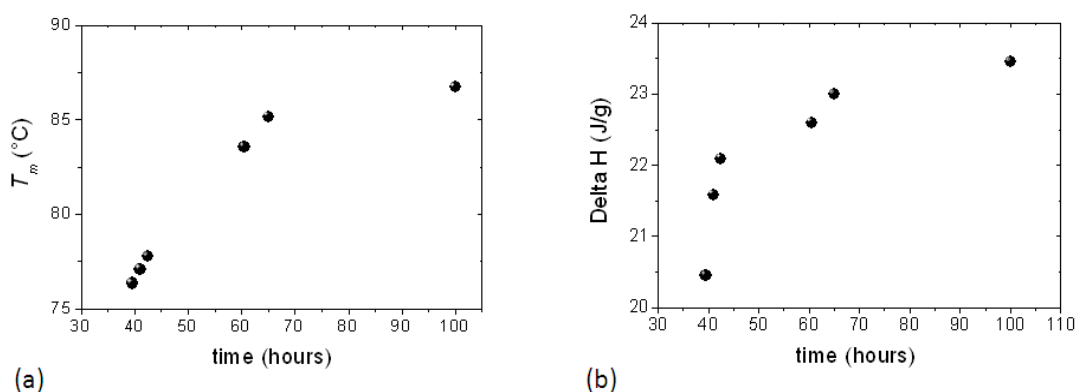
DSC study

Figure 4.12: (a) *Melting temperature (T_m) obtained from the melting peak of the gelatin sample at different drying times and* **(b)** *Drying time dependence of change in enthalpy (ΔH) of gelatin film during its formation.*

A Perkin Elmer DSC 7 unit was used to study the gelatin film formation at different drying times starting from the gel to a film. All the thermograms were taken between +10 °C to +120 °C at a heating rate of 10 °C/min. The thermogram is characterized by the peak which refers to the melting of the crystal domain originated from the collagen like triple-helix structure in the gelatin (section 4.4.3). Before 39 h of drying, no melting peak was observed from the thermograms of the samples and afterwards, the peak appeared until 100 h of drying time (figure 4.12 (a)). This fact further complements the NMR study in which the triple-helix structure was found to be formed by this time (figure 4.11 (a)). DSC studies show that there is a sharp increase in T_m until 65 h of drying time which further gradually increases until 100 h. On the other hand, NMR study shows that the amount of triple-helix structure does not increase after 41 h of evaporation time. In general, as the crystallinity in the sample increases, melting peak shifts to a higher temperature [103], however, this is not the case in the present study. Note that the helix-coil transition temperature in the gelatin solution is ~40°C (section 4.1). But the melting of the helix structure started at around 76 °C which increases further with drying time in this current gel system. In a gel the amount of water is less and mobility is restricted compared to a gelatin solution system. This means that the evaporation of the residual water, which may act as a plasticizer, from the system plays an important role to shift the melting peak to a higher value.

The increase in rigidity of the crystalline structure in the gelatin film during drying was confirmed by the corresponding enthalpy change or heat of fusion (ΔH) values listed in figure 4.12 (b). The heat required for melting per gram of sample (ΔH in J/g) was obtained by the integration of the area under the melting peak and then dividing by the total amount of sample (in g) used to obtain the thermogram. Although the film looked opaque from the exterior due to evaporation of most of the solvent at later stage of drying, it might contain water which serves as a plasticizer until it evaporates with time. This means that the crystalline structure becomes more rigid with time and more heat is required for melting the structure although the total triple-helix content does not increase. This information further supports the NMR analysis that the ratio of Gaussian to Lorentzian peak area increases with the evolution time (figure 4.11 (c)). Note that a clear glass transition temperature (T_g) was not observed in this set of measurements which is also a characteristic property of the gelatin film (see section 4.4.3).

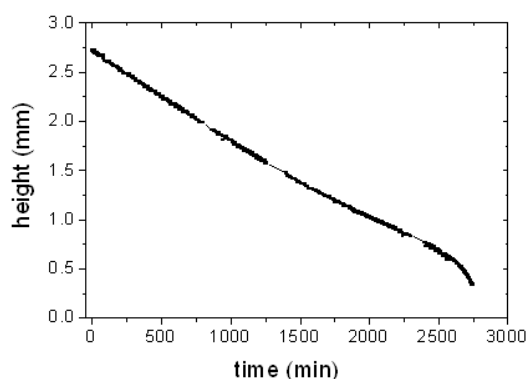## 4.3.3. Determination of evaporation tendency

Figure 4.13: *Reduction of height as a function of drying time in sample g.*

The real time evaporation of the solvent from a 1% gelatin solution (w/v) system (sample *g*) was followed to explore the relation between the evaporation and drying time using a micro camera. Figure 4.13 represents this relation where the height of the sample is plotted as a function of drying time. From the figure it is observed that the height of the sample decreases almost linearly with time until 1200 min. After that the height decreases non-linearly. During the final 150 min of drying, a sharp increase in shrinking is seen with time which corresponds to an increased evaporation. It is found that the maximum sample height change during a certain time which corresponds to the period required for acquiring a full profile of the gelatin sample at this drying stage is 30 μm. This value is well inside of the minimum resolution that is used (50 μm) during the profile measurement.

Consequently, this quick shrinkage would not affect the phenomenon which is seen in the present study. Note that this effect is absent in figure 4.2 where the evaporation tendency is determined from the width of profile as a function of drying time.

4.4. Film characterization

The films obtained from samples *a, b, c* and *d*, respectively, were stored in identical environmental conditions for sufficient time to ensure complete drying. Then the films were characterized using NMR, XRD and DSC methods.
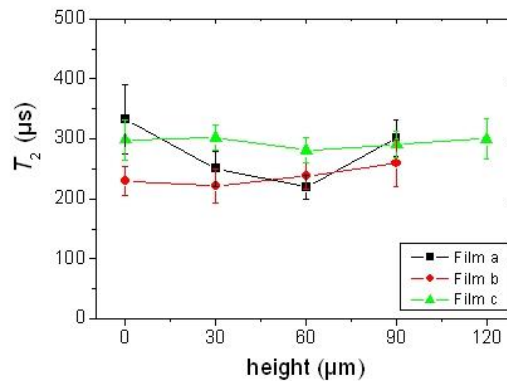
4.4.1. Single-sided NMR study

Figure 4.14: *T_2 constant at different layers of the completely dried film: film a prepared from sample a containing 1% gelatin in D_2O (w/v), film b prepared from sample b containing 2% gelatin in D_2O (w/v) and film c prepared from sample c containing 10% gelatin in D_2O (w/v).*

Film *a* (obtained from sample *a* containing 1% gelatin in D_2O (w/v)), film *b* (obtained from sample *b* containing 2% gelatin in D_2O (w/v)) and film *c* (obtained from sample *c* containing 10% gelatin in D_2O (w/v)) were under continuous investigation for prolonged period of time (until 210 days) and no significant difference in relaxation behavior inside the samples was observed. The parameters for this experiment were 87.5 µs for the echo time with 32 echoes, 200 to 250 ms of repetition time, 1024 to 2048 scans and no delay between two successive experiments. Figure 4.14 shows the T_2 relaxation time at different layers of the film *a*, *b* and *c*. Within the experimental error, all of the films show T_2 values of about 300 µm without any definite trend at different layers of the films. This result suggests that the final film appears to be homogeneous although the earlier discussion shows that the drying process is inhomogeneous, at the beginning faster near to the air-sample interface and at the end faster near to the substrate-sample interface.

Note that the final thickness of these films was in the range of 130 μm (Table 4.1) which was not enough to perform the experiments using bigger slice thickness to have a shorter pulse separation (echo time) [31]. As the single-sided NMR scanner is not able to detect the solid-like signal decaying below 100 μs, a pulse separation of 87.5 μs may not be sufficient to obtain the actual information about the relaxation behavior of the solid sample at different heights. For this reason, X-ray diffraction (XRD) technique, which is potentially more sensitive in the investigation of structure, was applied to characterize the final films.
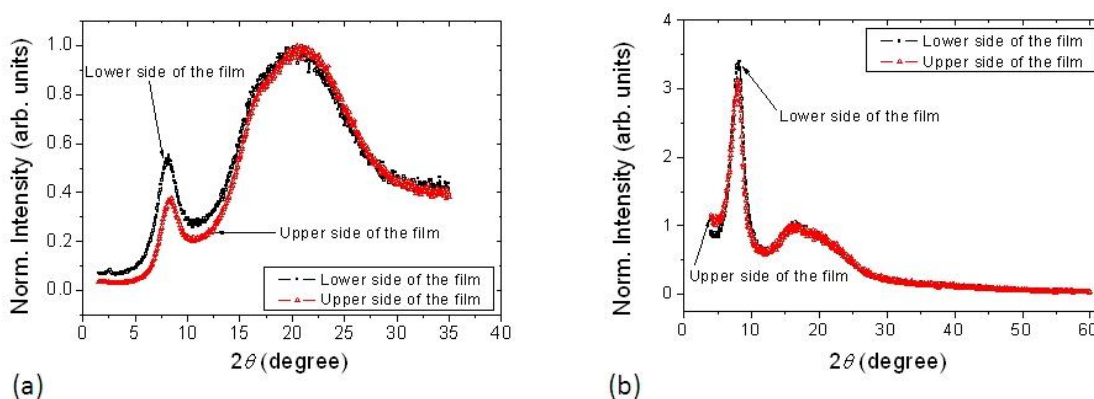
4.4.2. XRD study

Figure 4.15: *X-ray patterns of film a prepared from sample a containing 1% gelatin in D$_2$O (w/v) using* **(a)** *Traditional method and* **(b)** *Fixed angle incident beam method.*

As observed in figure 4.14, apparently the film is homogeneous when regarding relaxation at different layers, which is an indicator for mobility. The X-ray diffraction (XRD) study was performed in order to observe whether the heterogeneity observed during film formation by NMR persists even when the film formation process is completed. XRD was applied separately on both sides of film *a* as shown in figure 4.15. This simple approach can be used in order to detect structural differences that may have appeared during film formation. To acquire the XRD spectra, traditional geometry where both the x-ray source and the detector move in the vertical plan was applied for a range of angles 2θ = 1.5 to 35° (figure 4.15 (a)). In addition, the fixed angle incident beam method was used where the X-ray source was kept fixed to 0.5° throughout the experiment, and the detector moved through an angle of 2θ = 1.5 to 60° (figure 4.15 (b)). In the first method, possibility of the X-ray beam to penetrate into the sample without being scattered is more than the second method in which the X-ray beam may scatter more from the surface area of the sample as the incident beam angle is very low. It was found that the second method is more suitable for the present study as the heterogeneity in the structure of a film can be seen by comparing the crystalline pattern of the XRD spectra near to the upper and lower

surfaces, respectively, of the same film. Consequently, this method was used for the same kind of studies for the films obtained from the other polymers (see chapter 5 and 6).
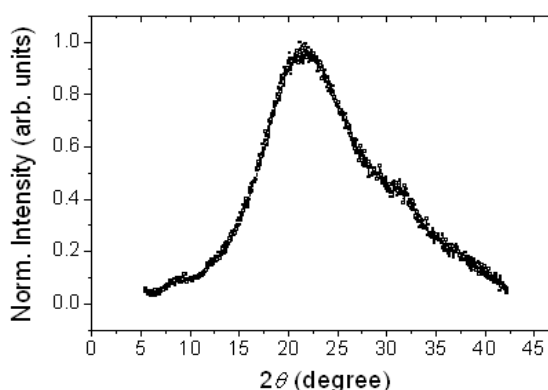

Figure 4.16: *X-ray patterns of the raw gelatin sample.*

It is well known that the partially crystalline gelatin film shows a characteristic peak at 2θ ~7-8° which is due to the triple-helix structure in collagen and also in renatured gelatin [104] In figure 4.15 relatively sharp peak is observed at 2θ ~8° and a broad distribution at 2θ ~20° for both measurements. The first peak is assigned to the partially crystalline region originating from the triple-helix structure as stated above, and the second broad distribution is due to the amorphous fraction of the sample. On the other hand, the XRD pattern obtained from the raw gelatin shows only a broad distribution which can be characterized by the amorphous region (figure 4.16). This means that the gelatin sample used in this study was fully denatured.

The relevant result in figure 4.15 is that the relative amount of partially crystalline structure at both sides of the film is not the same in comparison to the amorphous fraction. Note that the X-ray can, in principle, penetrate through the whole film in each measurement. But at low 2θ angle, the obtained information is mainly from the vicinity of the surface where the X-ray beam penetrates. This shows that the lower part of the film contains a relatively higher amount of partially crystalline or renatured collagen region than the upper part of the film, i.e. a larger amount of the triple-helix structure is found in the lower part of the film. This confirms the fact that T_2 data of the dried film in figure 4.14 does not show a clear heterogeneity is because the resolution of the single-sided NMR scanner is insufficient to observe this kind of microscopic phenomena in a solid sample, and that the very short contribution of the crystalline region to T_2 is lost before the acquisition of the first echo. The solid-state NMR spectroscopy could be a suitable tool to observe this effect.

4.4.3. DSC study

Dried film obtained from the sample *d* containing 2% gelatin in H_2O (w/v) was characterized using differential scanning calorimeter. The thermogram which was recorded at a heating rate of 10 °C/min in the temperature range 0-110 °C is shown in figure 4.17. After the completion of the first scan, the sample was cooled to the room temperature at a rate identical to the rate of heating and allowed to wait for 5 min and then the second scan was carried out using same parameters. The DSC plot obtained during the first scan shows a glass transition temperature (T_g) at around 55 °C related to the amorphous part of the gelatin film, followed by a melting peak (T_m) at around 92 °C related to the melting of the crystalline domain. On the other hand, the second scan contains a glass transition temperature (T_g) at around 43 °C and no melting peak as it is seen from the figure.
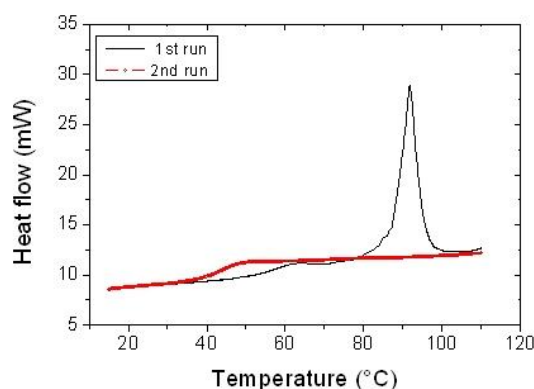

Figure 4.17: *The first and second heating scans of DSC thermograms for the gelatin film prepared from the sample d containing 2% gelatin in H_2O (w/v) at room temperature.*

The endothermic melting peak in the first heating scan further confirms the presence of structural gelatin (collagen like triple-helix structure) in the prepared film in this work [105]. During melting at 92 °C, the water presents in the gelatin film in various forms is released. It is known that the water molecules play a vital role in the collagen like triple-helix structure during the formation of gelatin film at room temperature [84]. When the triple-helix structure is unfolded upon heat treatment, they separate into individual helices at first by the disruption of water bridges (hydrogen bonds) between the three polypeptide chains and then into random coils which involves the disruption of intrahelical hydrogen bonds [86]. The water, released at the end of first heating, plasticizes the gelatin film [45] when the second heating is carried out. As a result, T_g of the film is reduced.

There is no melting peak related to the partial collagen like structure on the second scan as the triple-helix structure is completely disrupted during the first scan.
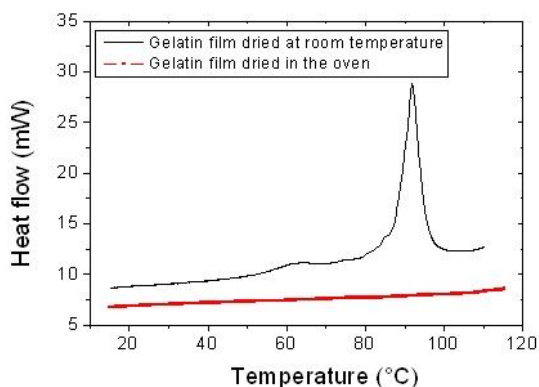

Figure 4.18: *A comparison between the DSC thermograms for the gelatin films prepared from the sample d containing 2% gelatin in H$_2$O (w/v) at room temperature (21 °C) and a film prepared in the oven at 60 °C from the same initial solution.*

The solution containing 2% gelatin in H$_2$O was cast on a Petri dish and the film was prepared in the oven at 60 °C to check the formation of partial triple-helix structure in the oven dried film. A comparison between the two DSC thermograms obtained from the film in the room temperature and the oven is shown in figure 4.18. Although the film prepared at room temperature contains a glass transition and a melting peak as described above, the film prepared in the oven does not show any of these thermal properties. A glass transition is expected in this kind of film as shown by Dai *et al.* [85] which is not clearly visible in this study. However, this study reveals that the film dried in the oven at a temperature (60 °C), higher than the helix-coil transition temperature (~40 °C) is completely amorphous without any structure.

4.5. Proposed Mechanism of gelatin film formation

For the comparatively dilute solutions (sample *a* and *b*), an increase in T_2 along the sample height from top to the bottom was observed at the beginning of the film formation which was absent in relatively concentrated solution (sample *c*). On the other hand, all the samples *a*, *b* and *c* show an increase of T_2 along the sample from bottom to the top layer during the film formation at a later stage. A possible microscopic explanation for the observed change of T_2 during the film formation process needs to take the combined effect of molecular clustering, structural regeneration, and solvent evaporation into account.
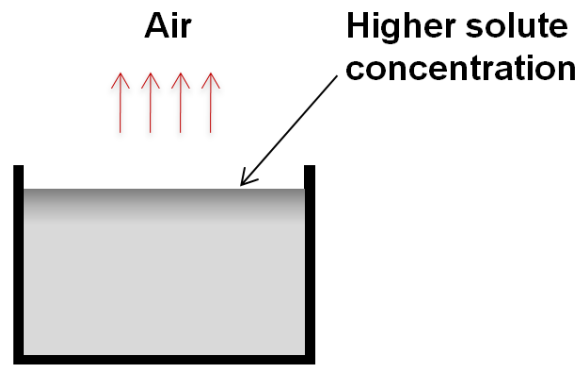
Figure 4.19: *Illustration of the evaporation of solvent from a dilute solution showing the distribution of the higher solute concentration at the evaporating surface.*

In reference [106], a general model of diffusion in evaporating solutions is proposed. It is found that the concentration of the solute has different distributions depending on the concentration of the solution, number of components and relative diffusion constants between components. In the limit of a very dilute solution (low solute content), the evaporation of the solvent induces an exponential concentration profile where the maximum solute concentration is found at the evaporating surface. The relevant information is that this limit could be applied in the low concentration gelatin solutions reported in this work. As it was mentioned above (section 4.2) in these dilute systems (sample *a* and *b*), an immediate gel formation is not observed. The solute concentration distribution is then determined by the evaporation process. Due to the fact that close to the evaporating surface the solute concentration is maximum, i.e. the solvent viscosity is higher, and one would expect that at the microscopic level, molecular mobility is more restricted and therefore T_2 is shorter than in the inner layers far from the surface. This macroscopic distribution could persist after the gelatin gel is formed and the network structure of gelatin develops, but it will not determine the T_2 behaviour at later evolution times when concentration increases (figure 4.3 (a) and 4.3 (b)). Upon evaporation, the system transfers to a more concentrated state and the solute concentration profile is not anymore a simple exponential as described in [106]. The decreasing of the value of the T_2 constant close to the evaporating surface is then ascribed to the region in the sample that is more concentrated, i.e. that possesses more gelatin. Note that the effect is not observed at any time of the drying process in the more concentrated 10% gelatin solution.

Generally, the network structure of gelatin increases when gelatin gel is formed starting from a solution. The gelatin film formation experiments using NMR technique were carried out at around 21°C. This temperature is lower than the gelation temperature of
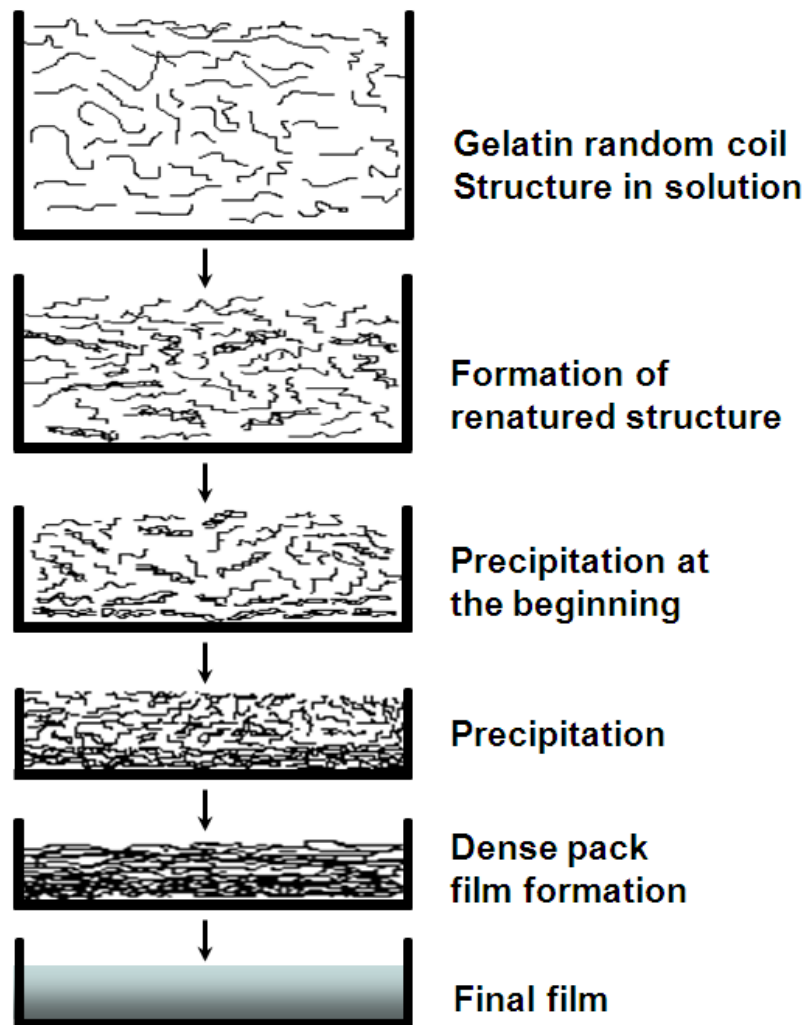
Figure 4.20: *Illustration of the gelatin system at different drying times. The evolution time increases from top to bottom.*

gelatin for the cooling regime. In this condition, the first stage of film formation involves the aggregation of the higher molecular weight molecules (regenerated collagen) to cluster themselves and to become attached to the already formed gel clusters [107]. The aggregated long chains are hydrogen bonded to form the well known helix structure. Pure collagen is insoluble in H_2O and D_2O. However, raw gelatin does dissolve well in water. Gel on the other side, as it is mentioned above, consists of (incompletely) regenerated collagen forming the gel network. The film formation study using high-field NMR (at 300 MHz of [1]H Larmor frequency) and DSC further supports the fact that triple-helix structure is formed at the intermediate stage of film formation. From this it follows that part of the structure has probability to become insoluble in water [108] which will, in turn, produce a precipitate forming a dense particle array at the bottom of the surface, and this process may be faster than that of the single gelatin short chains. This is assumed to be the

second stage of the film formation. In this work, the reduction in T_2 and T_1 – both indicating a decrease of mobility – was observed at different depths of the sample from the beginning of this stage. This process has continued and the difference in both relaxation times, but more dramatically in T_2, increased from layer to layer. At the same time, evaporation of the solvent results in an increasing total concentration in the sample. In the final stage, residual solvent has evaporated giving a densely packed gel film with only a small amount of residual water incorporated. The XRD data shows that the dense triple-helix structure that is preferably generated at the bottom of the sample during the evaporation makes a significant difference in the structure of the final film.

4.6. Concentration and humidity effects on gelatin films

In the study of gelatin film formation using single-sided NMR, it was observed that the molecular dynamics of the gelatin polymer varies with the initial concentration of gelatin in water at an early stage of film formation. For the relatively diluted solutions (1% and 2% initial concentration of gelatin in D_2O (w/v)), the distribution of the solute was heterogeneous in the vicinity of the air-sample interface compared to the relatively concentrated sample (10% initial concentration of gelatin in D_2O (w/v)). Note that this effect was observed when the concentration of the diluted solution was more than 10% due to solvent evaporation (see section 4.3.1). This suggests that the initial concentration of the gelatin solution plays a role in the molecular dynamics of the system during drying as well as in the final film although one would expect that two solutions with initial concentration C_1 and C_2, with $C_1 > C_2$ will have the same properties when C_2 will reach the same value as C_1 during drying. Motivated by this fact, gelatin films were prepared from a wide initial concentration range (1% to 30%), and characterized using NMR, DSC and TGA methods to obtain information about the effect of initial concentration of gelatin on the final film. Another purpose of this study was to acquire information about the effect of humidity on these gelatin films. Humidity is an important parameter to be considered for the application of the gelatin film as it varies with the change of climate, for example, relative humidity at tropical climate (averaging around 70%) is different than that of the continental climate (averaging around 40%). Water content in gelatin film varies with the change in humidity and it affects the mechanical properties of the film [84]. In this study, gelatin films were equilibrated at four different relative humidities (RH) (20%, 43%, 75% and 90%) before characterization (see below). Gelatin film was prepared from 9 different initial concentrations (1%, 3%, 5%, 7%, 10%, 15%, 20%, 25% and 30% gelatin in H_2O (w/v)) using the procedure described in section 3.2.1.

Table 4.2: *Relative humidities (RH) produced by saturated salt solutions at room temperature (~21 °C).*

Salt solution	Relative humidity (%)
CH_3COOK	20 ± 2
K_2CO_3	43 ± 1
NaCl	75 ± 1
KCl	90 ± 1

Four sets of samples, each set containing 9 samples based on the initial concentrations, were equilibrated at 20%, 43%, 75% and 90% relative humidities, respectively. To perform this procedure, each set was placed inside a desiccator which was calibrated previously at a nearly constant humidity using a saturated salt solution as shown in table 4.2. The samples were kept in the desiccator for 7 days before each experiment. For the NMR experiment at 40 MHz (^{1}H Larmor frequency), thin strips of the sample were put in the sample tube. Before this, the empty tube was placed in the desiccator at above mentioned humidity for sufficient time. The tube containing the sample was then placed in the desiccator for 7 days. After this time, the tube was covered to avoid humidity exchange with the environment and measured immediately.

Determination of relaxation time

The T_2 and T_1 of the gelatin films were studied at 40 MHz (^{1}H Larmor frequency) using Bruker Minispec spectrometer at room temperature. The CPMG pulse sequence was used to acquire the echo decays and fitted using a biexponential function (Equation 3.2) to obtain the spin-lattice relaxation time (T_2) for the fast and slow decaying components for each of the samples. Figure 4.21 (a) and (b) show the $T_{2,long}$ and $T_{2,short}$ of the gelatin films, respectively, as a function of initial concentration of gelatin solution at four different relative humidities (RH). From figure 4.21 (a) it can be seen that the gelatin films stored at 90% RH show higher values of $T_{2,long}$ (around 3 ms) compared to those stored at 20% RH (around 1 ms). Same kind of trend in the fast decaying components can be seen in 4.21 (b) where the maximum $T_{2,short}$ are around 140 µs and 112 µs of the films kept at 90% and 20% RH, respectively.
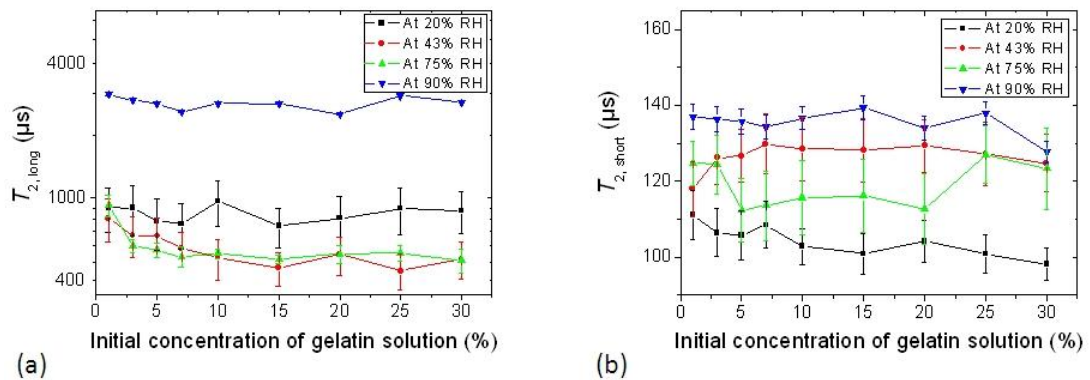
Figure 4.21: T_2 *relaxation times of the* **(a)** *slowly decaying components* **(b)** *faster decaying components as a function of initial concentration of gelatin solutions at different relative humidities.*

Yakimets *et al.* [84] described four types of sorbed water by the gelatin film depending on the relative humidity content: (a) water molecules those sit inside the triple-helix structure and bound to the structure by intramolecular hydrogen bond when the relative humidity is up to 10% (b) water bound to the protein helical fragments at 10-40% RH (c) each triple-helix is covered by a cylinder of bound water layer [46] at 40-90% RH and (d) free (non bound) water at 90% RH and more. Note that the gelatin film is semi-crystalline in nature. A part of the sorbed water molecules is found in the helical structure of the gelatin film as described above. Other water molecules are available in the amorphous region of the film as free water or bonded to the gelatin molecules that compose the amorphous part of the film. At lower RH, the relaxation process is dominated by the ^{1}H of the gelatin polymer. The ^{1}H of the water contributes only as a part of the helix structure. The higher T_2 values of gelatin films at 90% relative humidity are attributed to the water contribution as described in (c) and (d).

Another observation in figure 4.21 is that the T_2 values decrease slightly with the increase of initial concentration of gelatin solution. For instance, gelatin film prepared from 1% concentration and kept at 75% RH shows the $T_{2,long}$ value of 950 µs (figure 4.21 (a)) which is reduced to 550 µs for the gelatin film prepared from 30% concentration at the same relative humidity. Same kind of tendency is observed for the films kept at 43% RH, although, it is not clear for the samples kept at 20% and 90% RH. From figure 4.21 (b), on the other hand, a decrease in the $T_{2,short}$ values with the increase of initial concentration of gelatin solution can be seen in the films kept at 20% RH.

The relative weight of the two contributions, A_{short} and A_{long} (see Equation 3.2) are obtained from the echo decay analysis of the samples. The relative amounts of the fast decaying components, calculated as $A_{short}/(A_{short} + A_{long})$ are shown in figure 4.22. This figure

demonstrates that there is an initial gelatin concentration dependency on the fast decaying components of the films kept at higher relative humidities. At 75% and 90% RH, relative amount of the fast decaying components are lower in the gelatin films prepared from the higher gelatin concentrations compared with those prepared from lower concentrations.
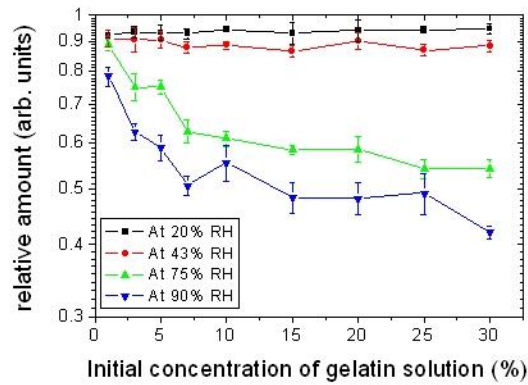

Figure 4.22: *Relative amount of fast decaying components as a function of initial concentration of gelatin solution at different relative humidities.*
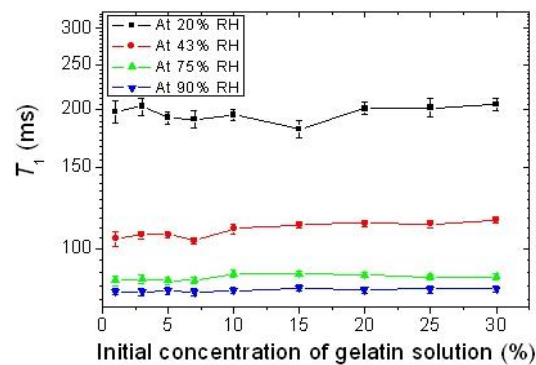

Figure 4.23: *T_1 relaxation times as a function of initial concentration of gelatin solution at different relative humidities.*

An inversion recovery pulse sequence $[180° - \tau - 90°]$ was used with 30 τ values (logarithmically spaced) to measure the spin-lattice relaxation time (T_1). Figure 4.23 shows the T_1 values as a function of initial concentration of gelatin solution at four different relative humidities. In this study, the T_1 values of only one component were detected from all the samples at different humidities. This means that the T_1 relaxation times obtained here refer to the interaction between the excited ^{1}H of the gelatin polymer as well as different types of water molecules in the gelatin film and the lattice molecules

which make up the surrounding structure. The effect of initial concentration is not critical, but remarkable is the fact that the T_1 values are shorter at higher RH of storage as can be seen in figure 4.23. This occurrence can be described by the fact that the relaxation time is related to the lattice through the molecular motions [32]. When the gelatin film is stored at 20% relative humidity, all the water molecules present in the film are bound to the helical structure of gelatin through the intra- and intermolecular hydrogen bond. On the other hand at higher relative humidity, for example at 75% and 90%, free water as well as the water layers (which cover the helical structure) are available. The non-bound water act as a plasticizer which helps the movement of the gelatin molecule. As a result, the correlation time τ_c, a characteristic time required for the movement or tumbling (rotation, vibration or translation) of the molecule, is determined by the relative humidity in the present case. In the solid gelatin films at 20% RH, tightly bound water molecules and the polymer molecules have longer correlation times and the T_1 values are longer than that of the molecules of the gelatin films kept at 90% RH having shorter correlation time.
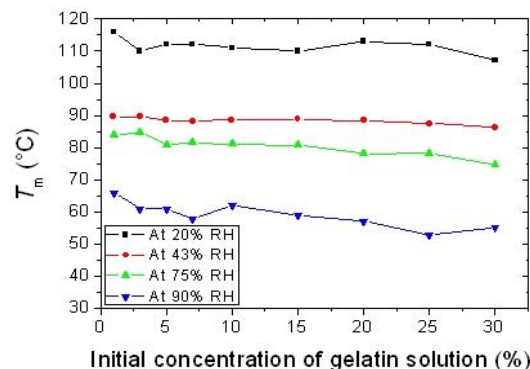
DSC study

Figure 4.24: *Melting temperature (T_m) obtained from the melting peak of the gelatin films as a function of initial concentration of gelatin solution at different relative humidities.*

Gelatin films kept at constant humidity and room temperature was studied using a Perkin Elmer DSC 7 unit. All the thermograms were taken between +25 °C to +140 °C at a heating rate of 10 °C/min. As described in section 4.4.3, the thermogram is characterized by the peak which refers to the melting of the crystal domain originated from the collagen like triple-helix structure in the gelatin. The results are shown in figure 4.24 where melting temperatures (T_m) of the gelatin film at four different storage humidities are plotted as a function of the initial concentration of gelatin solution during film preparation. The fundamental observation in this figure is that the same batch of films stored in the lowest

relative humidity (20%) show the highest T_m values. With the increase in relative humidity, the T_m values decrease and the lowest T_m values are obtained for the batch of films which kept in the highest relative humidity of 90%. The increase in water content in the gelatin film due to the increase in humidity has a plasticizing effect on the film structure. As a result, melting temperatures (T_m) of the gelatin film reduce as the water content increase in the film.

Another observation is that the T_m values of the gelatin films reduce with the increase in the initial concentration of gelatin solution for a set of samples. For the storage relative humidity of 20%, 43%, 75% and 90%, the T_m values of the gelatin films prepared from 1% gelatin in water solution (w/v) are 116 °C, 90 °C, 84 °C and 66 °C, respectively, which are decreased to 107 °C, 86 °C, 75 °C and 55 °C, respectively, for the films prepared from 30% gelatin in water solution (w/v). More diluted a solution with polymer, better is the crystallization due to increased possibility of rearrangement of the biopolymer. As a consequence, less renaturation of collagen occurs when the initial concentration of gelatin solution is high. With the decrease of crystalline structure in the film, the melting peak shifts to a lower temperature [103] which describes this tendency.

TGA study[1]

The thermal stability of the films was measured using a TGA/SDTA 851e (Mettler Toledo). Dynamic scans from 25 °C to 750 °C were carried out at 10 °C/min under helium atmosphere. The TGA graphs of weight loss of the gelatin films obtained from different initial concentrations of gelatin in water (w/v) are shown in figure 4.25 (a) and (c) for the relative humidity 43% and 75%, respectively. The corresponding first derivative related to the rate of weight loss for the gelatin films are shown in figure 4.25 (b) and (d), respectively. The TGA curves of all the gelatin films exhibit two zones of weight loss. The first weight loss at 30-150 °C is attributed to mainly the loss of water, whereas the second weight loss takes place at 250-400 °C which is associated with the protein chain breakage and peptide chain rupture [109].

From the figures 4.25 (b) and (d), it can be seen that the gelatin films prepared from 30% gelatin concentration (30% gelatin film) and stored at 43% and 75% relative

humidity show a slow rate of weight loss in the first zone which is related to water loss and this process is taken place over a long temperature range. On the other hand, gelatin films
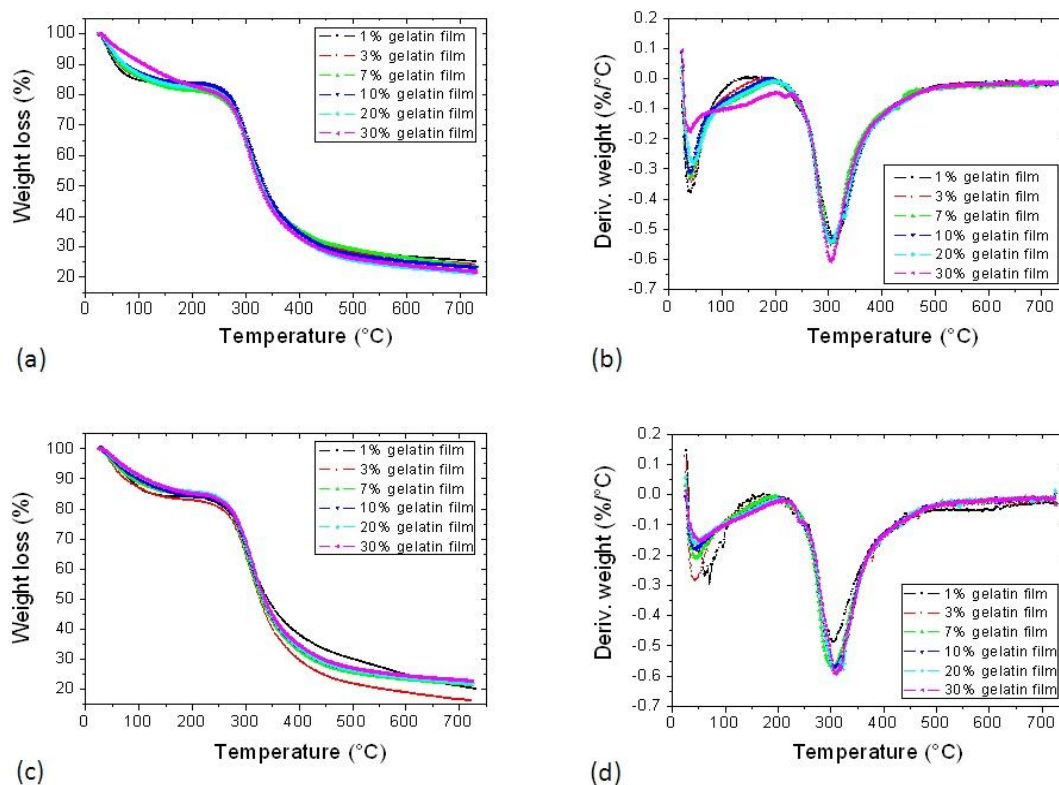

Figure 4.25: (a) *TG and* **(b)** *DTG curves of the gelatin films prepared from different initial concentrations and stored at 43% RH.* **(c)** *and* **(d)** *are the TG and DTG curves of the gelatin films, respectively, stored at 75% RH. 1% gelatin film means the gelatin film prepared from 1% initial concentration of gelatin.*

prepared from 1% gelatin concentration and kept at the same relative humidities show a faster rate weight loss which is taken place over a shorter temperature range compared to that of the 30% gelatin film. In the second zone, it is seen that the weight loss taken place at a faster rate in 30% gelatin film than the 1% film. These experiments demonstrate that the gelatin film prepared from lower initial concentration contains higher degree of renaturation and less amount of water in the film. However, TGA studies do not show any particular trend regarding the effect of 43% and 75% RH on the gelatin films.

4.7. Conclusions

Time-dependent NMR profiles in conjunction with relaxation times measurements were carried out in different systems of relatively low and high concentration solutions of gelatin during the process of film formation. D_2O was chosen as a solvent probing in this way the dynamics of the system, observing only the protons from gelatin. Any effect of

exchange between labile protein protons and ^{2}H from D_2O was ruled out due to the fact that it occurs at very early stages of the film formation process. Using three different gelatin solutions according to the initial concentration, namely 1%, 2% and 10% gelatin in D_2O (w/v), it was found that close to the final drying stage, the T_2 constant of the film near the substrate decreases faster than in the vicinity of the air-sample interface. Furthermore, it was shown using XRD that this heterogeneity persists in the final film. In a separate study using high-field NMR in combination with DSC, it was observed that the renaturation process during the gelatin film formation takes place after a certain evaporation time which continues for a short time period compared to the total time of film formation.

This overall proves that heterogeneous drying happens in this kind of systems. Moreover, a new aspect of this dynamical process for the relatively diluted solution is revealed by the fact that the T_2 constant is found to be faster in the vicinity of the air-sample interface when compared with the middle part of the sample. This could be explained by the fact that for a dilute gelatin solution, the solute is spatially heterogeneously distributed due to the evaporation process. It can be concluded that heterogeneity in the drying of gelatin gels have two different sources, one being the renaturation, resulting in precipitation of collagen, and the other one the concentration gradient developing in diluted systems. The first persist in the final film while the second seems to vanish. This is concluded from the observation of the T_2 dependence on height at the later stages of the film formation process. At these times, T_2 constants have a monotonous growing tendency upon height.

The study on the gelatin films prepared varying the initial concentration of gelatin in water and stored at different relative humidities revealed that the relaxation and thermal properties of the film depend on the humidity of the environment. This experiment also confirmed the minor effect of initial solution concentration on the properties of prepared gelatin film.

Chapter 5

Starch film formation study

If you have an apple and I have an apple and we exchange these apples then you and I will still each have one apple. But if you have an idea and I have an idea and we exchange these ideas, then each of us will have two ideas.

George Bernard Shaw

5.1. Introduction

Starch granule is composed of three different regions which are amorphous region, crystalline lamellae and amorphous growth ring. At room temperature, a starch granule is not soluble in water because of the stable semi-crystalline structure. However, it undergoes limited swelling (reversible), presumably due to hydration and swelling of the amorphous regions. It is known that amylopectin (figure 3.2 (b)), due to its highly branched open structure, allows access to hydrogen-bonding solvent molecule. Consequently it is more disrupted in water or another solvent able to form hydrogen bonding than amylose, which has a tightly packed structure. The interaction of starch granules with hot water is different as in water at room temperature. For example, when the starch granules are heated in excess water beyond a critical temperature depending on the type of starch, an irreversible change is taken place known as gelatinization [16]. This involves swelling of the granules, crystallite melting, viscosity development and solubilization. During swelling, the amorphous phase of granular starch is fully plasticized by the solvent and amylose (figure 3.2 (a)) starts to leach. This process is influenced by the increase in temperature. Depending on the initial concentration of starch in water, a precipitation or a white elastic gel (prepared from a concentrated system) can be obtained when the system is left at rest and cool down to room temperature [68]. Apart from the

concentration effect, the chain length of amylose influences this phenomenon. Amylose having a degree of polymerization (DP) <110 precipitate from aqueous solutions at all temperatures. Amylose of DP 250-660 precipitates or forms gel, depending on the concentration and temperature. For DP >1100 predominantly form gels rather than precipitate [16].

Upon cooling, the starch suspension forms an elastic gel when the initial starch concentration is high. This involves interactions that occur mainly by hydrogen bonding between starch chains. This process is known as retrogradation [16]. In this process, amylose molecules start to be prone to double-helix formation with the same type of molecules as well as with the long branches of amylopectin [110]. The amylopectin molecules also undergo through a recrystallization process with the same type of molecules. As a result, gelatinized starch begins to reassociate in an ordered structure. In case of diluted starch suspension, the supernatant consists of mainly amylopectin. It may also contain highly branched non-amylopectin type polysaccharides and small amount of amylose. The precipitate contains mainly amylose and a part of branched amylopectin [16].

Although the gelation process as well as the starch gel itself has been studied extensively [111]-[114], not much attention has been given to studying the film formation process. In this chapter, a microscopic dynamic study of starch film formation is demonstrated which accompany the evolution from the initial polymer suspension (starting from a dilute system) or gel (starting from a concentrated system) to final film. Using low-field NMR the new feature reported in the present work is the experimental demonstration of the different molecular dynamics during starch film formation starting from two different initially concentrated systems. XRD was employed in order to investigate structural differences in the dried films. This information is correlated with the NMR studies.

5.2. Samples

1% and 5% aqueous suspensions of starch were prepared as described in section 3.2.1. Glycerol was used as a plasticizer (20g/100g of starch) to prepare each sample. A micro camera was used to follow the reduction of the sample height due to evaporation in sample *a* and *b*. Sample *c* and *d* were used to study the film formation in the single-sided NMR scanner. A large portion of sample *c* was cast on a Petri dish and a final film of around 100 µm thickness was obtained. In this case, the evaporation time was longer than that of the other samples. For sample *e* and *f*, the T_2 values of the samples were obtained using an accessible vertical range of 4.1 mm of the single-sided NMR scanner which will be discussed below. Table 5.1 summarized the samples used in this study.

Table 5.1: *Different starch samples prepared using H_2O or D_2O as a solvent. Glycerol was added as a plasticizer (20g/100g starch) to prepare each sample.*

Sample	Initial concentration (%) of starch in the solvent (w/v)	Solvent	Initial physical status of the sample	Study	Thickness of the final film (µm)
a	1	H_2O	suspension	Using micro camera	---
b	5	H_2O	gel	Using micro camera	---
c	1	H_2O	suspension	Profiling at 11.7 MHz (^{1}H) and XRD	130 ± 15
d	5	H_2O	gel	Profiling at 11.7 MHz (^{1}H) and XRD	170 ± 10
e	1	H_2O	suspension	T_2 study at 11.7 MHz (^{1}H)	---
f	1	D_2O	suspension	T_2 study at 11.7 MHz (^{1}H)	---

5.3. Film formation study using micro camera

A micro camera was used to follow the real time evaporation from the sample *a* containing 1% starch in H_2O (w/v) and sample *b* containing 5% starch in H_2O (w/v), respectively. The camera was placed at a fixed distance from the Petri dish and pictures were taken at different drying stages. A set of pictures is shown in figure 5.1 for the sample *a*. Figure 5.1 (a) shows the fresh starch sample right after casting and it looks homogeneous all over the sample height. After 15 min, two distinct layers are visualized which can be seen in figure 5.1 (b). The lower layer is a white, gel like and nontransparent substance. This layer contains mostly amylose which precipitates in this kind of system as explained in section 5.1. On the other hand, the upper layer is a solution which contains mainly amylopectin and relatively small amount of amylose and highly branched polysaccharides. After 2 hours of casting, as shown in figure 5.1 (c), the separation of the layers is clearly visible and the height of the lower layer is decreased. Figure 5.1 (d), (e) and (f) show a reduction of the height of the upper layer due to the evaporation of the

solvent. There is a minor reduction of the height of lower layer as well which indicates the continuation of packing of solute and removal of the solvent from the lower layer.
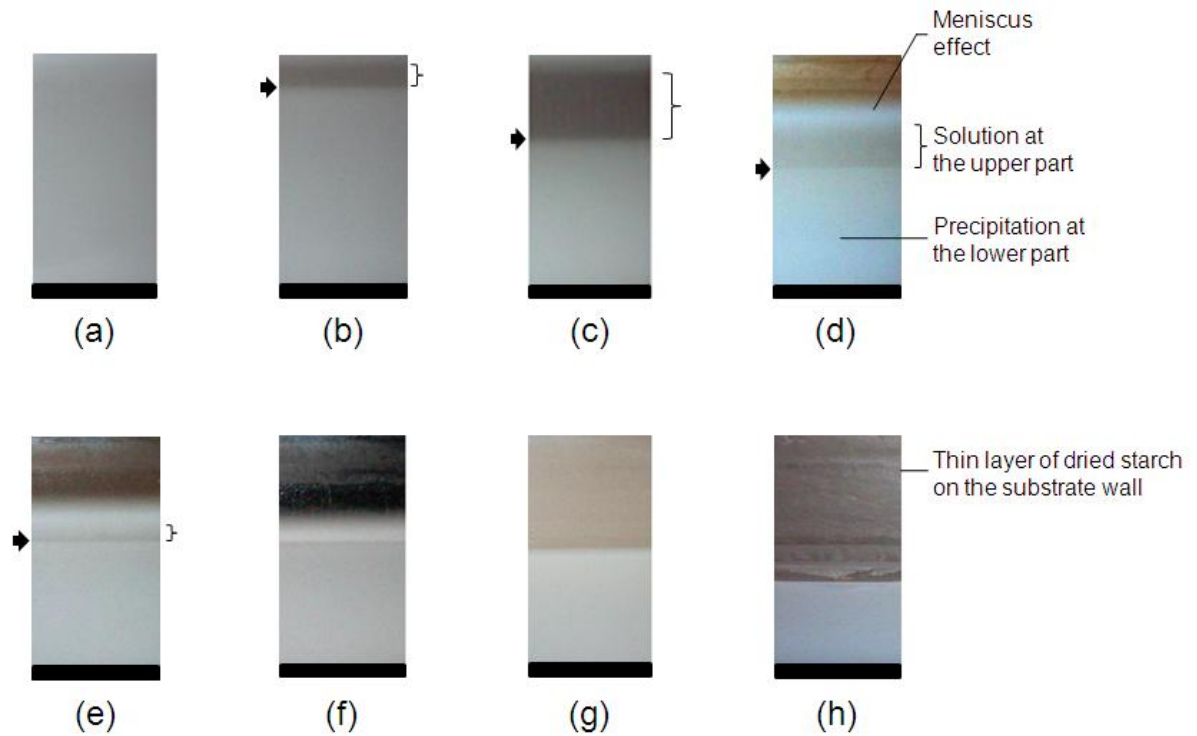

Figure 5.1: *Sample a containing 1% starch in H_2O at different stages of drying. The evolution time increases from (a) to (h).The arrow shows the phase separation whereas the bracket shows the upper solution layer. The different backgrounds in the upper part of the pictures are due to the reminiscent light at different of the day.*
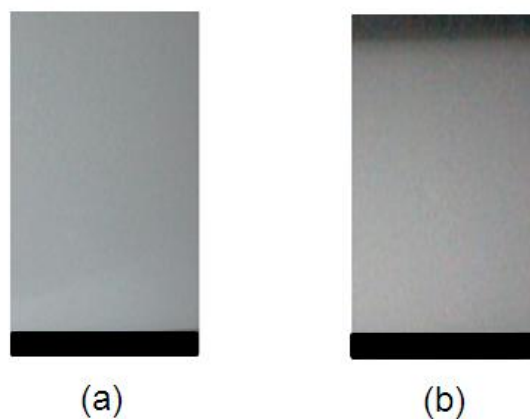

Figure 5.2: *Sample b containing 5% starch in H_2O at different stages of drying. The evolution time increases from (a) to (b).*

In figure 5.1 (g), it is seen that the upper layer of the sample is not detectable anymore after a certain time of evaporation. After that, the lower layer continues to shrink with time as can be seen in 5.1 (h). A dried thin layer of starch can be observed on the

wall of the Petri dish. The camera was fixed in order to cover the complete sample from the beginning of the evaporation process. A meniscus on the top of the sample is clearly visible in figure 5.1 (d) which blur the air-sample interface of the sample as can be seen in figure 5.1 (e) and (f) as well. The concentration of the non-volatile components will be increased at the upper part of the sample with the solvent evaporation. After a certain drying time when the solvent is mostly evaporated from the upper part (as shown in figure 5.1 (f), in the present case), these components will apparently increase the thickness of the lower part of the sample. This effect is not seen which might be due to the lack of contrast or the presence of meniscus as described above.

Figure 5.2 shows the sample *b* which is prepared using 5% starch in H_2O (w/v) and cast on a Petri dish. The viscosity of this sample was high after gelatinization and it formed a gel as can be seen in 5.2. Due to retrogradation, amylose and amylopectin present in the system form an ordered structure. As the solvent evaporates, the sample thickness decreased with time and the film was formed.

5.4. Real time film formation study using single-sided NMR scanner

Profiling of the samples

When the height of the starch sample was approximately 1 mm following partial evaporation of H_2O, it was placed on to the single-sided NMR scanning device. The starting time of the profile experiments is considered as time, t=0 in the following discussion. For sample *c*, this time corresponds to 78 h after the casting time whereas 38 h had elapsed for sample *d*. After 78 h of casting time, water was already evaporated from the top layer of sample *c* (corresponding to the phase rich in amylopectin) and became similar to sample *a* in figure 5.1 (h). On the other hand, sample *d* was in gel state after 38 h.

For both samples, 23 consecutive experiments, i.e. complete profiles, were carried out as shown in figure 5.3 (a) and (b) for sample *c* containing 1% starch in H_2O (w/v) and sample *d* containing 5% starch in H_2O (w/v), respectively. The direction of scanning was from top (sample-air interface) to bottom (sample-substrate interface). The position of the sensor was moved in steps of 100 μm until 277 min and 417 min for sample *c* and *d*, respectively, after which it was reduced to 50 μm. The figure shows that the height of the samples exceeds the scanning range of the machine. The resolution was fixed to 50 μm in both cases. 12 and 15 points were required for sample *c* and *d*, respectively, to cover the

space between the substrate – defined as zero in the following discussion – and the sample-air interface. For sample *c*, with a pulse separation of 87.5 μs, 32 scans, 2048 echoes and 8 s repetition time, a total time of ~256 s was required for the acquisition of data at one position, i.e. one individual slice. That means the time for scanning the full profile was ~52 min. This period was followed by a waiting time of 23 min. In sample *d*, the repetition time was reduced to 7 s and the number of scans was the same, so that each profile took 56 min to be completed; this period was followed by a waiting time of 34 min before the beginning of the following slice.
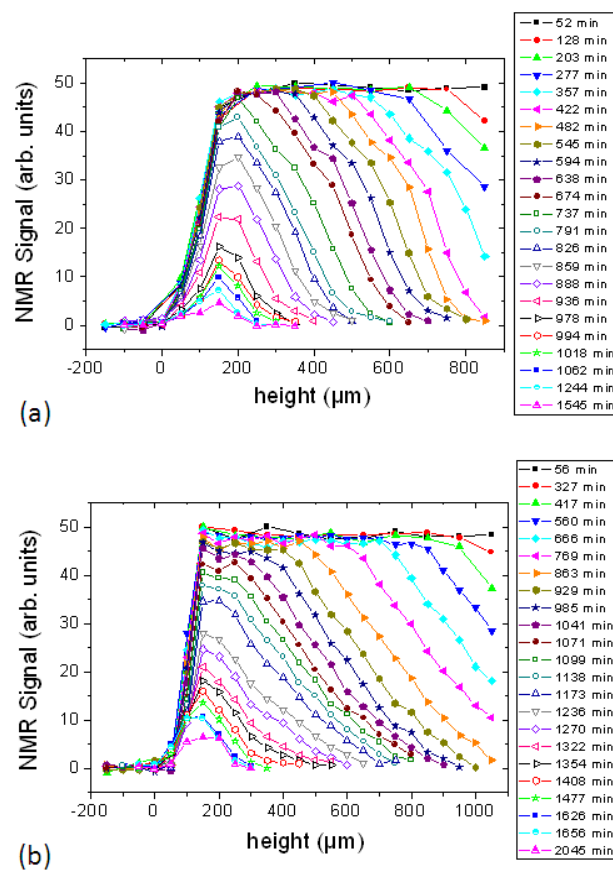

Figure 5.3: *NMR profiles of the starch-water system at different drying times:* **(a)** *Sample c containing 1% starch in H_2O (w/v) and* **(b)** *Sample d containing 5% starch in H_2O (w/v). Each sample contains glycerol (20g/100g of starch) as a plasticizer.*

With the solvent evaporation in both samples, less time was required to accumulate one profile as less repetition time was required at the later stage. The repetition time was always adjusted to be ≥ 5 T_1 for the full recovery of the magnetization throughout the experiment. Although sample *d* contains higher amount of starch and glycerol compared with sample *c*, both experiments show same maximum intensity (within experimental error) in the initial profiles. A reduction in the signal intensity is observed after about 737 min and 929 min for sample *c* and *d*, respectively, after being constant

before the above mentioned time. This is due to the hardening of the sample with the corresponding decrease of the relaxation time T_2. It is important to mention that the first echo is forming at 87.5 µs. For solid-like samples, a great portion of the signal might decay inside this time as it was observed in case of gelatin samples (chapter 4). It is seen that the right edge of the profile curve (air-sample interface) shows a gradual decay. This decay is smoother in sample *d* compared with that of sample *c* as can be seen in figure 5.3. On the other hand, the signal intensity in the substrate-sample interface exhibits a sharp decay in all profiles.

Determination of sample shrinking rate

The decrease in the sample height as a function of evolving time is shown in figure 5.4 (a) and (b) for sample *c* containing 1% starch in H_2O (w/v) and sample *d* containing 5% starch in H_2O (w/v), respectively. Both samples contain glycerol (20g/100g of starch) as a plasticizer. The sample height has been calculated as the width of the profiles is defined by the values of 5% of the maximum intensity where the signal can still be distinguished reliably from the noise level (see section 4.3.1). Based on this assumption, the rate of evaporation $\dot{E}$, defined as the slope of the fitted lines, was calculated for each sample.
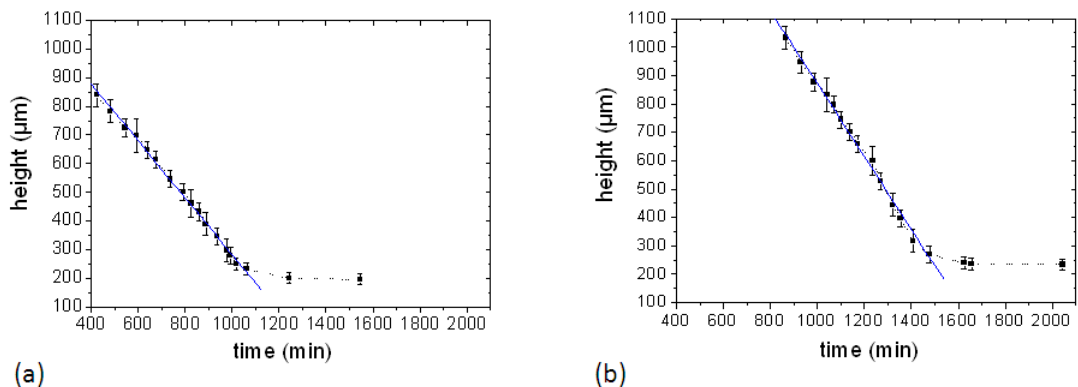

(a)   (b)

Figure 5.4: *Film thickness estimated from the profile widths in figure 5.3, as a function of drying time. Linear fits to the experimental data are shown.* **(a)** *Sample c containing 1% starch in H_2O (w/v) and* **(b)** *Sample d containing 5% starch in H_2O (w/v). Each sample contains glycerol (20g/100g of starch) as a plasticizer.*

At the beginning of drying, it is seen that the profile width decreases uniformly with time in both samples (figure 5.4). As like as the gelatin samples (chapter 4, section 4.3.1), these samples show a single evaporation regime which indicates a smooth evaporation of the solvent during the experiment period. The evaporation rates calculated for sample *c*

and d are 1.6×10^{-8} m/s and 2.1×10^{-8} m/s, respectively. After 1070 min and 1480 min, there is no notable change in the profile widths of sample c and d (within the experimental error) until the end of the experiment as can be seen in figure 5.4 (a) and (b), respectively.

The final profile width of these samples is in the range of 230 μm although the actual thickness of the films is lower than this calculated value as can be seen in table 5.1. After the profile experiments, all the films were stored in the same environmental conditions as it was during the drying period to ensure complete drying of the film.

Determination of T_2 at different heights

For both samples, the CPMG echo decay obtained from each profile point is monoexponential at the earlier evaporation time. Accordingly, a mono-exponential function (Equation 3.1) is fitted to the experimental data to obtain the spin-spin relaxation time (T_2) constant. At a later stage of drying, the decay curves obtained from the bottom to a certain height of the sample could be fitted with two exponential decays (Equation 3.2).
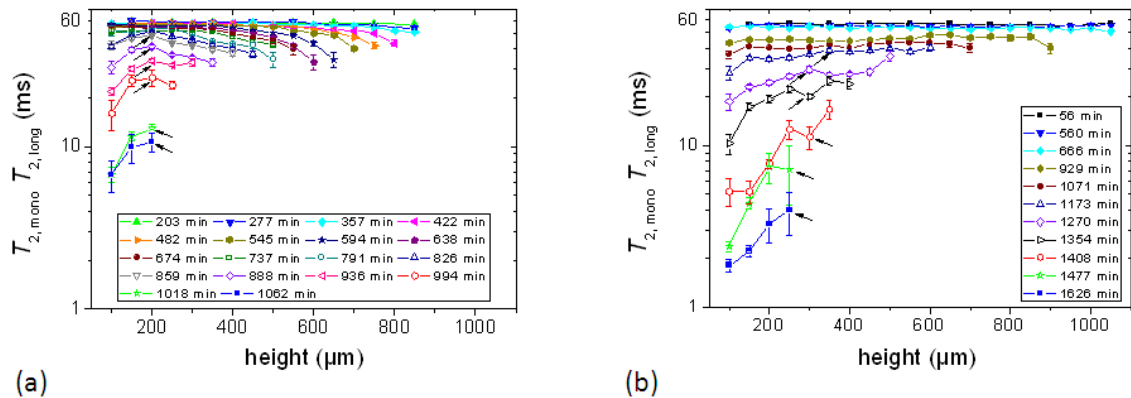

Figure 5.5: *T_2 constants at different heights of the sample.* **(a)** *Sample c containing 1% starch in H_2O (w/v) and* **(b)** *Sample d containing 5% starch in H_2O (w/v). Each sample contains glycerol (20g/100g of starch) as a plasticizer. Layer positions correspond to coordinates introduced in figure 5.3. At the later stage of drying, the echo decays were fitted with two exponential decay function from the bottom of the sample to a certain height which is showed by the arrow. In the case of bi-exponential decay, the effective T_2 data showed in both figures correspond to the slow decaying components.*

Figure 5.5 (a) and (b) show the T_2 values obtained either from the single component at an earlier stage or a combination of single and slow decaying components (long component) at later stage during the total drying time with respect to different positions in the sample c containing 1% starch in H_2O (w/v) and sample d containing 5% starch in H_2O (w/v), respectively. Both samples contain glycerol (20g/100g of starch) as a plasticizer. In general, both samples have nearly the same T_2 values at the beginning of

the experiment as can be seen in figure 5.5. As it was observed in the case of gelatin samples (chapter 4), the T_2 values decrease with the time of film formation in both starch samples until the end of measurement period. For example, starting from around 60 ms in sample *c*, the lowest T_2 value achieved is around 7 ms after 1062 min of drying whereas in sample *d*, the lowest T_2 value is around 2 ms after 1626 min of sample drying. The decrease of T_2 values with time attributes to the film formation process and solvent evaporation.

There are two types of dependencies of T_2 values on the position within the sample *c* are observed during the evaporation process. Until around 890 min of drying, the T_2 values gradually decrease with the increase of sample height which follows a definite tendency (see below). The first T_2 profile shows that there is a slight decrease in T_2 values (~60 ms to ~55 ms) with the increase of height. This difference increases at the later stage of evaporation. For instance, the T_2 value in the sample height of 100 µm is ~57 ms which is reduced to ~34 ms at the height of 650 µm after 594 min of sample drying. Another observation in this sample is that the change in T_2 values is less pronounced with the increase of sample height and drying time at the bottom part of the sample. For instance, the T_2 value after 638 min of drying is ~55 ms at 100 µm which is slightly reduced to ~52 ms at 400 µm height. Note that at the beginning of the experiment, the highest T_2 value observed in the lower part of the sample is ~60 ms. This indicates a slow evolving of the sample at the bottom part in sample *c*. On the other hand, the T_2 values in the height 500 µm and 600 µm are ~47 ms and ~33 ms, respectively, in the same T_2 profile. From these observations, it becomes immediately obvious that the gradual decrease in T_2 value in a profile mainly takes place at the few hundredths of µm near to the air-sample interface in sample *c* until around 740 min of drying (figure 5.5 (a)). From 888 min onwards, there is another kind of dependency of the T_2 values on the height of sample *c* which shows that the bottom part of the sample has the lowest T_2 value.

The T_2 value of sample *d* for different heights of the first T_2 profile is ~56 ms as can be seen in figure 5.5 (b). After 666 min the T_2 values begin to vary from layer to layer in the sample, a similar tendency showed by the sample *c* at the later stage of drying. From

1354 min onwards, T_2 value decreases sharply in the bottom part of the sample. For example, in the height of 350 µm, T_2 value is ~17 ms which is decreased to ~5 ms at the bottom layer after 1408 min. Note that sample *d* does not show the decrease in T_2 values with the increase of sample height during the entire experiment time as it is seen in the earlier stage of film formation in sample *c*.
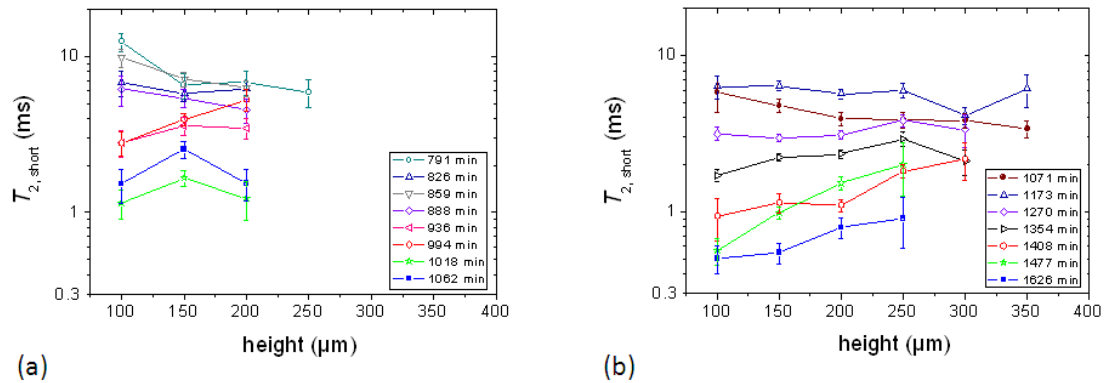

Figure 5.6: *T_2 constatns of the fast decaying components at different heights of the sample.* **(a)** *Sample c containing 1% starch in H_2O (w/v) and* **(b)** *Sample d containing 5% starch in H_2O (w/v). Each sample contains glycerol (20g/100g of starch) as a plasticizer. Layer positions correspond to coordinates introduced in figure 5.3.*

Both samples show a second component during the later stage of film formation (after 791 min and 1071 min of drying time for sample *c* and *d*, respectively) from the bottom to a certain height of the sample. Figure 5.6 (a) and (b) show the short T_2 values (named as $T_{2,short}$) obtained from the fast decaying components with respect to different positions in sample *c* and *d*, respectively. In sample *c*, the highest $T_{2,short}$ value of the fast decaying component is ~13 ms after 791 min of drying time which is reduced to ~1 ms after 1062 min. In sample *d*, on the other hand, the $T_{2,short}$ value decreases from ~6 ms to ~0.5 ms in between 1071 min and 1626 min of the experiment time. In this sample, it is seen that the $T_{2,short}$ value is showing the same type of depth dependence as was found for the slow decaying components in figure 5.5 (b). This means that the fast decaying component is also different at the bottom layer than that of the intermediate layer in sample *d*. The $T_{2,short}$ values of sample *c*, however, do not show such a clear tendency as seen in figure 5.6 (a).

An earlier study (section 5.3) reveals that sample *c* formed a suspension after it was cast whereas sample *d* was a gel at the same time and the evaporation tendency of these two systems was different at the beginning of film formation. From profile experiment, one can see that the molecular mobility in the vicinity of the air-sample
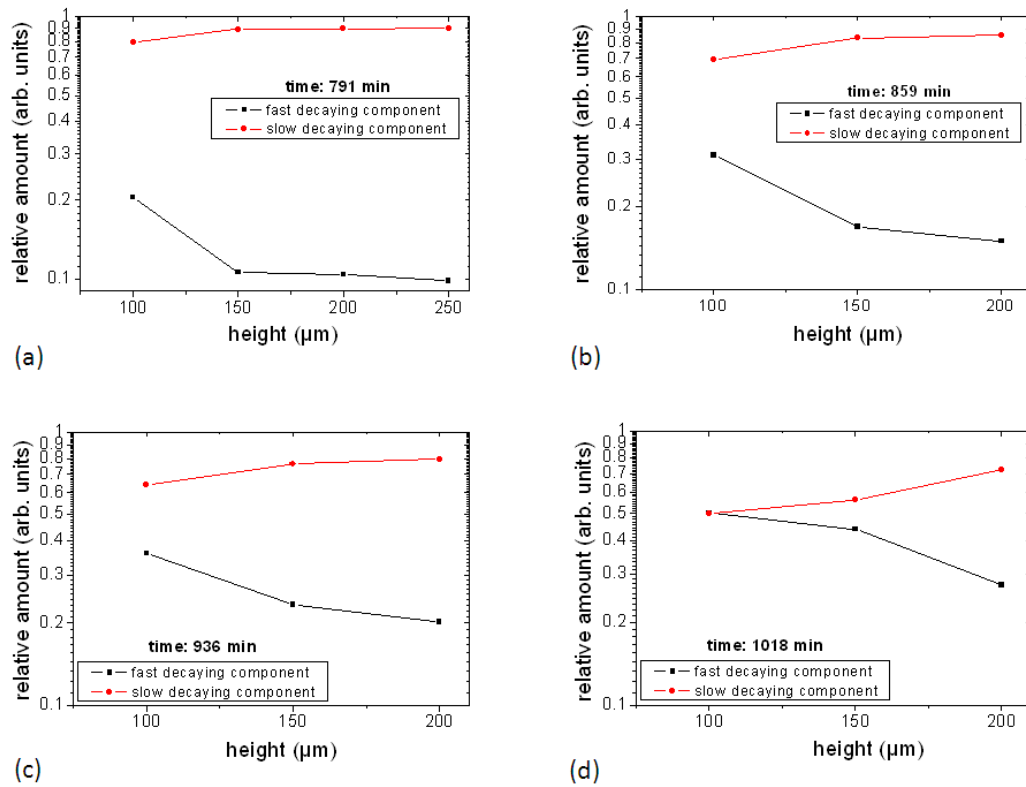
Figure 5.7: *Change in relative amount of fast and slow decaying components with time in sample c containing 1% starch in H₂O (w/v). Layer positions correspond to coordinates introduced in figure 5.3.*

Figure 5.8: *Change in relative amount of fast and slow decaying components with time in sample d containing 5% starch in H₂O (w/v). Layer positions correspond to coordinates introduced in figure 5.3.*
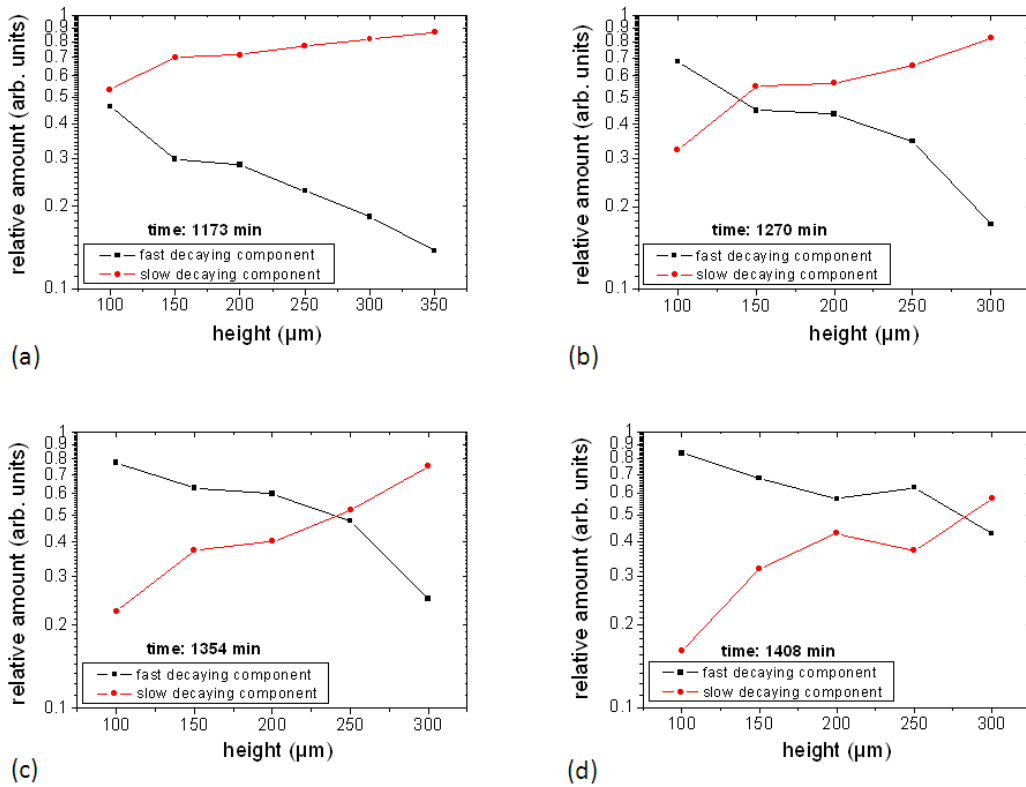
interface decreases during evaporation of sample *c* at an earlier time. This effect is absent in sample *d*. At a later stage, it is observed in both samples that the mobility increases with the sample height, especially in 5% starch containing sample (sample *d*). The above T_2 study confirms that molecular mobility of these systems (see section 4.3.1) is different even though both samples are in gel state during the study.

The weight of the two contributions, A_{short} and A_{long}, can be estimated from the echo decay analysis (Equation 3.2) and the relative amounts $A_{(i,j)}/(A_i + A_j)$ as obtained for sample *c* and *d* where $\{i,j\} = \{short, long\}$, are plotted in figure 5.7 and 5.8, respectively. For both samples, the relative amount of the fast decaying component is increasing with time whereas it is decreasing for the slow decaying component. Sample *d* shows the higher relative amount of the fast decaying component than that of sample *c* at the end of the measurement period. In sample *c* (figure 5.7), a tendency is seen where the relative amount of the slow decaying component is lower at the bottom of the sample than the top of the sample. This tendency is more prominent in sample *d* as can be seen in figure 5.8. Note that, while the $T_{2,short}$ values show different trends for both samples (short component more or less independent of height in sample *c*, getting shorter towards bottom in sample *d*), the relative weight of the short component becomes bigger towards the bottom in all cases. These results support the notion that the bottom part of the sample has slower dynamics due to the presence of higher relative weight of the short components than the top part.

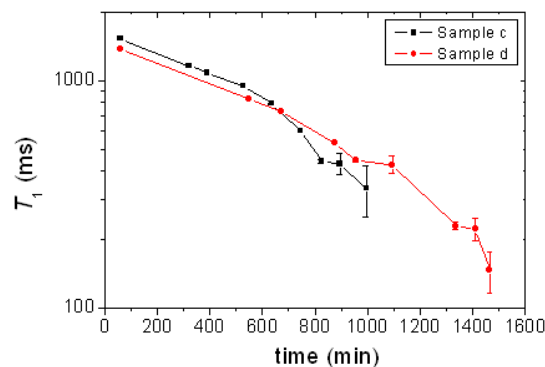## Determination of T_1 during film formation

Figure 5.9: *Evolution of T_1 with drying time in sample c and d. Layer positions correspond to coordinates introduced in figure 5.3.*

Longitudinal relaxation times (T_1) were measured on a wider slice (300 μm) in the centre of each sample at regular intervals of drying time during the profile measurements. A saturation recovery pulse sequence $[90° - \tau - 90°]$ [74] was used with 18τ values (logarithmically spaced) to obtain the T_1 values. At the beginning of the experimental period, the T_1 values for sample *c* and *d* are ~1530 ms and ~1377 ms, respectively, as can be seen in figure 5.9. The T_1 value is found to decrease during the drying process of the samples. After 995 min and 1465 min of evaporation of sample *c* and *d*, respectively, the T_1 values are reduced to ~336 ms and ~146 ms, respectively.

Table 5.2 summarize the limiting value of T_1 and T_2 of 1% and 5% starch systems during film formation.

Table 5.2: *The approximate T_1 and T_2 values of 1% and 5% starch systems in water (w/v). Glycerol was added as a plasticizer (20g/100g starch) to prepare each sample.*

Sample (starch in water (w/v))	At early stage			At final stage		
	T_2 (ms)		T_1 (ms)	T_2 (ms)		T_1 (ms)
	long	short		long	short	
1%	60	13	1530	7	1	336
5%	60	6	1377	2	0.5	146

Determination of T_2 of fresh starch samples

Aqueous suspension of 1% starch sample was prepared using H_2O (sample *e*) or D_2O (sample *f*) as a solvent. Both samples contained glycerol (20g/100g of starch) as a plasticizer. Each sample was placed on top of the single-sided NMR scanner when a precipitation was clearly visible. In this study, a 7 mm thick spacer was used. This spacer allows an accessible vertical range of 4.1 mm. Note that for all the remaining results obtained in this thesis, a thicker spacer (9 mm) was used to locate the RF coil close to the sample (see section 3.3). In this way more sensitivity was gained.

CPMG pulse sequence [71] was used to obtain the T_2 values from different heights of the sample. Figure 5.10 (a) and (b) show the measured T_2 values for sample *e* and *f*, respectively. From figure 5.10, it is seen that the T_2 values are nearly homogeneous at

different heights of the sample. The T_2 value of the upper part of sample *e* is ~60 ms which is more or less the same as the T_2 values of sample *c* and *d* at the beginning of the profile experiment as can be seen in figure 5.5. The T_2 values obtained in the fresh sample *e* might be affected by the diffusion or mobility of the molecules. With time, mobility decreases in the sample and this effective T_2 value approaches to the real value.
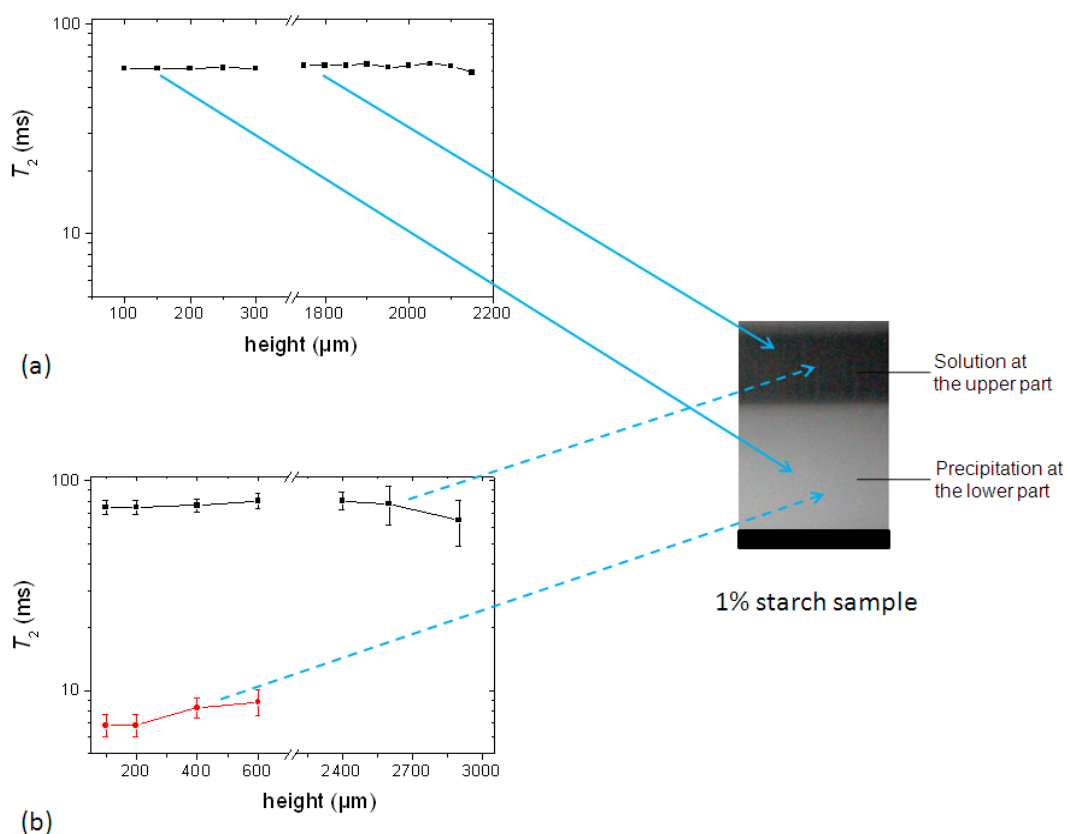

Figure 5.10: *T_2 constants at different heights of* **(a)** *Sample e containing 1% starch in H_2O (w/v) and* **(b)** *Sample f containing 1% starch in D_2O (w/v). Glycerol (20g/100g of starch) was used as a plasticizer.*

From figure 5.10 (b) it is clear that sample *f* shows the T_2 relaxation of two components. The lower precipitation part of this sample shows a $T_{2,short}$ of ~7 ms which increases a little with sample height and a $T_{2,long}$ of ~75 ms. On the other hand, the upper solution part shows only one component with a T_2 of ~75 ms which can be the residual contribution from water/mobile parts. Note that, this sample contains HDO molecules obtained from the exchangeable proton from the starch polymer [115] and the glycerol plasticizer which may contribute to the higher T_2 value. Taking into account that the concentration of glycerol in the total sample is around 0.2% at the beginning and 3

protons among 8 protons of glycerol are exchangeable, the % of proton in the glycerol may be less than the total residual protons in the sample and thus the contribution of glycerol is negligible in the signal.

5.5. Film characterization

The final films from sample *c* containing 1% starch in H_2O (w/v) and sample *d* containing 5% starch in H_2O (w/v) were stored keeping the same environmental conditions of the drying process for two weeks and then measured using NMR and XRD techniques.

5.5.1. Single-sided NMR study

The T_2 experiments were performed for the films obtained from sample *c* containing 1% starch in H_2O (w/v) (named as film *c*) and sample *d* containing 5% starch in H_2O (w/v) (named as film *d*). The results are shown in figure 5.11. The echo time used in these experiments was 114.5 µs. The remarkable fact is that T_2 is uniform within the experimental error as shown in this figure when the film is practically ready. In case of gelatin sample (chapter 4), it was found that a fast decaying component (characteristic of solid like signals) could be distinguished in the dried samples and a large portion of the signal of the sample was decayed below 100 µs which could not be detected in the single-sided NMR. As same, the T_2 values obtained in figure 5.11 can be the transverse relaxation time of the longer component of a solid film.
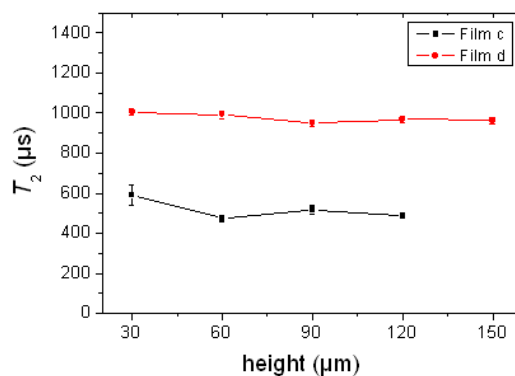

Figure 5.11: *T_2 constants at different heights of the completely dried film c and d prepared from sample c containing 1% starch in H_2O (w/v) and sample d containing 5% starch in H_2O (w/v), respectively. Glycerol (20g/100g of starch) was used as a plasticizer during film preparation.*

The values of T_2 are ~550 µs and 1 ms for film *c* and *d*, respectively. The precipitation as observed during the film formation in sample *c* might help to form a denser structure in the final film. In addition, initial glycerol content in the total system (0.2% in sample *c* compared with 1% in sample *d*) may have an influence on the polymer molecules during the film formation. To estimate the residual water content in film *c* and *d*, the films were dried in oven at 105° C until a constant weight was obtained. Note that both films were calibrated at 43% RH before the experiment. It was found that the moisture content (dry weight basis) in film *c* (around 11%) is slightly less than film *d* (around 15%). All these effects might influence the polymer chain mobility to be lowered in film *c* which explains the lower T_2 value in this film. A Comparison with the other polymer films studied in this work shows that the T_2 values of dried starch films are higher than that of the gelatin films (chapter 4) and PVOH films (chapter 6).

5.5.2. XRD study

The X-ray diffractograms of the films obtained from sample *c* containing 1% starch in H_2O (w/v) and sample *d* containing 5% starch in H_2O (w/v) are shown in figure 5.12. The XRD patterns were acquired for both sides of each film using fixed angle incident beam method (section 3.3) as it was carried out for gelatin films (chapter 4). The amorphous contribution has been subtracted [116].
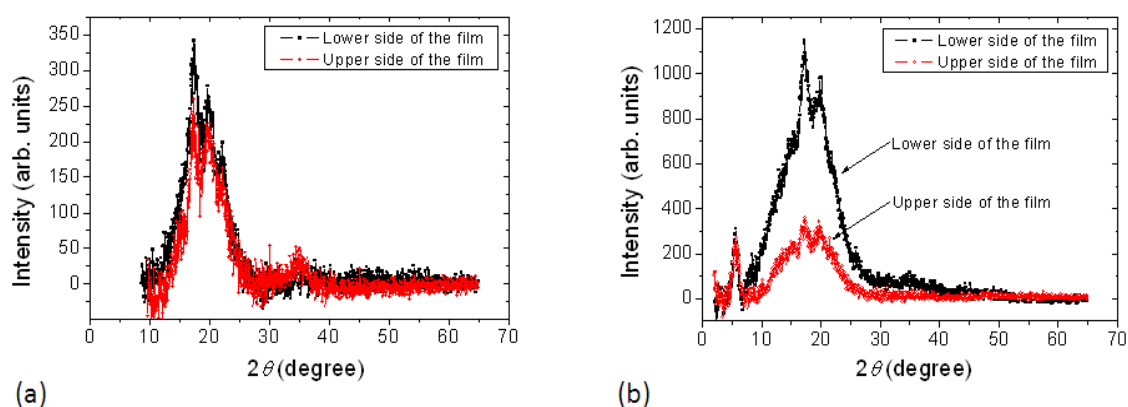

Figure 5.12: *X-ray patterns of films prepared from* **(a)** *sample c containing 1% starch in H_2O (w/v) and* **(b)** *sample d containing 5% starch in H_2O (w/v).*

From literature [117], it is found that the crystalline structure of starch is characterized by specific diffraction peaks observed at 9.9°, 11.2°, 15°, 17°, 18.1° and 23.3° at 2θ Bragg angles for A-type crystallinity (see section 3.1.1) and 5.6°, 15°, 17°, 22° and 24° at 2θ Bragg angles for B-type crystallinity. In this study, the X-ray diffraction

of the film obtained from sample *c* reveals two prominent peaks at 2θ ~17° and 20.5°. There are other two peaks at 2θ ~15° and 22° which cannot be seen clearly. Because of low signal to noise, the diffractogram until 2θ ~8° is subtracted in figure 5.12 (a). On the other hand, sample *d* shows prominent peaks at 2θ ~5.6°, 17° and 20°. Same as sample *c*, the peaks at 2θ ~15° and 22° cannot be seen clearly. Assignment of these peaks suggests that the starch films obtained from the film formation study contain B-type crystallinity. This observation is in agreement with the study described, for example, in [118] where B-type crystallinity was observed (including the peak at 2θ ~ 20°) in starch films prepared from corn starch. Note that B-type crystallinity is found in some tuber and cereal starches rich in amylose. The B-type pattern has relatively less dense packed double helices than the A-type pattern. Figure 5.12 (a) shows that both sides of the XRD pattern for sample *c* is nearly the same whereas the film obtained from sample *d* shows (figure 5.12 (b)) that the lower side of the film has a higher intensity in the peak compared with that of the upper side of the film. In figure 5.12 (b) the significant fact is that the peak at 2θ ~5.6° shows the same intensity for both sides of the film obtained from sample *d* although there is a significant difference in intensity in the peaks at 2θ ~17° and 20° at both sides of the same sample. The upper side of this film may contain higher amorphous region which will scatter the X-ray more than the lower part of the film. During the film formation at a later stage in sample *d* (section 5.4), a decrease in mobility of the sample was observed at the lower part revealed by the increase of T_2 relaxation time with sample height. The XRD data further complements the T_2 effect as observed during the film formation study. Note that a similar observation was seen in the gelatin films as described in section 4.4.2.

5.6. Proposed mechanism of starch film formation

In this study, two different tendencies in the molecular mobility are observed during the film formation processes. The mechanism that account for these observations takes place necessarily during film formation. It is known that when the semi-crystalline structure of starch granule is treated in hot water, the linear amylose can diffuse through the granule more readily than the highly branched amylopectin. When the temperature of the system is reduced, the diluted starch solution forms a precipitate which contains mainly amylose. In this system, amylose associate together to form very compact double helices that further associate to form the precipitation [110], [119]. Amylopectin and highly branched polysaccharides take part in the precipitation as well in less extent since the amylose forms complex structure with these molecules [16]. The relevant information is that these

highly branched molecules will precipitate in such a way that they will try to settle closer to the upper solution layer which means the presence of more branched molecule with the decrease in distance to the upper solution layer. As described before in section 5.1, the
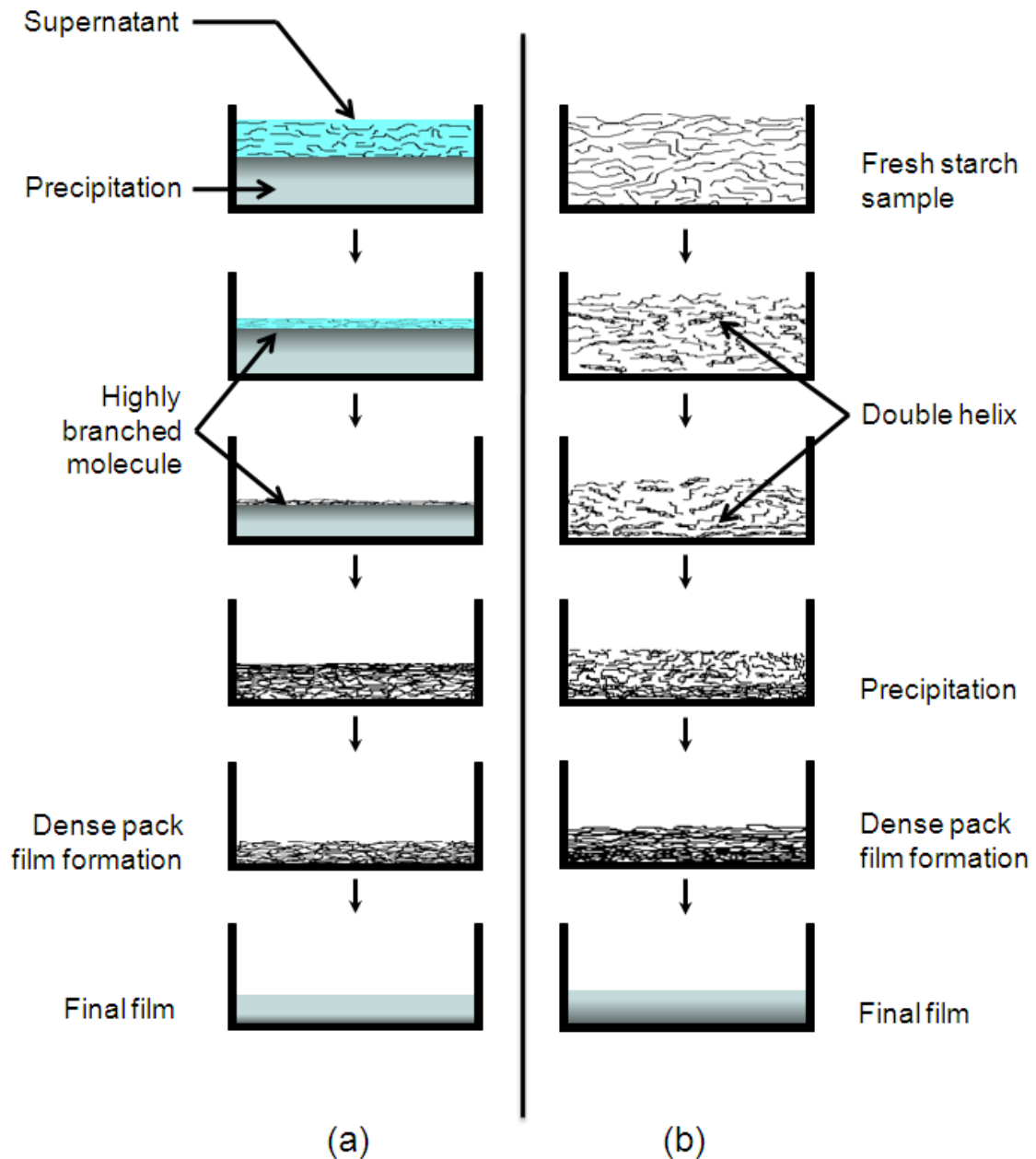

Figure 5.13: *Illustration of the starch system at different drying times.* **(a)** *Sample c containing 1% starch in H_2O (w/v) and* **(b)** *Sample d containing 5% starch in H_2O (w/v). The evolution time increases from top to bottom.*

highly branched molecules are readily affected by water. Consequently, these molecules will have affinity to water which might explain this tendency. Moreover, the amylopectin-rich non-volatile solute of the upper part of the dilute sample will accumulate in the interface when the solvent from the upper part is evaporated. Accordingly, a gradual

increase in the amount of highly branched molecule near to the air-sample interface will be established. The decrease in T_2 value towards the air-sample interface (figure 5.5 (a)) can be explained by the combination of these two occurrences. The starch sample prepared from 5% starch in water is a gel from the beginning of film formation which does not show this tendency.

At a later stage, a decrease in T_2 value at the bottom part of the sample can be observed, especially in 5% starch containing sample. Starch gel consists of double helical crystallite [16]. The crosslinked gel system is not stable due to continuous evaporation of water. Consequently, it is most likely that the double helix structure precipitate when the water concentration is reduced in the system presumable that the water takes part in the structure making hydrogen bond. This process will reduce the mobility of the bottom part of the sample which is possible to follow from the relaxation study. In this way, the interplay of water evaporation and polymer migration result, for the conditions studied in this work, in a dynamic heterogeneity of the polymer molecules across the film thickness, which develops gradually after the average water concentration drops below a critical value. The XRD data shows that the dense triple-helix structure that is preferably generated at the bottom of the sample during the evaporation makes a significant difference in the structure of the final film.

5.7. Conclusions

A number of studies were conducted to follow the evaporation of the solvent from two different starch samples containing 1% and 5% of starch in water (w/v) during the process of film formation. In both systems, glycerol was used as a plasticizer. These studies enable one to understand the starch-H_2O system at a molecular level. Using a micro camera, evaporation of the solvent from these starch systems was observed optically revealing that at the macroscopic level, the evaporation tendency of these two systems is different. While 1% starch containing sample forms a precipitation at the beginning, 5% starch containing sample is a gel. With evaporation, the thickness of the upper solution part of 1% starch containing sample reduced due to solvent evaporation and the lower precipitation layer became dense packed.

By a time-dependent NMR 1D-microimaging (profile) measurement of the samples it was found that the transverse relaxation times (T_2) represent a suitable measure for indicating the residual mobility of the sample, whereas the signal intensity determined along the profile requires taking the evolution of T_1 into account. The 1% starch containing sample showed a gradual decrease in the mobility of the polymer molecules near to the

air-sample interface at the beginning of the experiment period which was totally absent in the sample containing 5% starch in water. When both starch samples were approaching the final drying stage, the T_2 values of the system near the substrate decreased more compared with that of the vicinity of the air-sample interface. Subsequent analysis of the completely dried film by X-ray diffractometry revealed that the amorphous region at the upper surface is indeed considerably higher than that at the lower surface. These observations are similar to earlier finding obtained for gelatin solutions, where network formation and precipitation resulted in an increased crystallinity at the bottom surface (chapter 4).

In this chapter, the progress of molecular mobility of starch suspension until the final stages of film drying has been investigated with spatial resolution for the first time by using NMR relaxometry, providing insight into the development of resolved polymer concentration. The main conclusion from the complete set of experiments is that the starch film is drying in a stratified fashion.

Chapter 6

Structural and dynamical heterogeneities of PVOH film during its formation

The opposite of a correct statement is a false statement.
But the opposite of a profound truth may well be another profound truth.

Niels Bohr

6.1. Introduction

Water is used as a common solvent for the production of semi-crystalline poly(vinyl alcohol) (PVOH) film. Above the glass transition temperature ($T_g \approx 85^\circ C$) fully hydrolyzed PVOH is completely soluble in water [120]. The interaction between the PVOH and water molecules plays an important role in polymer chain dynamics in the solution [121]. With continuous evaporation of water this dynamic changes in time and the final film is obtained from a cast solution. Films from PVOH in aqueous solution have been a largely studied system, however, most of them refer to crosslinked hydrogels [120], [122]-[124]. The influence of the formation process in solution-based PVOH films shows different characteristics; contrary to hydrogels, PVOH film formation by solvent evaporation does not involve any cross-linking (gelation). However, a number of complex interactions are still present making difficult any quantitative description accounting for the processes that drive the cast solution to the final film. A number of references [11], [18]-[21] have been devoted to study of the drying of the PVOH solution. There, a "skin" formation process has been reported which consists of a glassy layer formation on top of the evaporating solution. This process is related to the shifting of the glass transition temperature (T_g) due to the change in the solvent concentration. As the PVOH film is semicrystalline in nature,

the removal of solvent during the film formation process will drive both the crystallization and the amorphous phase (glass) formation process. In particular the glass transition temperature of the PVOH-water mixture will increase. As a consequence, a glassy layer may develop in the air-sample interface as the solvent removal rate is faster in this part of the sample, compared with the bulk solution system. On the other hand, the development of a crystalline skin is reported in reference [22] on the basis of the change in evaporation rate during the film formation. In this reference magnetic resonance imaging (MRI) studies of PVOH cast from aqueous solution as a function of time show nonuniform water distribution at certain drying conditions, coupled with a crystalline layer at the top surface of the solution. However, detailed microscopic experimental studies explaining these observations as well as the structural characterization of the final film addressing these phenomena are scarce.

In this chapter, the presence of gradual heterogeneities in dynamics during film formation of the PVOH in an aqueous solution is experimentally demonstrated using single-sided NMR technique. X-ray diffraction (XRD) technique is used to study the film which is capable of providing information on structure of the final state of the PVOH film at a molecular level. The NMR studies presented here reveal a progressive process leading to a hardening of the top regions of the film assessed by the relaxation times T_2 and T_1 gradually growing towards the bottom part of the sample. Beside the single-sided NMR scanner, a Minispec and a field cycling relaxometer are used to study the T_2 and T_1, respectively to obtain additional information. The heterogeneity identified by the NMR study is confirmed by the XRD study of the film. In this way, dynamic and structural studies performed with NMR and XRD, respectively, provide evidence that heterogeneities in the film formation process and in the final film are present.

6.2. Samples

Table 6.1 shows the characteristics of the samples used in this work. The film formation of PVOH of three different molecular weights, MW=27000 (indicated as 27K), 61000 (61K) and 125000 (125K) was investigated in order to observe the molecular weight dependency. While most of the experiments were carried out with the sample of 61K (sample *a, c, e, f, g, h* and *i*), comparative measurements were repeated under similar experimental conditions for 27K (sample *b*) and 125K (sample *d*), respectively. Deuterated water (D_2O) was used as a solvent (sample *a, e, g* and *i*) in order to selectively follow the dynamics of the backbone of the PVOH molecules. The results obtained using H_2O as a solvent were compared with those obtained using D_2O. The initial concentration

of PVOH in the solution was set to 25% (w/v) for all the samples. The same protocol was used for the preparation of all the samples to be diluted either with H_2O or D_2O. Note that when PVOH is used as a hydrogel, the gel is induced only after several cycles of a freezing-thawing process [125], [126]. However, no gel formation was observed after several hours of preparation in the present work.

Table 6.1: *Different PVOH samples prepared using H_2O or D_2O as a solvent. The initial concentration of PVOH in solution was 25% (w/v).*

Sample	Molecular weight of PVOH	Solvent	Study	Thickness of the final film (µm)
a	61K	D_2O	Profiling at 11.7 MHz (^{1}H) and XRD	275 ± 10
b	27K	H_2O	Profiling at 11.7 MHz (^{1}H) and XRD	380 ± 25
c	61K	H_2O	Profiling at 11.7 MHz (^{1}H) and XRD	340 ± 12
d	125K	H_2O	Profiling at 11.7 MHz (^{1}H) and XRD	268 ± 15
e	61K	D_2O	T_1 at 11.7 MHz (^{1}H)	---
f	61K	H_2O	Diffusion at 11.7 MHz (^{1}H)	---
g	61K	D_2O	Diffusion at 11.7 MHz (^{1}H)	---
h	61K	H_2O	T_1 and T_2 at 40 MHz (1H)	---
i	61K	D_2O	T_1 and T_2 at 40 MHz (1H)	---

For the diffusion measurements, sample *f* (25% (w/v) PVOH in H_2O) and sample *g* (25% (w/v) PVOH in D_2O) were prepared and the stimulated echo sequence in combination with the static magnetic field gradient of the sensor was used. The measurements were performed right after the casting, sealing the container to avoid evaporation. For this measurement an encoding time τ = 0.0055 to 1.9 ms, diffusion time Δ = 2 ms, repetition time of 3 s and 5 s (for sample *f* and *g*, respectively) were used. All experiments were performed at room temperature.

6.3. Film formation study

6.3.1. Real time film formation study using single-sided NMR scanner

Profiling of the samples

As stated in the experimental chapter, the sample was placed on top of the scanning device and vertical profiles were obtained (figure 6.1) by moving the scanner from top to bottom at a step size of 100 μm at the beginning and 50 μm at a later stage with a resolution of 50 μm in both cases. The time scale shown in this figure is the time after sample casting.
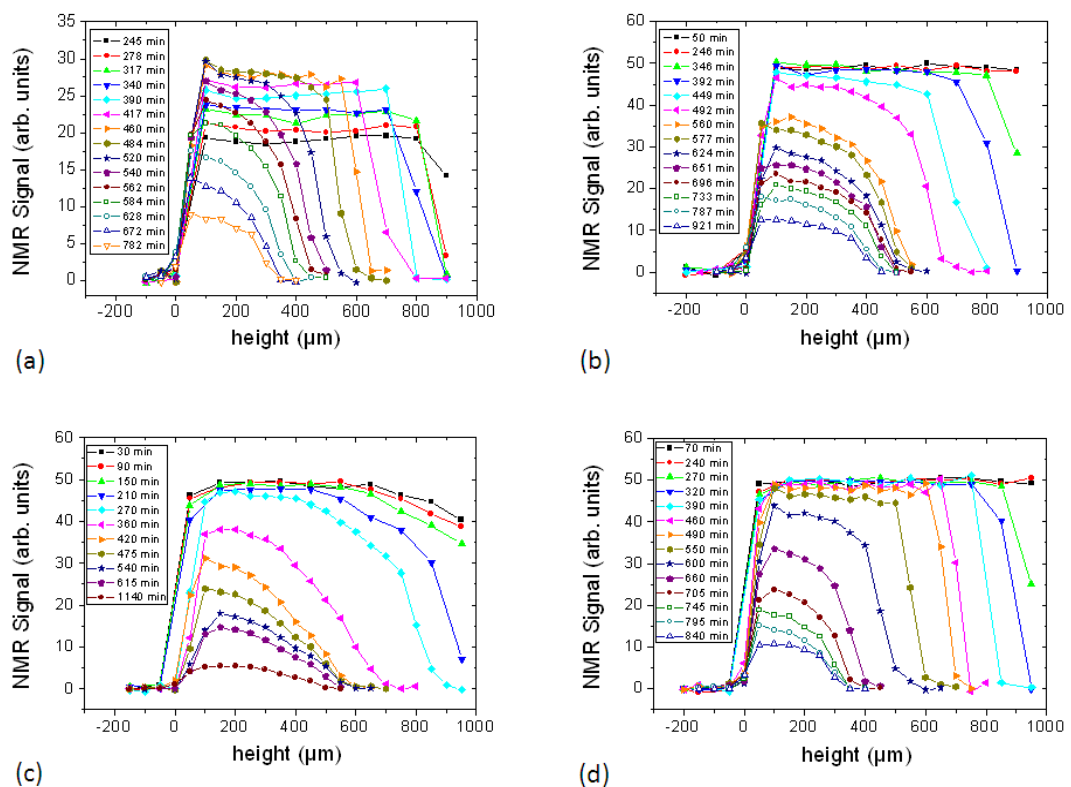

Figure 6.1: *NMR profiles of the 25% PVOH in water (w/v) solution system at different drying times:* **(a)** *sample a containing PVOH (MW= 61K) in D_2O* **(b)** *sample b containing PVOH (MW= 27K) in H_2O* **(c)** *sample c containing PVOH (MW= 61K) in H_2O and* **(d)** *sample d containing PVOH (MW= 125K) in H_2O.*

The NMR profiles for sample *a, b, c* and *d* are presented in figure 6.1 (a), (b), (c) and (d), respectively, as a function of height at different time intervals while the system is evolving under the solvent evaporation. Between two successive profiles, T_1 was

measured (see "determination of T_1 at different heights" section) for the samples prepared using H_2O as a solvent (except sample *a*). The right edge of the profiles corresponds to the air-sample interface whereas 0 μm at the left hand side shows the substrate-sample interface. All the samples possess an initial height of more than 1000 μm and the air-sample interface is becoming observable due to progressive shrinkage after 245 min, 346 min, 210 min and 270 min of evaporation time for sample *a*, *b*, *c* and *d*, respectively. Note that the apparent shift of the substrate-sample interface by approximately 50 μm is an averaging effect and a consequence of the change of step size of the scanner which is reduced from 100 μm to 50 μm.

For sample *a*, the signal intensities show a gradual increase according to the increase of the polymer concentration as a consequence of water evaporation. It is seen that the maximum profile intensity shown by other three samples are the same (within experimental error) which means that the molecular weight of the PVOH samples does, at first sight, not have an influence on the signal intensity. The signal of the profiles is a consequence of the number density of protons in PVOH and water. Due to the settings of the NMR experiment there is no T_1 weighting, but a T_2 influence cannot be completely excluded. Its influence is negligible in the profiles (see following section); the profile is therefore only an indicator for the film thickness but not for the distribution of polymer within the film.

The profiles describe macroscopic features of the film formation process associated with the evaporation of the solvent. The height of these profiles decreases during the later part of the experiments due to the evaporation of solvent causing shrinkage of the sample and the reduction of T_2 values. The edge of the profile curves at the substrate-sample interface did not change in time, while the signal intensity in all the profiles exhibits a sharp decay on the air-sample interface at earlier times during film formation.

Determination of sample shrinking rate

In figure 6.2 the decrease in the sample height as a function of evolving time is shown. The sample height has been calculated as the width of the profiles is defined by the values of 5% of the maximum intensity where the signal can still be distinguished reliably from the noise level. Based on this assumption, the rate of evaporation $\dot{E}$, defined as the slope of the fitted lines, was calculated for each sample. It can be seen that the first stage of evaporation have similar rates for sample *a*, *b* and *c*. For sample *d* this value is slightly smaller, which means that a very high molecular weight of PVOH sample may

affect the evaporation process. All of these curves demonstrate that the rate of evaporation has two different regimes. They are expressed as $\dot{E}_1$ (for the first part) and $\dot{E}_2$ (for the second part), respectively, with a crossover at $\tau_{CR} \approx$ 580 min, 560 min, 420 min and 700 min of drying time for sample *a*, *b*, *c* and *d*, respectively. Note that the rates decrease almost one order of magnitude for all the samples. The relative humidity and temperature of the laboratory were not controlled but tend to be 40 ± 5% and (21 ± 2) °C, respectively, which may influence the average drying time.
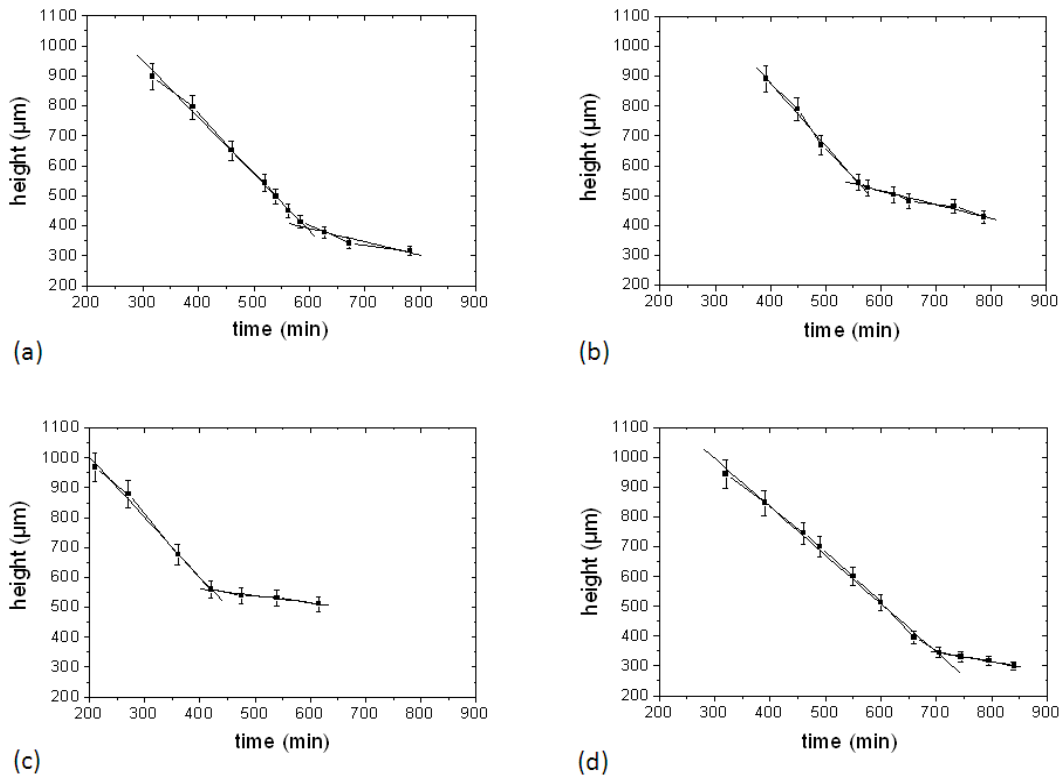

Figure 6.2: *Film thickness estimated from the profile widths in figure 6.1, as a function of drying time. Linear fits to the experimental data are shown.* **(a)** *sample a containing PVOH (MW= 61K) in D₂O (* $\dot{E}_1 = 3.0 \times 10^{-8}$ *m/sec and* $\dot{E}_2 = 0.7 \times 10^{-8}$ *m/sec)* **(b)** *sample b containing PVOH (MW= 27K) in H₂O (* $\dot{E}_1 = 3.5 \times 10^{-8}$ *m/sec and* $\dot{E}_2 = 0.8 \times 10^{-8}$ *m/sec)* **(c)** *sample c containing PVOH (MW= 61K) in H₂O (* $\dot{E}_1 = 3.4 \times 10^{-8}$ *m/sec and* $\dot{E}_2 = 0.4 \times 10^{-8}$ *m/sec) and* **(d)** *sample d containing PVOH (MW= 125K) in H₂O (* $\dot{E}_1 = 2.7 \times 10^{-8}$ *m/sec and* $\dot{E}_2 = 0.5 \times 10^{-8}$ *m/sec).*

Similar observation is described in reference [22] where the two regimes are attributed to the formation of a "skin layer" at the air-sample interface. It is stated that this skin, having insufficient mobile ^{1}H to be visualized during profiling, consists of a relatively high crystalline fraction which makes it particularly impermeable. Consequently, evaporation rate becomes slower as it is reflected from the two evaporation rates. The thickness of any eventual "skin layer" is in any case much smaller than the resolution of the scanner (30 μm).

The different evaporation regimes correlate with the change in the shape of the profiles in their air-sample interface. The sharper decay is associated with the faster evaporation rate. This behavior can be interpreted as a dynamical change produced after the average water concentration decreases below a certain value where there is almost no free water anymore, but still the polymer retain high mobility.
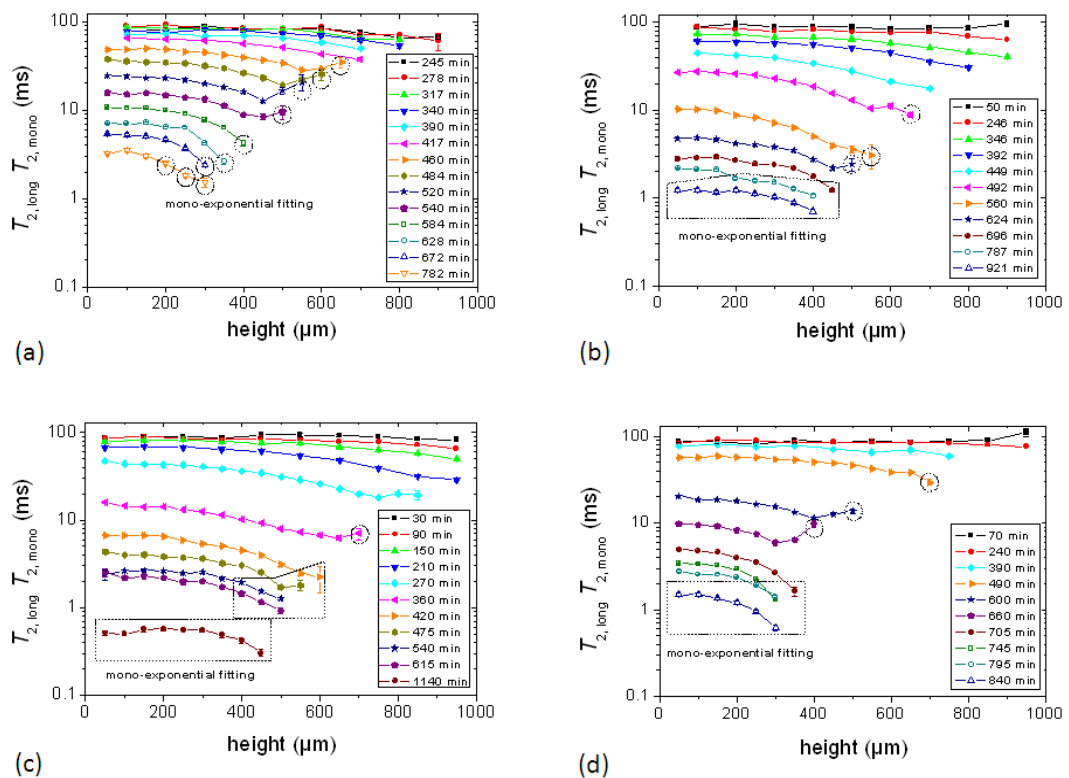
Determination of T_2 at different heights

Figure 6.3: T_2 *relaxation times of the slowly decaying components at different heights of* **(a)** *sample a containing PVOH (MW= 61K) in D_2O* **(b)** *sample b containing PVOH (MW= 27K) in H_2O* **(c)** *sample c containing PVOH (MW= 61K) in H_2O and* **(d)** *sample d containing PVOH (MW= 125K) in H_2O. The layer positions correspond to coordinates introduced in figure 6.1. At the later stage of drying, the echo decays were fitted mono-exponentially which is indicated by the circles and boxes.*

Each point in the profile of figure 6.1 is obtained from an individual CPMG echo train which means that at a given time, the proton spin-spin relaxation time constant (T_2) can be obtained all over the sample height from the analysis of corresponding echo decays (figure 3.8 (b) and (c)). It is found that at the earlier evaporation times, the echo decay curves can be fitted with a bi-exponential function (Equation 3.2). The short T_2 decay is expected to correspond to the relaxation of the protons of the PVOH molecule that are not able to exchange (non-labile protons). For sample *a*, the longer relaxation

constant is related with the protons that are able to exchange with the hydrogen atoms of the D_2O molecules in solution. For the other three samples, this decay corresponds to the water protons as well as to the -OH protons of PVOH that exchange with the solvent. The long and short T_2 components as a function of sample height are shown in figure 6.3 and 6.4, respectively, from the beginning to a later stage of film formation process which is indicated by the evaporation time.
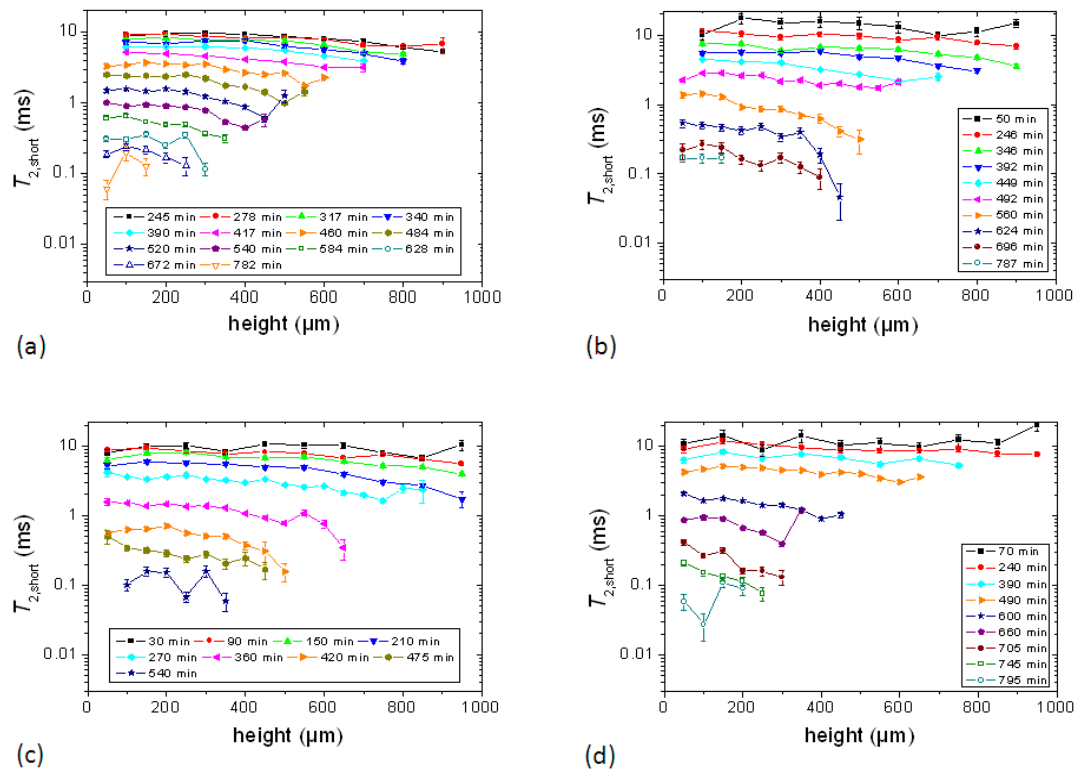

Figure 6.4: T_2 relaxation times of the faster decaying components at different heights of **(a)** sample a containing PVOH (MW= 61K) in D_2O **(b)** sample b containing PVOH (MW= 27K) in H_2O **(c)** sample c containing PVOH (MW= 61K) in H_2O and **(d)** sample d containing PVOH (MW= 125K) in H_2O. The layer positions correspond to coordinates introduced in figure 6.1.

Note that the T_2 obtained in the single-sided NMR is the combination of transverse relaxation and magnetic field inhomogeneity. Accordingly, T_2 relaxation time data described in this section will be considered as the effective T_2 time (see section 3.3).

For sample *b*, *c* and *d*, it is found that a $T_{2,long}$ of around 90 ms at different heights can be seen in the first hour of the drying process. For sample *a*, this T_2 value is slightly bigger in the first hour as can be estimated from the figure 6.3 (a) (around 85 ms after 245 min). For all samples, $T_{2,long}$ values decrease with time until the end of measurement period due to both the process of film formation and solvent evaporation. From the

relaxation behavior of the bottom part of the sample, it is also evident that the $T_{2,long}$ values decrease around two orders of magnitude (~90 ms to ~2 ms) during the drying period. Figure 6.4 shows that $T_{2,short}$ is around 10 ms after first few hours of casting for each sample which is decreased to around 0.1 ms until the short components are not anymore detectable. Therefore, similar to the long components, $T_{2,short}$ decreases nearly two orders of magnitude and then become undetectable by the experimental setup.

The fundamental observation in these figures is that the T_2 relaxation times change at different layers for each measurement. From a certain time of evaporation onwards (460, 492, 360 and 490 min for sample *a*, *b*, *c* and *d*, respectively), the echo decay of the air-sample interface layer in all the samples, could only be fitted with a mono-exponential function (Equation 3.1) to obtain the corresponding T_2 value (see figure 6.3). For further evaporation times this feature extends on inner layers and at the end on the complete sample. It can be seen that after 921, 1140 and 840 min for sample *b*, *c*, and *d*, respectively, there is no second component all through the sample height as shown in the last profile experiment in each sample. Note that the pulse separation used in these experiments is 87.5 μs which means the first echo is generated after this time. The solid like component, which decays within 100 μs [87], will be difficult to observe. This is the reason why only one component is observed at the later stage of drying which indicates the formation of a solid-like structure at the top surface of the sample. In figure 6.4 it is also observed that T_2 values of the short components gradually decreases as the height of the sample increases at later stage of evaporation time i.e. both long and short components behave qualitatively in the same way. The values of T_2 do not show any dependence on height at the beginning of the experiment indicating that at the beginning of the film formation process, the solution is uniform. Note that for sample *a*, which is used to follow the relaxation behaviour of the polymer chain, same type of T_2 dependency as a function of sample height is observed. Furthermore, the short T_2 values of this sample are similar to the shorter T_2 of sample *b*, *c* and *d*. The short T_2 values of the samples *a*, *b*, *c* and *d* at the respective evolution time show very weak dependence on height inside the experimental errors. At later times, the short components are not anymore detected. The difference in gradual change of T_2 all along the layers in different experiments due to the drying effects are bigger than any change in T_2 that could happen in the time taken for a single profile. The relative difference between the maximum and minimum T_2 (calculated from the bottom and the top surface of the sample, respectively) comparing to T_2 of the
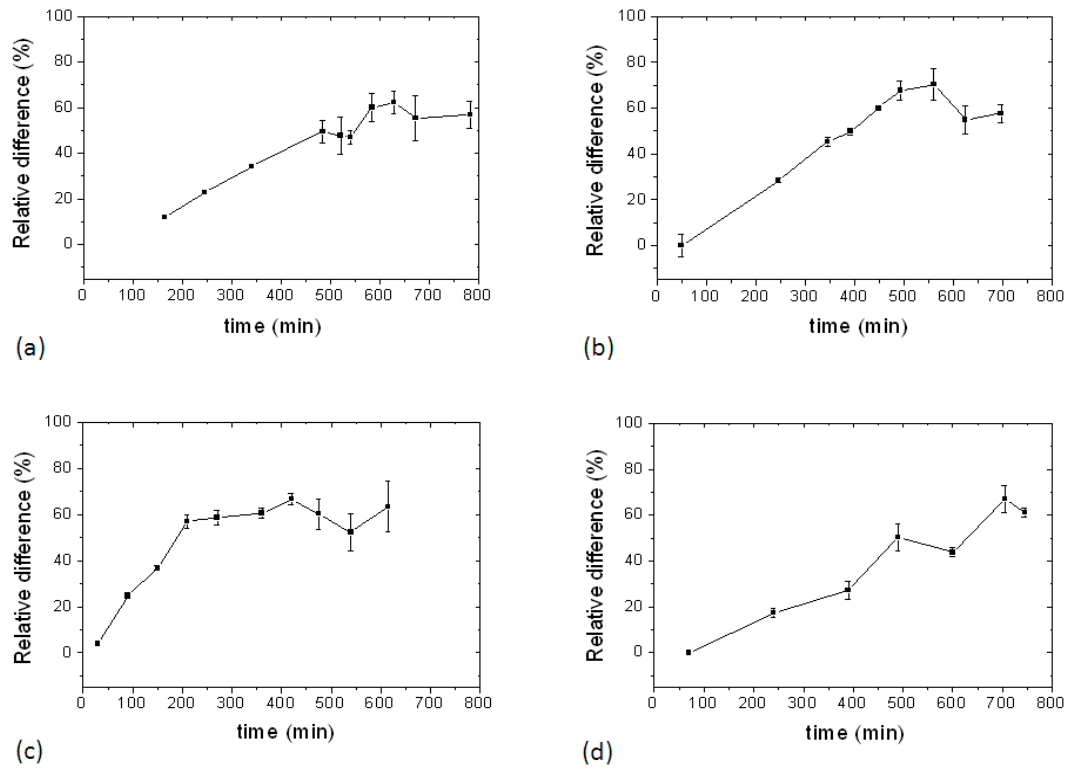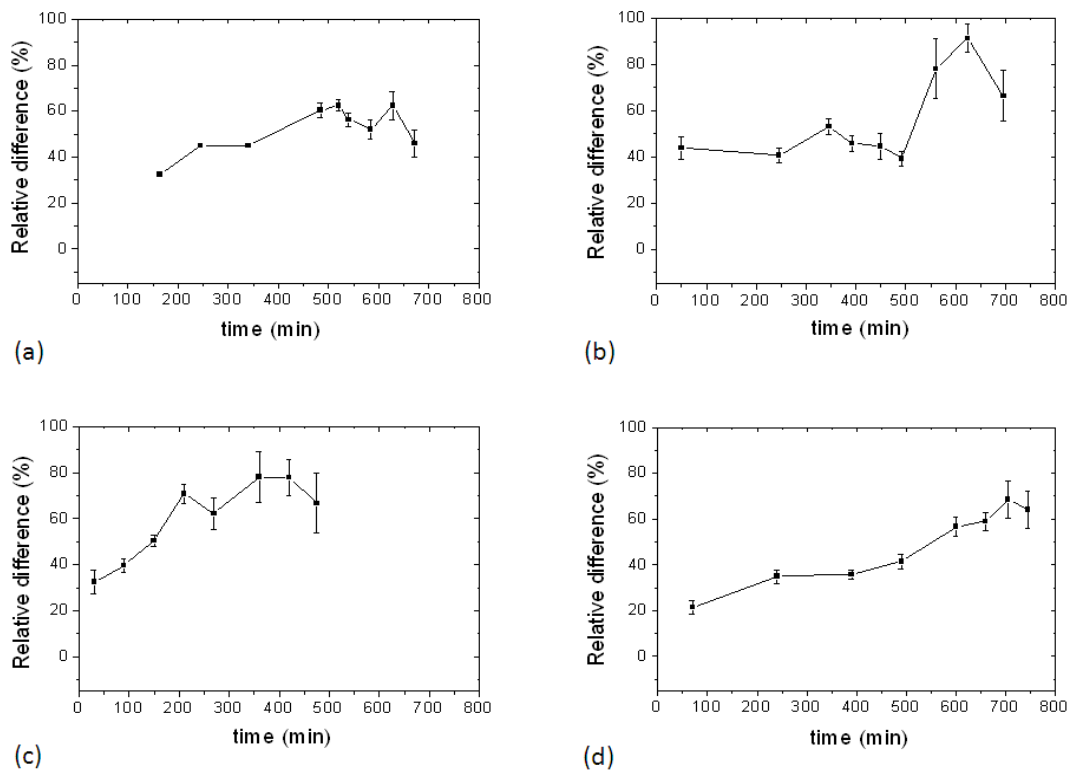
Figure 6.5: *Relative difference between the maximum and minimum T_2 of the slowly decaying components calculated respectively from the bottom and top parts of a single profile in figure 6.3 at different drying times. The labels* **(a)**, **(b)**, **(c)** *and* **(d)** *in the figures correspond to the sample a, b, c and d, respectively.*

Figure 6.6: *Relative difference between the maximum and minimum T_2 of the faster decaying components calculated respectively from the bottom and top parts of a single profile in figure 6.4 at different drying times. The labels* **(a)**, **(b)**, **(c)** *and* **(d)** *in the figures correspond to the sample a, b, c and d, respectively.*

bottom part is plotted in figure 6.5 and 6.6 for the long and short components, respectively. This difference increased to more than 60% and then stabilized inside the experimental error.
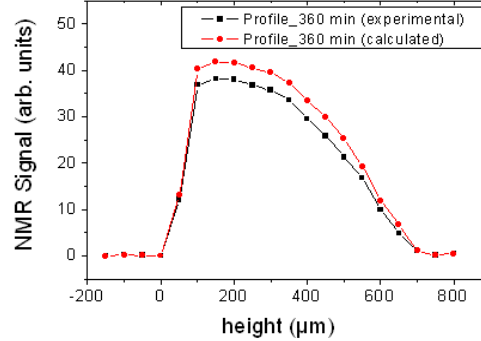

Figure 6.7: *Effect of T_2 on the profile intensity (see text). The experimental profile is taken from sample c containing PVOH (MW= 61K) in H_2O at 360 min.*

From the T_2 values obtained in the figure 6.3 and 6.4, a possible effect of T_2 on the profiles (figure 6.1) can be estimated. Taking the profile of the sample *c* at 360 min as an example, the estimation is shown in figure 6.7. The experimental intensities of the profile and the intensities as it would be affected by the T_2 process can be modeled by the equation,

$$I(layer, t_{echo}) = \frac{I_0}{4} \sum_{i=2}^{5} \{A_{short} \exp(-i \times t_{echo} / T_{2short}) + A_{long} \exp(-i \times t_{echo} / T_{2long})\} ,\quad (6.1)$$

Here, i corresponds to the echo number. As explained before, the signal is the sum of the area of the 2nd to 5th echoes. The echo-time (t_{echo}) is 87.5 µs and I_0 is the maximum intensity at time t=0. From Equation 6.1, the experimental intensities of the profile and the T_2-compensated intensities can be determined using the following correction,

$$I_{corrected}(layer, t) = 4 \times I_{exp}(layer, t) / \sum_{i=2}^{5} \{A_{short} \exp(-i \times t_{echo} / T_{2short}) + A_{long} \exp(-i \times t_{echo} / T_{2long})\}$$
$$(6.2)$$

Figure 6.7 shows that if the relaxation effect on the intensities is compensated, the overall shape of the profile is almost the same. Consequently, the profile is not much affected by the T_2 relaxation process occurring during the acquisition of the first 5 points in the CPMG decay.

Relative weight fraction of T_2 components at different heights

The relative weight (see Equation 3.2) of the two contributions, A_{short} and A_{long}, can be estimated based on the initial polymer concentration and the state of evaporation as is obtained from the remaining film thickness, assuming approximately constant density throughout the experiment. The relative amounts of the fast decaying components, calculated as $A_{short}/(A_{short} + A_{long})$ are shown in figure 6.8.
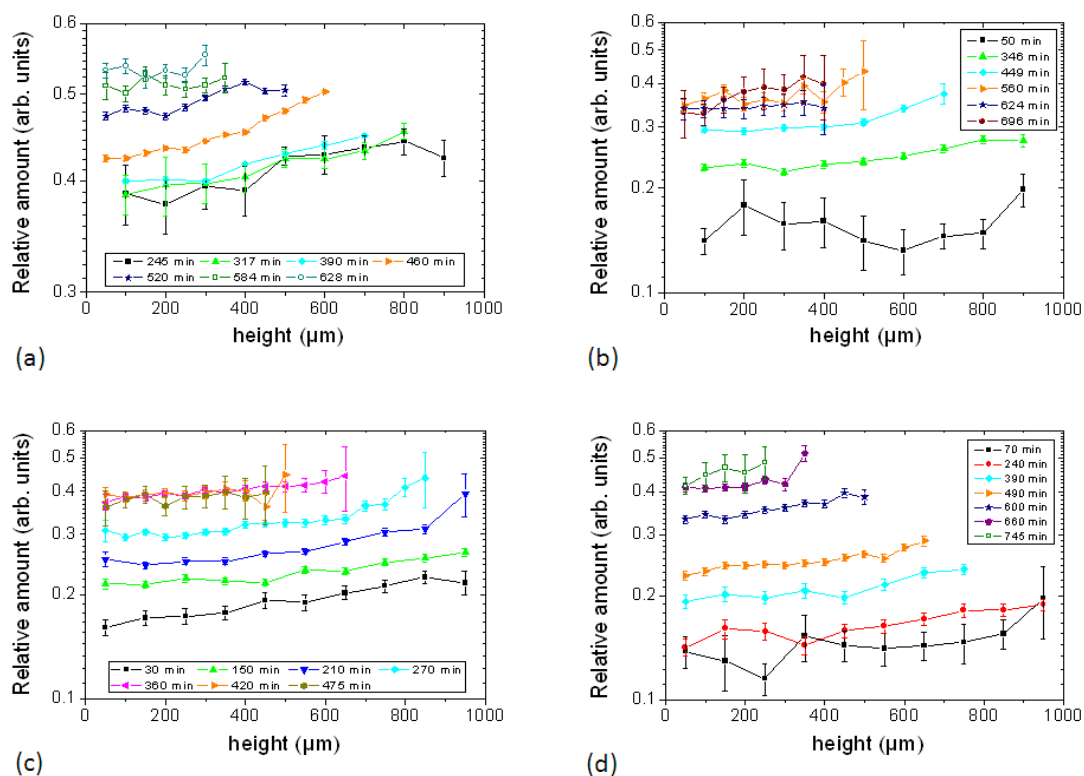

Figure 6.8: *Change in relative amount of the fast decaying components with time in* **(a)** *sample a containing PVOH (MW= 61K) in D_2O* **(b)** *sample b containing PVOH (MW= 27K) in H_2O* **(c)** *sample c containing PVOH (MW= 61K) in H_2O and* **(d)** *sample d containing PVOH (MW= 125K) in H_2O. Each symbol type and layer positions correspond to a complete profile and coordinates, respectively as introduced in figure 6.1.*

The relative difference between the maximum and minimum values of the relative component, A_{short} are shown in figure 6.9 as a function of the drying time. The two components of T_2 allow certain discrimination of the dynamics of the polymer itself and its solution. As discussed before, the component with a shorter relaxation constant may be assigned to the non-labile protons of the polymer backbone. This fast decaying component increases with time of film formation all along the system (figure 6.8). As the evaporation of the solvent continues, the concentration of the solute increases as well as the contribution of the polymer main chains in the NMR signal which explains this trend.

From the figure it is clear that the relative amount in each of the samples grows slightly towards the top part. From figure 6.9 one can infer that the presence of the polymer chains in the top surface of each of the samples is around 40% higher than the bottom part of the sample after 1 hour of evaporation. This relative difference decreases with time of evaporation and a difference of around 20% (apart from sample *a*) between the top and bottom layers is observed at the crossover of the two evaporation regimes (figure 6.2).
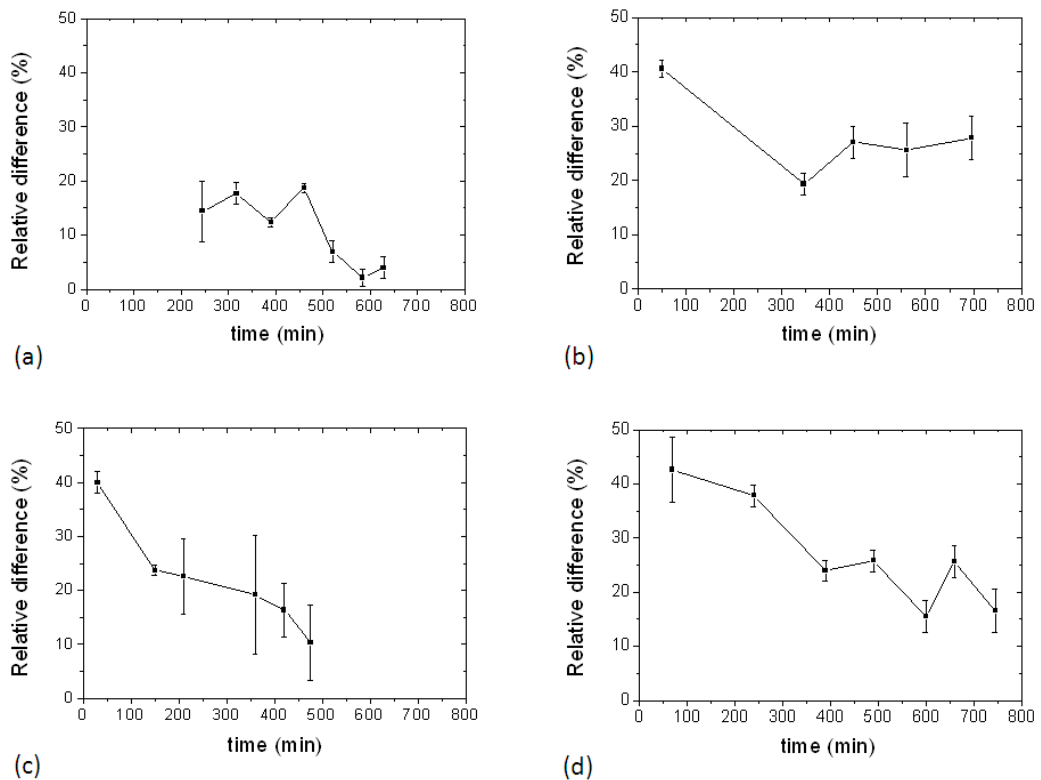

Figure 6.9: *Relative difference between the maximum and minimum relative amount of the faster decaying components of T_2 calculated respectively from the bottom and top layers of a single profile in figure 6.8 at different drying times. The labels* **(a)**, **(b)**, **(c)** *and* **(d)** *in the figures correspond to the sample a containing PVOH (MW= 61K) in D_2O, b containing PVOH (MW= 27K) in H_2O, c containing PVOH (MW= 61K) in H_2O and d containing PVOH (MW= 125K) in H_2O, respectively.*

Determination of T_1 at different heights

As stated in section 6.3.1 (profiling of the samples), T_1 and T_2 measurements of the same sample are performed alternatingly as a function of height with the exception of sample *a* that contains PVOH in D_2O. A mono-exponential function was fitted to all the magnetization recovery curves in these experiments to obtain corresponding spin–lattice relaxation time (T_1) values. The results of T_1 measurements of sample *b*, *c*, and *d* are shown in figure 6.10 as a function of sample height at different drying times.
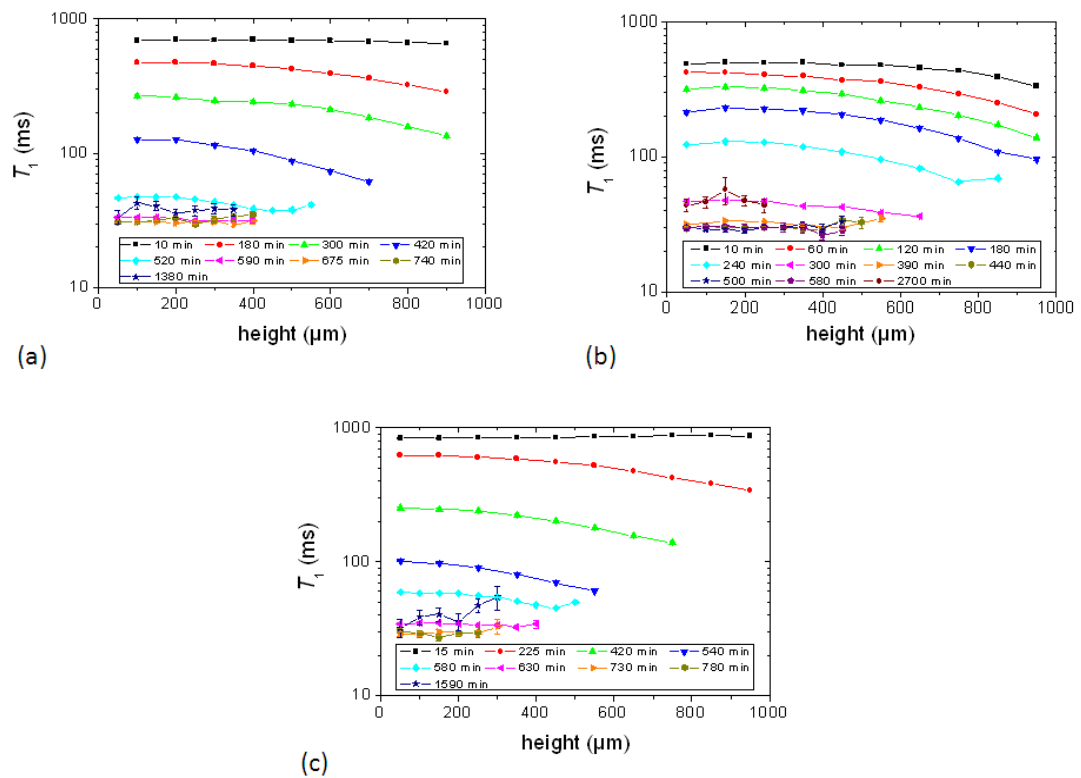
(a)

(b)

(c)

Figure 6.10: *Evolution of T_1 with drying time in* **(a)** *sample b containing PVOH (MW= 27K) in H_2O* **(b)** *sample c containing PVOH (MW= 61K) in H_2O and* **(c)** *sample d containing PVOH (MW= 125K) in H_2O. The layer positions correspond to coordinates introduced in figure 6.1.*
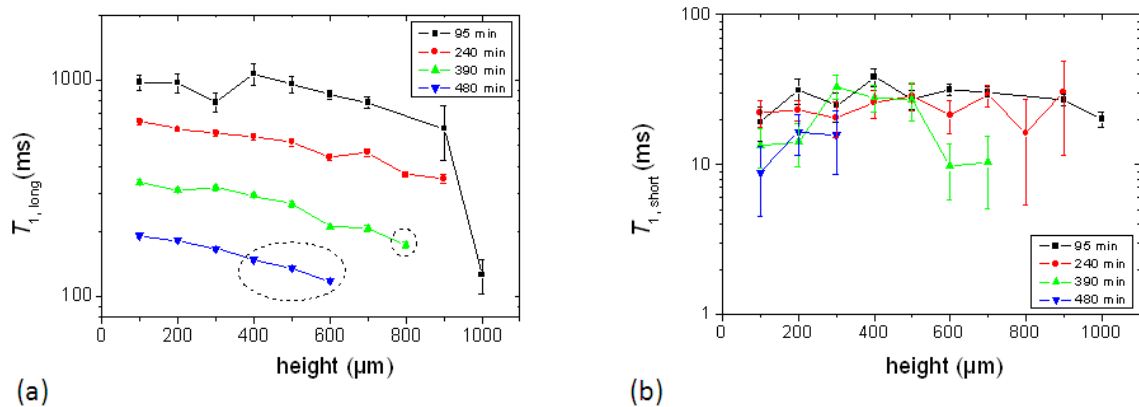

(a)

(b)

Figure 6.11: *Evolution of T_1 with drying time in sample e containing PVOH (MW= 61K) in D_2O:* **(a)** *T_1 of the long components and* **(b)** *T_1 of the short components. At the later stage of drying, the magnetization recovery were fitted mono-exponentially which is indicated by the circles.*

For sample *a*, the required number of scans was higher to obtain an acceptable signal to noise ratio comparing to that of H_2O containing samples during the CPMG experiments. As a result, T_1 and T_2 measurements of this sample could not be carried out alternatingly. A separate sample named *e* was prepared using D_2O and magnetization

recovery data were obtained using same parameters and conditions. In this study, two components were found and a bi-exponential function was fitted accordingly. The results for sample e are shown in figure 6.11.

The T_1 values of all the samples show common features. For instance, T_1 values decrease as a function of time as a result of the solvent evaporation. From figure 6.10, it can be seen that starting from the three different T_1 values, 700 ms, 500 ms and 900 ms for the sample b, c and d, respectively, all the samples show a minimum value of around 30 ms after evolution. In the general case, the NMR relaxation rate of polymers in solution is proportional to the so-called segmental reorientation time [127], [128]

$$\frac{1}{T_1} \propto \tau_s \approx \frac{b^2\, a_H\, \eta}{k_B T}\,,\tag{6.3}$$

where b is the Kuhn segment length, a_H is the hydrodynamic radius of the segments and η is the viscosity of the medium surrounding the segment. T is the absolute temperature and k_B is the Boltzmann constant. As the evaporation takes place, the mobility of the polymer chains decreases due to the increase in the viscosity of the solution and as a consequence, the NMR relaxation process is affected. In the case of pure water, T_1 and T_2 have an inverse dependence with the viscosity as well [32], but this dependence not necessarily holds for the case of water in a polymer-water solution.

After 1380 min, 2700 min and 1590 min of drying time, T_1 values of the sample b, c and d, respectively, show a relative increase. It is expected that the crystalline component in a solid polymer will have longer T_1 relaxation time than the corresponding amorphous component at the same temperature and magnetic field [32]. The gradual increase of T_1 towards the top of the solution at 1590 min in sample d is compatible with the presence of more crystalline component in the top of the film. Before the minimum T_1 is reached, the bottom parts of all the samples show longer T_1 than the corresponding upper part following similar spatial patterns than T_2 along the height of the film. The different values of T_1 along the sample height provide additional evidence that the drying of the PVOH film is inhomogeneous. This effect is less pronounced in the short component of sample e due to larger experimental error (figure 6.11 (b)). The weight fraction of the two T_2 components of this sample does not show any particular trend.

Diffusion Study

The steady strong gradient of the single-sided NMR scanner was used to perform the diffusion experiments. Figure 6.12 shows the echo decays of two freshly prepared sample f and g where H_2O and D_2O are used as the solvent, respectively. The signal of the residual ^1H in the solvent from the sample g is strongly suppressed by a repetition time much shorter than the corresponding T_1. In this figure, two components can clearly be distinguished. The diffusion attenuation for the two components in the slow-limit exchange can be written as [44]

$$A_{diff}\left(\tau\right) = A_{short} \exp\left\{-KD_{short} - \left(\frac{2\tau}{T_{2short}} + \frac{\Delta}{T_{1short}}\right)\right\} + A_{long} \exp\left\{-KD_{long} - \left(\frac{2\tau}{T_{2long}} + \frac{\Delta}{T_{1long}}\right)\right\}, \quad (6.4)$$

where $K = \left(\gamma G\tau\right)^2 \left(\Delta + \frac{2\tau}{3}\right)$. γ, G, τ and Δ represent gyromagnetic ratio of protons, gradient strength, encoding time and diffusion time, respectively. Note that for sample f and g, both conditions, $\tau \ll T_2$ and $\Delta \ll T_1$ are satisfied. As a result these two relaxation times will not affect the diffusion measurement.
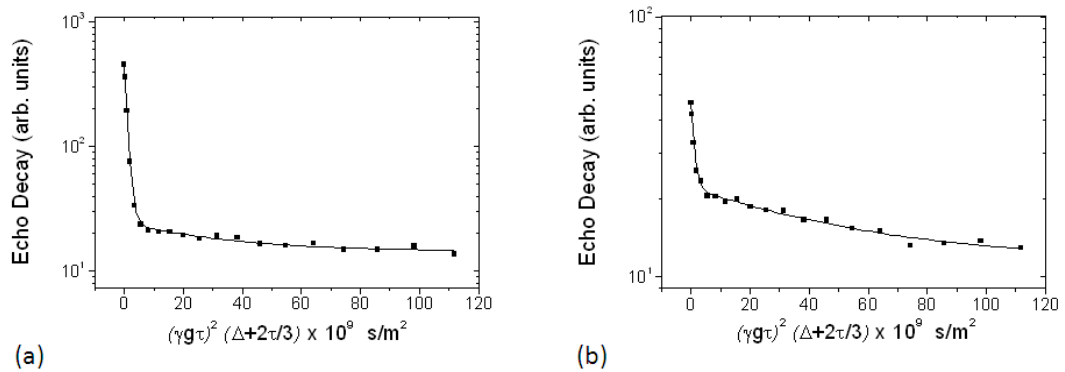

(a)   (b)

Figure 6.12: *Stimulated echo decay curves of (a) sample f containing PVOH (MW= 61K) in H_2O and (b) sample g containing PVOH (MW= 61K) in D_2O measured in the single-sided NMR scanner right after the sample preparation. The solid lines are bi-exponential fittings to the experimental data.*

The values of the slow diffusion component corresponding to the polymer are $(3.2 \pm 0.1) \times 10^{-11}$ m^2/s and $(1.8 \pm 0.4) \times 10^{-11}$ m^2/s for the sample f and g, respectively (Figure 6.12). On the other hand, the fast diffusion coefficient reflects the exchange of protons between the backbone and the solvent. Sample f has a fast diffusion coefficient of $(1.1 \pm 0.1) \times 10^{-9}$ m^2/s while for sample g the value is $(0.94 \pm 0.06) \times 10^{-9}$ m^2/s. Both diffusion coefficients are almost half the value of bulk water, a consequence of the high viscosity of

the solution. Note that the water molecules in the PVOH aqueous solution exchange with the hydroxyl groups of the polymer chain. The relative amount of free (or bulk) water is found after a complete hydration of the PVOH molecules to be about 30 wt% in the solution [120]. At the initial concentration, the sample has enough bulk water to dominate the diffusion process.

The diffusion process is playing an important role in the understanding of the heterogeneities in the dynamics observed during film formation. When the rate of evaporation of the solvent is higher than a certain value, the solute-solvent distribution in the solution system is not homogeneous. In order to have a quantitative insight, an analysis similar to that stated in reference [22] can be made computing the relation between the rate of the vertical convection and the diffusion of the polymer molecules:

$$\varsigma = \frac{\xi \dot{E}}{D} \, ,$$

(6.5)

here ξ is the layer thickness, $\dot{E}$ is the value of the thickness change as shown in figure 6.2 in m/s and D is the diffusion coefficient of the polymer molecules. When $\varsigma \ll 1$, diffusion dominates in the solution and the film remain homogeneous throughout. For the cases when $\varsigma \geq 1$, the difference in concentration cannot be compensated by diffusion, giving rise to a higher polymer concentration in the upper part of the solution. Taking the values of $\dot{E}_1$ from figure 6.2 (c) and (a), one obtains $\varsigma \approx 1.05$ and 1.7 for the sample *f* and *g*, respectively. This means that drying is taking place in a so-called heterogeneous regime.

6.3.2. NMR study at 40 MHz

T_1 and T_2 of freshly prepared PVOH solutions using H_2O and D_2O (labeled as sample *h* and *i*, respectively) are studied at 40 MHz ^{1}H Larmor frequency. Table 6.2 shows T_1 and T_2, respectively, for both short and long components. From the table it is seen that both samples prepared using H_2O and D_2O show two components while in the single-sided NMR scanner at 11.7 MHz shows only one component during T_2 study as described before. T_1 of the single component of the PVOH solution prepared using H_2O at 11.7 MHz has to be compared with the long T_1 component at 40 MHz. The T_1 values of the short component are 41 ms and 50 ms for the sample *h* and *i*, respectively, whereas those are 668 ms and 1115 ms for the long components, respectively. It is seen that the

sample prepared using D_2O as a solvent has a higher long component of T_1 while the short component remains almost the same. HDO molecules formed due to the exchange of labile protons from the –OH group of PVOH chain with the deuterium atom of the solvent may be responsible for the longer T_1 value.

A similar tendency is seen in T_2 values of sample i (see table 6.2) for the long components showing higher value than that of the sample h. T_2 values of the short components match with the results obtained in the single-sided NMR. Generally speaking, all the values of T_2 of the short components of the fresh samples obtained in both instruments are between 10 and 20 ms. Note that the T_2 values of the long components in this study are 390 ms and 688 ms using H_2O and D_2O, respectively, whereas it is around 90 ms for all the samples studied in single-sided NMR (see section 6.3.1). As discussed before, the effective T_2 values obtained in the measurement of single-sided NMR scanner are shorter than the T_2 values obtained at 40 MHz.

Table 6.2: T_1 , T_2 *relaxation times and % relative amount of the short and long components of sample h containing PVOH (MW= 61K) in H_2O and sample i containing PVOH (MW= 61K) in D_2O measured right after preparation at 40 MHz proton Larmor frequency.*

Sample	T_1 study				T_2 study			
	Short (± 1%)		Long (± 1%)		Short (± 1%)		Long (± 1%)	
	T_1 (ms)	Relative amount	T_1 (ms)	Relative amount	T_2 (ms)	Relative amount	T_2 (ms)	Relative amount
h	41	12.7%	668	87.3%	17	15.6%	390	84.4%
i	50	74.6%	1115	25.4%	18	75.8%	688	24.2%

The relative amount of the short and long components calculated from the T_1 and T_2 experiments are given in table 6.2. It is seen that sample h prepared using H_2O as a solvent has higher relative weight of long components in the signal contribution whereas sample i prepared using D_2O as a solvent has higher relative weight of short components. Using water as a solvent, one has to pay attention to the contribution of the ^{1}H of the different sub-systems in order to achieve a correct interpretation of the experimental NMR

results. For this reason, T_1 and T_2 relaxation times are measured in a slightly higher and more homogeneous magnetic field of a proton Larmor frequency of 40 MHz. Generally, in a 25% PVOH-H_2O solution, 21.4% protons from the PVOH molecule containing 4 protons in the repeating unit and 78.6% protons from the H_2O molecule containing 2 protons in each molecule contribute to the NMR signal. Taking into account that 1 proton is exchangeable (labile protons) among 4 protons in the PVOH molecule, further calculation shows that around 16% of the total NMR signal comes from the non-labile protons of the PVOH polymer backbone whereas remaining 84% of the signal is contributed by the H_2O molecule and the labile protons of PVOH molecule. Table 6.2 shows a very similar distribution of relative weight of the short (as well as long) components as obtained from the experimental values of T_1 and T_2 measurements of sample *h* in 40 MHz. In case of PVOH-D_2O solution, 75% non-labile protons from the PVOH backbone chain and 25% labile protons in the solution or in exchange will give rise to the signal. The relative weight obtained from the T_1 and T_2 measurements of sample *i* show around 75% slow decaying and 25% fast decaying components as can be seen in table 6.2. Furthermore from figure 6.8, it is clear that at the first experimental hour the relative amount of the fast decaying components is 15-20% which matches with the estimated value as described above.
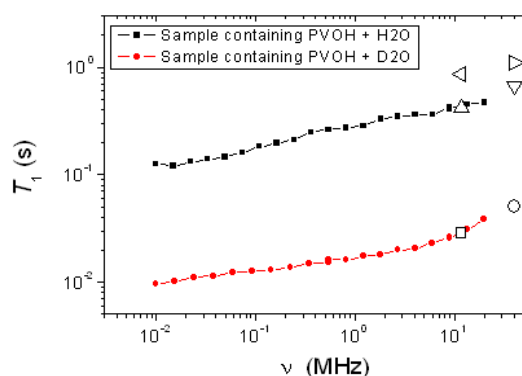
6.3.3. NMR study using Field cycling relaxometer

Figure 6.13: *Frequency dependence of the proton spin-lattice relaxation times of PVOH in H_2O and D_2O systems. The point symbols are showing the results of previous studies at 11.7 MHz and 40 MHz of ^1H Larmor frequency (see figure 6.10, 6.11 and table 6.2).*

Proton T_1 relaxation dispersions at room temperature of freshly prepared sample of PVOH (61K) in H_2O and D_2O (not shown in table 6.1) were investigated using a field-cycling NMR relaxometer in the interval between 10 kHz and 20 MHz. All relaxation curves could be described by monoexponential functions. Both samples exhibit

qualitatively the same dispersion of the T_1 values as shown in figure 6.13. The relaxation mechanism of the polymer in the solution can be explained by the standard Rouse model [128]. Furthermore, the results which are obtained using the same kind of sample in 11.7 MHz (single-sided NMR scanner) and 40 MHz (the Minispec unit) ^{1}H Larmor frequency are complemented by these experiments. It is seen that the average T_1 value obtained at the beginning of the experiment in single-sided NMR for sample *c* (figure 6.10 (b)) matches with the T_1 value of ^{1}H relaxation obtained at 11 MHz ^{1}H Larmor frequency of this experiment for the PVOH in H_2O sample. On the other hand, average T_1 of the fast decaying component (short T_1) of the PVOH in D_2O sample as obtained in figure 6.11 (b) from the single-sided NMR experiment accompanies the result obtained in this study.

6.4. Film characterization

The final films from sample *a*, *b*, *c* and *d* were stored keeping the same environmental conditions of the drying process for two weeks and measured using NMR (only sample *d*) and XRD techniques.

6.4.1. Single-sided NMR study

The fully dried film obtained from sample *d* was stored keeping the same environmental conditions of the drying process for two weeks. In order to explore some limitations and artifacts that can be introduced using single-sided NMR device for the study of the film in its final stage, three CPMG experiments were carried out in the completely formed film using three different pulse separations, namely, 53.5 μs, 56.5 μs and 66.5 μs that define in turn the resolution or layer thickness [31] and keeping the remaining parameters constant (32 echoes, 250 ms repetition time, and 2048 scans).

The measured T_2 values are given in the figure 6.14 as a function of height. The CPMG echo decays are in the order of few hundreds of microseconds and only few echo points are available to be fitted with a mono-exponential function and obtain T_2 relaxation time. Note that only with the shortest pulse separation it is possible to highlight the difference in T_2 at the upper and lower layers of the sample. A longer pulse separation cannot discriminate this effect and shows an apparent homogeneity in the sample inside the experimental error as observed from the T_2 values in different layers. The results obtained in this figure further strengthen the fact that for a pulse separation of 87.5 μs

(used actually to monitor the PVOH solution drying), the instrument is not able to detect the solid-like signal decaying below 100 µs in the case that a solid-like layer appears on the top surface of the sample as described in section 6.3.1.

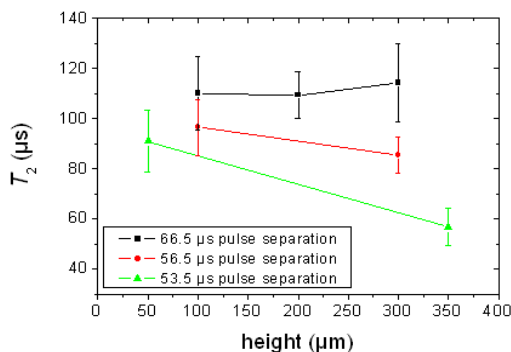**Figure 6.14:** *T_2 constants at different layers of the completely dried film from sample d containing PVOH (MW= 125K) in H_2O. The 180° pulse separation of 66.5 µs, 56.5 µs and 53.5 µs set the resolution to 100 µm, 200 µm and 300 µm respectively [31]. Different numbers of points are needed in each pulse separation to cover the constant film thickness.*

NMR proves clearly, as long as the system has still a sufficiently high mobility that inhomogeneities appear in the solution during practically all the film formation process. During solidification, at advanced evolution times, rigid domains are extended in the entire sample limiting the application of the NMR technique employed in the current work as can be seen in figure 6.14. The heterogeneities observed during evolution will have a signature after solidification, and this is nicely proven in figure 6.16.

6.4.2. XRD study

Powder diffraction spectrum of the raw poly(vinyl alcohol) is shown in the figure 6.15 where the 2θ angles were scanned between 4° and 68°. The X-ray diffractograms of the films obtained from sample *a*, *b*, *c* and *d* are shown in the figure 6.16. All XRD patterns are showing the crystalline structure only. The amorphous contribution has been subtracted [116]. XRD patterns of both the upper and lower parts of all the studied films as well as the raw PVOH sample show a characteristic crystalline peak at a scattering angle of 2θ ~19.5°. The crystal system of PVOH is monoclinic and the (hkl) index for this peak can be calculated using the unit cell parameters for a PVOH crystal [129] which gives (101). From the figure 6.15 it is also seen that the XRD patterns of the raw PVOH sample show a prominent second peak at 2θ ~41° resulting in the (111) plane. However, upper part of each film shows a weak peak at 2θ ~41° which is not distinguishable due
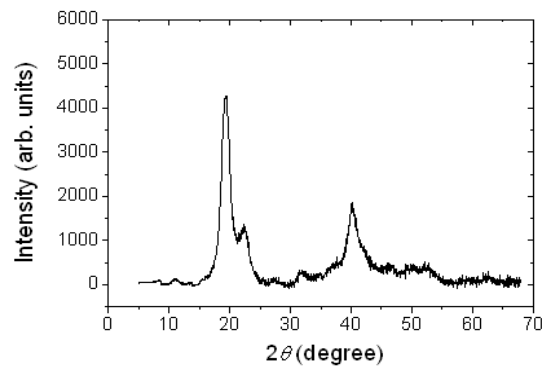
Figure 6.15: *X-ray patterns of the raw poly(vinyl alcohol) sample.*

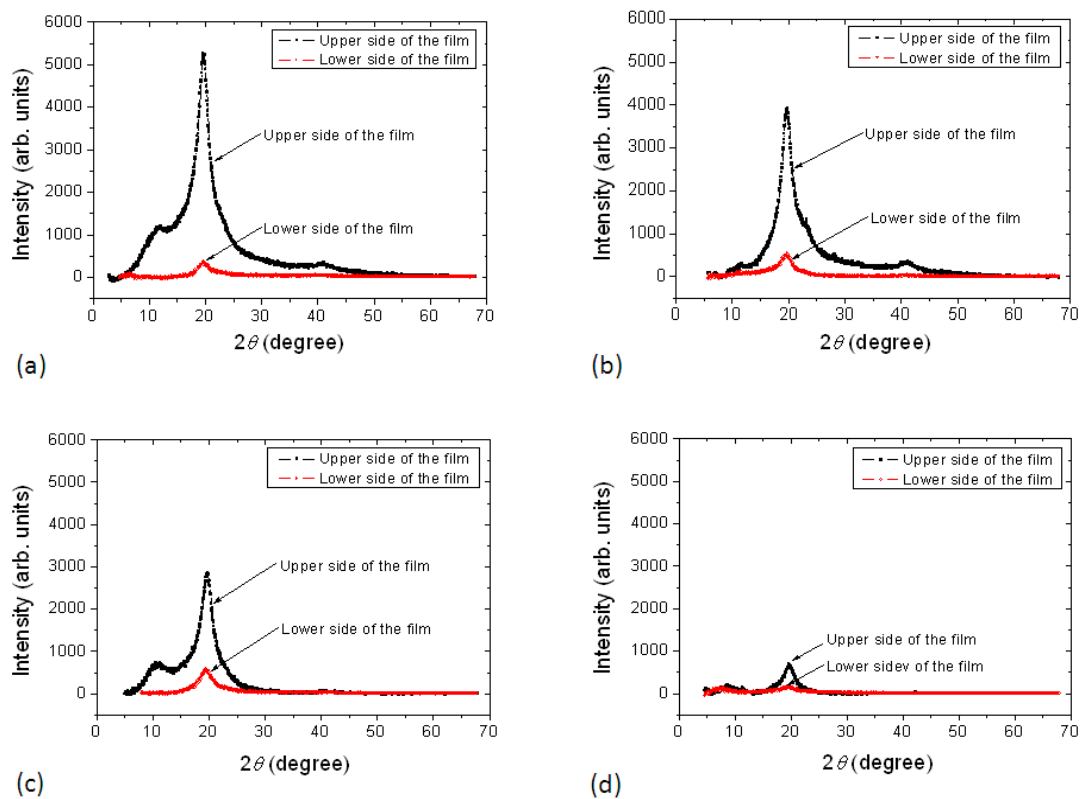**Figure 6.16:** *X-ray patterns of the completely dried film prepared from* **(a)** *sample a containing PVOH (MW= 61K) in D_2O* **(b)** *sample b containing PVOH (MW= 27K) in H_2O* **(c)** *sample c containing PVOH (MW= 61K) in H_2O and* **(d)** *sample d containing PVOH (MW= 125K) in H_2O.*

to low signal to noise ratio in the XRD pattern of the lower part of the films.

We define a parameter which is a simplified indication of the true crystallinity using the following formula [130]:

$$\% \, Crystallinity = \frac{(Total \, Area - Amorphous \, Area) \, of \, the \, XRD \, pattern}{Total \, area \, of \, the \, XRD \, pattern} \times 100 \,, \qquad (6.6)$$

Note that the raw XRD pattern is composed of the superposition of the signal intensity (fraction) from the scattering centres corresponding to the crystalline and amorphous part. The amorphous area is determined from the correction of the baseline for the amorphous region obtained in the lower part of the XRD pattern. To determine the crystallite size present in the upper and lower parts of the final film, Scherrer's equation (Equation 2.15) is applied for the characteristic crystalline peak (at 2θ ~19.5°) and the Scherrer constant k is assumed to be 0.9 which is used for PVOH as can be seen in reference [131].

Table 6.3: *Maximum intensity of the peaks, full width at half maximum (FWHM) at 2θ ~19.5° and % Crystallinity of the upper sides comparing to the lower sides of the films obtained from the sample a containing PVOH (MW= 61K) in D_2O, sample b containing PVOH (MW= 27K) in H_2O, sample c containing PVOH (MW= 61K) in H_2O and sample d containing PVOH (MW= 125K) in H_2O calculated from the XRD patterns shown in figure 6.16.*

Sample	Intensity of the peak at 2θ ~19.5° (arb. units)		FWHM of the peak at 2θ ~19.5° (Δ (2θ))		Crystallinity (%)	
	Upper side	Lower side	Upper side	Lower side	Upper side	Lower side
a	5252.2	368.2	2.57	2.18	78.0	33.2
b	3403.1	434.1	2.21	2.23	64.8	38.1
c	2467.8	523.5	2.43	2.60	55.4	34.2
d	648.3	144.1	2.30	3.76	31.0	22.0

Table 6.3 shows the intensities of the peaks at the scattering angle of 2θ ~19.5°, full width at half maximum (FWHM) of these peaks and the % crystallinity (estimated from Equation 6.6) obtained from the raw XRD patterns. The intensities at both sides of the film are influenced by several factors like roughness and curvature of the sample. The % crystallinity on the other hand is independent of these factors and is the relevant parameter in the context of the present study. Another source of the difference in the peak intensities, besides roughness or curvature at both sides of the sample, is the presence of more crystalline domains in the upper part of the sample [132]. The total crystallinity decreases for the film sample prepared from the PVOH of higher molecular weight. The relative amount of crystallinity (see Table 6.3) further supports this observation. From the FWHM values it is found, using Equation 2.15, that the crystalline domains have a characteristic size in the order of 5 nm in all the samples independent of the side that is

measured and its relative amount of crystallinity. Quantitatively, the upper and lower sides of the films prepared from sample *b*, *c* and *d* have a difference in the relative amount of crystallinity in the range of 10 to 25% (see table 6.3).

Note that sample *a* prepared using PVOH of MW= 25K and D_2O as a solvent shows the highest % of crystallinity which does not match with the molecular weight dependency on the crystallinity observed for the other samples prepared using H_2O as a solvent. For gelatin, it was observed that the preparation of a gel sample using D_2O instead of H_2O has different properties, for example, higher rigidity and melting temperature [133]. To explore the effect of different solvents on the final structure of PVOH film in details could be an interesting topic for the future study.

6.5. Proposed mechanism of PVOH film formation

The mechanism that account for the observed heterogeneities takes place necessarily during film formation. For each of the samples, the T_1 and T_2 values of the both components (figure 6.3, 6.4, 6.10 and 6.11) and the relative amount of the fast decaying components (figure 6.8) decrease gradually with the increment in the sample height and evolution time. At later stage of drying, the $T_{2,short}$ relaxation times cannot be anymore detectable. This indicates a solid-like structure formation in the vicinity of the top surface of the samples. As expressed above, these results point toward the fact that the sample is not homogeneous during drying giving rise to the non-homogeneous structure of the film. The appearance of the single components at the upper part of the samples as shown in the T_2 study (figure 6.3), is a strong evidence that the solid phase is in the process of formation at the corresponding evolution times. The gradual formation of the semi-crystalline polymer domains occurs henceforth from top to bottom of the film. The system undergoes a glass transition and becomes semicrystalline as the evaporation on the top surface increases locally the concentration of polymer to a critical concentration at a certain time. The distribution of the solute (PVOH) concentration in the system [106] arises due to the water evaporation. Right after casting, the water-PVOH solution is a uniform fluid with high viscosity. The drying process regulates water transport in the whole system. At the beginning this transport involves diffusion of water molecules through the continuous solution but at later stages, percolation of water through interstitial spaces between solidified semicrystalline PVOH takes place. The gradient of the solvent and solute concentrations [134] induced by evaporation [11], [106] generates a net flux of water in the direction of the evaporation front causing a difference in concentration. Diffusion processes will tend to reestablish a uniform concentration, but the slow diffusivity

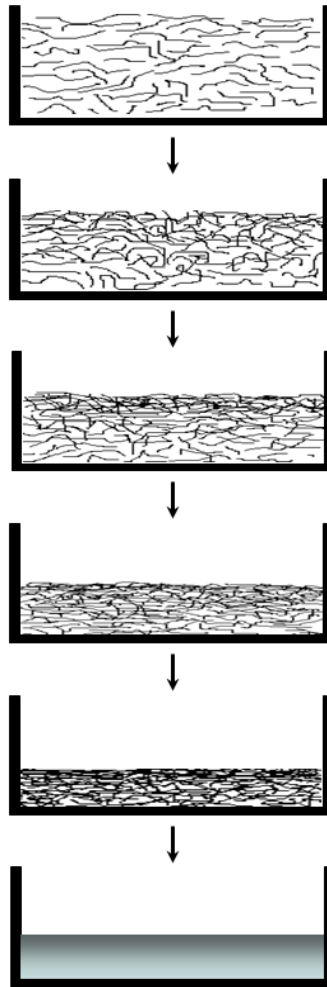of the polymers prevents any equilibration in the time scale of the total film formation process.

Figure 6.17: *Illustration of the poly(vinyl alcohol) solution system at different drying times. The evolution time increases from top to bottom.*

When a concentration gradient is induced, provided that there is enough mobility in the system, it will remain at advanced times where the fluid system becomes highly viscous. The solidification phase transition then will reflect the concentration inhomogeneity.

6.6. Conclusions

The film formation of PVOH of different molecular weights in water solution and the final films obtained in the course of time were studied by NMR relaxation and X-ray diffractometry, respectively. The shrinking rate was followed by NMR imaging with a single sided NMR profiler. Despite the fact that a considerable amount of NMR signal is generated from the protons in the solution (water) for the most of samples studied, the

results are in a complete agreement with the case where D_2O is used as a solution instead. As mentioned above, the detection of a "skin-layer" using this single-sided scanner is difficult. However, the remarkable fact in this work by NMR is the evidence of a gradual slowing down of the molecular dynamics in the direction of the evaporating surface. This is indicated by the two experimental parameters T_1 and T_2.

By the determination of the relaxation parameters T_1 and T_2 it could be traced out that the effect of the evaporation of the solvent molecules in the dynamics of the solution induces a dynamic heterogeneity of the polymer molecules across the film thickness for all the molecular weights. The local evaporation process taking place at the air-sample interface further influences the migration of polymer chains, inducing differences in concentration along the whole system. The direct consequence is the reduction in the mobility of the polymer chains towards the surface where evaporation takes place. These spatial heterogeneities influence the local dynamical behavior of the system and the profile of relaxation times becomes progressively asymmetric during the evolution time. The shorter relaxation times on the top surface at later stages of film formation indicate the presence of more immobile polymer chains. Once the system has completely solidified below certain water content, the measured T_2 relaxation times reflect the dynamics of the amorphous part (as expressed above, the single sided scanner is not sensitive to solid NMR signals). This reveals that the amorphous domain has different dynamics along the film. Taking into account that more crystallization domains are found on top of the film from the XRD study, together with the fact that the polymer system is well below the glass transition temperature, the dynamics of the amorphous part is restricted by the presence of the crystalline domains in the sense of confinement i.e., there is a geometrical confinement. The effect of the molecular weight on the structure of the films is the formation of more crystalline phase at the top surface in the case that PVOH has the lowest molecular weight. This can be seen in table 6.3, where the ratio of crystallinity between the upper and the lower parts decreases with the increase in molecular weight.

In conclusion, an evidence of heterogeneous dynamical restriction of the amorphous part of the final film by the presence of more crystalline domains is found in the final film along the vertical direction, induced during its formation process and influenced by the molecular weight of the polymer.

Chapter 7

Summary and outlook

If I'd had some set idea of a finish line,
don't you think I would have crossed it years ago?

Bill Gates

During the last few decades, increasing efforts have been paid to the investigation of the biopolymer films for new applications. However, the biopolymer film formation process is still not fully understood, and requires considerable attention. The goal of this thesis has been the study of the film formation of environmentally friendly polymers and their characterization. Two biopolymers, gelatin (from animal origin) and starch (from plant origin), were chosen because of their abundance as well as diversify and promising field of applications. Poly(vinyl alcohol) (PVOH), an environmentally friendly synthetic polymer, having a simple structure compared to gelatin and starch, was studied as well. For each polymer sample, a set of systematic experiments were designed to follow the drying process using low-field single-sided nuclear magnetic resonance (NMR) device.

The remarkable aspect in these experiments is the discrimination of the dynamics among different layers of microscopic resolution that is possible with the technique using single-sided NMR scanner. Time-dependent NMR profiles were measured at different layers of the sample using this scanner. Longitudinal (T_1) and transverse (T_2) relaxation times, which prove directly the dynamics of the system [32], were obtained from the echo-decay for each profile point. X-ray diffraction (XRD) and differential scanning calorimetry (DSC) techniques along with the NMR technique were used to characterize the dried films. The employed methods represent a suitable measure for indicating the residual mobility of the system.

The investigations of the film formation and their characterization on these polymer systems are listed and summarized as below:

- Gelatin solutions were prepared varying the initial concentrations of gelatin (1%, 2% and 10%) in H_2O or D_2O (w/v) followed by casting. Film formation was investigated *in situ* during evaporation of the solvent. It was found that when the gelatin film is approaching the final drying stage, the T_2 values of the sample near the substrate decreases more compared with the value at the vicinity of the air-sample interface. This spatial heterogeneity is also observed in the T_1 values at a comparatively low [1]H Larmor frequency of 11.7 MHz, being sensitive for a reduction in overall molecular mobility. XRD study confirmed that the heterogeneity observed during the film formation persists in the final film [SG 1], [SG 2].

- A solution using 10% gelatin in H_2O (w/v) was prepared. Same amount of sample was cast in a series of Petri dishes and left to evolve under identical conditions. Each sample was subjected to study using high-field NMR and DSC while the film was forming. Development of collagen-like triple helix structure (renaturation) was observed in the course of gelatin film formation as revealed by these studies. It was found that the renaturation process takes place for a short period comparing to the total time of film formation [SG 3].

- Gelatin films were prepared from the solutions of different initial concentrations (1% to 30%) in H_2O (w/v). The films were calibrated at four different relative humidity (20%, 43%, 75% and 90%) conditions. The influence of initial concentration and humidity on the dried gelatin film was investigated. It was found that there is an apparent effect of humidity on the relaxation and thermal properties of the gelatin film which is less pronounced in case of initial concentration [SG 4].

- Film formation process from an aqueous sample of 1% and 5% corn starch (w/v) was successfully studied for the first time using micro camera and single-sided NMR scanner. The dried film was characterized using NMR and XRD techniques. It was found that the molecular mobility of these two samples varied notably at different stages of film formation. At an intermediate stage, a gradual decrease in mobility of 1% starch containing sample towards the air-sample interface was observed although 5% starch containing sample was homogeneous all along the sample height. At a later stage, heterogeneity in the dynamics was observed in both samples showing that the bottom part of the sample is less mobile than the upper part. This effect was more evident in the 5% starch containing sample and

the XRD study confirmed that the structural heterogeneity persists in the final film obtained from this sample [SG 5].

- The film formation out of a concentrated aqueous solution of poly(vinyl alcohol) (PVOH) of different molecular weights subject to solvent evaporation was investigated by means of NMR methods and by XRD of the final, solid film. A dynamic heterogeneity of the polymer molecules across the film thickness was observed after a certain time. This behavior approximately corresponds to a change in evaporation rate, indicated by a pronounced decrease of the film shrinking rate. This work confirms that a pronounced reduction in mobility of the polymer chains is observed towards the air-sample interface; however, the variation remains gradual for the whole accessible drying period and a transition towards a well-defined solid skin is not observed from the NMR relaxation data. Subsequent analysis of the completely dried film by X-ray diffractometry, however, reveals that the crystallinity at the top surface is indeed considerably higher than that at the bottom [SG 6], [SG 7].

The above presented studies open the door to several possibilities for future research. It will be necessary to study the influence of the precipitation of the biopolymer chains on the film formation. It was observed that the profile edges near to the air-sample interface vary with concentrations of the sample which was not fully understood along this work. To explore this occurrence would be a promising approach. Although we have extensively studied the structural heterogeneity of the final dried film obtained from gelatin, starch and PVOH samples using low-field NMR and XRD methods, still there are scopes to explore. For instance, extraction of the thin layers from the upper and lower surfaces of a dried film could be helpful for further characterization of the film and to obtain quantitative information regarding the heterogeneity using solid-state NMR or other techniques. Based on the results obtained in this thesis, preparation and characterization of the multilayer biopolymer film could be a potential approach in future.

Publications by the Author as a part of this work

[SG 1].   S. Ghoshal, C. Mattea and S. Stapf. Inhomogeneity in the drying process of gelatin film formation: NMR microscopy and relaxation study. *Chemical Physics Letters*, 485, 343-347, 2010.

[SG 2].   S. Ghoshal, C. Mattea, P. Denner and S. Stapf. Heterogeneities in gelatin film formation using single-sided NMR. *Journal of Physical Chemistry B*, 114, 16356-16363, 2010. [Won the best paper award of TU Ilmenau 2010]

[SG 3].   S. Ghoshal, C. Mattea and S. Stapf. Gelatin film formation studied by high-field NMR and DSC techniques. (In preparation)

[SG 4].   S. Ghoshal, C. Mattea and S. Stapf. Concentration and humidity effects on gelatin films studied by NMR. (In preparation)

[SG 5].   S. Ghoshal, C. Mattea, P. Denner and S. Stapf. Drying of starch biopolymer: NMR microscopy study. (In preparation)

[SG 6].   S. Ghoshal, P. Denner, S. Stapf and C. Mattea. Structural and dynamical heterogeneities in PVA films induced by evaporation during the formation process. *Chemical Physics Letters*, 515, 231-234, 2011.

[SG 7].   S. Ghoshal, P. Denner, S. Stapf and C. Mattea. Study of film formation of Poly(vinyl alcohol). *Macromolecules*, 45, 1913-1923, 2012.

Bibliography

[1]   F. W. Billmeyer. *Textbook of polymer science.* John Wiley & Sons: New York, 1984.

[2]   D. Feldman and A. Barbalata. *Synthetic Polymers: technology, properties, applications.* Chapman & Hall: London, UK, 1996.

[3]   G. Griffin. *Chemistry and Technology of Biodegradable Polymers.* Springer, 1993.

[4]   A. Gennadios. *Protein-based films and coatings.* CRC Press: Boca Raton, 2002.

[5]   M. A. García, M. N. Martino and N. E. Zaritzky. Microstructural characterization of plasticized starch-based films. *Starch - Stärke*, 52 (4), 118-124, 2000.

[6]   C. S. S. R. Kumar. *Nanostructured thin films and surfaces.* Wiley-VCH: Weinheim, 2010.

[7]   I. Yakimets, S. S. Paes, N. Wellner, A. C. Smith, R. H. Wilson and J. R. Mitchell. Effect of water content on the structural reorganization and elastic properties of biopolymer films: a comparative study. *Biomacromolecules*, 8 (5), 1710–1722, 2007.

[8]   E. Kristo, C. Biliaderis and A. Zampraka. Water vapour barrier and tensile properties of composite caseinate-pullulan films: Biopolymer composition effects and impact of beeswax lamination. *Food Chemistry*, 101 (2), 753–764, 2007.

[9]   D. Thirathumthavorn and S. Charoenrein. Aging effects on sorbitol- and non-crystallizing sorbitol-plasticized tapioca starch films. *Starch - Stärke*, 59 (10), 493–497, 2007.

[10]   J. F. Martucci and R. A. Ruseckaite. Tensile properties, barrier properties, and biodegradation in soil of compression-Molded gelatin-dialdehyde starch films. *Journal of Applied Polymer Science*, 112 (4), 2166–2178, 2009.

[11]   S.-S. Wong, S. A. Altinkaya and S. K. Mallapragada. Understanding the effect of skin formation on the removal of solvents from semicrystalline polymers. *Journal of Polymer Science Part B: Polymer Physics*, 43 (22), 3191–3204, 2005.

[12] J. C. H. Hwa. Mechanism of film formation from latices. Phenomenon of flocculation. *Journal of Polymer Science Part A: General Papers*, 2 (2), 785–796, 1964.

[13] S. Erich, H. Huinink, O. Adan, J. Laven and A. Esteves. The influence of the pigment volume concentration on the curing of alkyd coatings: a 1D MRI depth profiling study. *Progress in Organic Coatings*, 63 (4), 399–404, 2008.

[14] A. F. Routh and W. B. Russel. A process model for latex film formation: limiting regimes for individual driving forces. *Langmuir*, 15 (22), 7762–7773, 1999.

[15] A. Veis. *The macromolecular chemistry of gelatin.* Academic Press: New York, London, 1964.

[16] J. N. BeMiller and R. L. Whistler. *Starch: chemistry and technology.* Academic Press, 2009.

[17] V. Goodship and D. Jacobs. *Polyvinyl alcohol: materials, processing and applications.* Smithers Rapra Technology: Shrewsbury, 2005.

[18] M. O. Ngui and S. K. Mallapragada. Understanding isothermal semicrystalline polymer drying: mathematical models and experimental characterization. *Journal of Polymer Science Part B: Polymer Physics*, 36 (15), 2771–2780, 1998.

[19] M. O. Ngui and S. K. Mallapragada. Mechanistic investigation of drying regimes during solvent removal from poly(vinyl alcohol) films. *Journal of Applied Polymer Science*, 72, 1913–1920, 1999.

[20] M. O. Ngui and S. K. Mallapragada. Quantitative analysis of crystallization and skin formation during isothermal solvent removal from semicrystalline polymers. *Polymer*, 40 (19), 5393–5400, 1999.

[21] S.-S. Wong, S. A. Altinkaya and S. K. Mallapragada. Drying of semicrystalline polymers: mathematical modeling and experimental characterization of poly(vinyl alcohol) films. *Polymer*, 45, 5151–5161, 2004.

[22] E. Ciampi and P. J. McDonald. Skin formation and water distribution in semicrystalline polymer layers cast from solution: a magnetic resonance imaging study. *Macromolecules*, 36 (22), 8398–8405, 2003.

[23] Y.-T. Kim, Y.-S. Hong, R. M. Kimmel, J.-H. Rho and C.-H. Lee. New approach for characterization of gelatin biopolymer films using proton behavior determined by low field 1H NMR spectrometry. *Journal of Agricultural and Food Chemistry*, 55 (26), 10678–10684, 2007.

[24] A. Traoré, L. Foucat and J. P. Renou. 1H NMR studies: dynamics of water in gelatin. *European Biophysics Journal*, 29 (3), 159–164, 2000.

[25] M.-C. Vackier, B. P. Hills and D. N. Rutledge. An NMR relaxation study of the state of water in gelatin gels. *Journal of Magnetic Resonance*, 138 (1), 36–42, 1999.

[26] A. E. Aliev. Solid-state NMR studies of collagen-based parchments and gelatin. *Biopolymers*, 77 (4), 230–245, 2005.

[27] V. Svoboda and B. Y. Liaw. In situ transient study of polymer film growth via simultaneous correlation of charge, mass, and ellipsometric measurements. *Pure and Applied Chemistry*, 80 (11), 2439–2449, 2008.

[28] M. Peura, T. Karppinen, A. Soovre, A. Salmi, M. Tenkanen, E. Hæggström and R. Serimaa. Crystallization and shear modulus of a forming biopolymer film determined by *in situ* x-ray diffraction and ultrasound reflection methods. *Journal of Applied Physics*, 104 (2), 23513, 2008.

[29] Y. Wang, D. Juhué, M. A. Winnik, O. Leung and M. C. Goh. Atomic force microscopy study of latex film formation. *Langmuir*, 8, 760–762, 1992.

[30] A. Fissel, J. Dabrowski and H. J. Osten. Photoemission and ab *initio* theoretical study of interface and film formation during epitaxial growth and annealing of praseodymium oxide on Si(001). *Journal of Applied Physics*, 91, 8986–8991, 2002.

[31] F. Casanova, J. Perlo and B. Blümich. *Single-sided NMR*. Springer, 2011.

[32] A. Abragam. *The principles of nuclear magnetism.* Clarendon Press, Oxford University Press: Oxford, New York, 1961.

[33] P. T. Callaghan. *Principles of nuclear magnetic resonance microscopy*. Clarendon Press, Oxford University Press: Oxford, New York, 1991.

[34] F. A. Bovey, L. Jelinski and P. A. Mirau. *Nuclear magnetic resonance spectroscopy.* Academic Press: San Diego, 1988.

[35] M. H. Levitt. *Spin dynamics: basics of nuclear magnetic resonance.* John Wiley & Sons, 2008.

[36] H. Friebolin. *Basic one- and two-dimensional NMR spectroscopy.* Wiley-VCH: Weinheim, 2005.

[37] R. Macomber. *A complete introduction to modern NMR spectroscopy.* Wiley, 1998.

[38] D. Cullity and S. R. Stock. *Elements of X-ray diffraction.* Prentice Hall: Upper Saddle River, NJ, 2001.

[39] C. Suryanarayana and M. G. Norton. *X-Ray diffraction.* Plenum Press: New York, 1998.

[40] P. Gabbott. *Principles and applications of thermal analysis.* Blackwell Pub.: Oxford, Ames, Iowa, 2008.

[41] J. D. Menczel and R. B. Prime. *Thermal analysis of polymers.* John Wiley: Hoboken, NJ, 2009.

[42] G. Höhne, W. Hemminger and H.-J. Flammersheim. *Differential scanning calorimetry.* Springer: Berlin, New York, 2003.

[43] R. W. Biederman, M. Doyle, R. W. W. Biederman and J. Yamrozik. *The cardiovascular MRI tutorial: lectures and learning.* Lippincott Williams & Wilkins, 2007.

[44] R. Kimmich. *NMR: tomography, diffusometry, relaxometry.* Springer, 1997.

[45] G. N. Ramachandran and C. Ramakrishnan. *Biochemistry of collagen.* Plenum Press: New York, 1976.

[46] J. Bella, B. Brodsky and H. M. Berman. Hydration structure of a collagen peptide. *Structure*, 3, 893–906, 1995.

[47] F. Gul-E-Noor, M. A. Khan, S. Ghoshal, R. Mazid, A. M. S. Chowdhury and R. A. Khan. Grafting of 2-ethylhexyl acrylate with urea on to gelatin film by gamma radiation. *Journal of Macromolecular Science, Part A*, 46 (6), 615–624, 2009.

[48] S.-S. Choi and J. Regenstein. Physicochemical and sensory characteristics of fish gelatin. *Journal of Food Science*, 65, 194–199, 2000.

[49] P. J. A. Sobral, F. C. Menegalli, M. D. Hubinger and M. A. Roques. Mechanical, water vapor barrier and thermal properties of gelatin based edible films. *Food Hydrocolloids*, 15 (4-6), 423–432, 2001.

[50] P. C. Griffith, P. Stilbs, A. M. Howe and T. Cosgrove. A Self-Diffusion Study of the complex formed by sodium dodecyl sulfate and gelatin in aqueous solutions. *Langmuir*, 12 (12), 2884–2893, 1996.

[51] M. N. Belgacem and A. Gandini. *Monomers, polymers and composites from renewable resources.* Elsevier: Amsterdam, London, 2008.

[52] R. Talja. Preparation and characterization of potato starch films plasticized with polyols. *PhD Thesis*, Department of Food Technology, University of Helsinki, 2007.

[53] T. Barsby, A. Donald, P. Frazier and Royal Society of Chemistry (Great Britain) Food Chemistry Group. *Starch: advances in structure and function.* Royal Society of Chemistry, 2001.

[54] P. J. Jenkins and A. M. Donald. The influence of amylose on starch granule structure. *International Journal of Biological Macromolecules*, 17 (6), 315–321, 1995.

[55] S. Jobling. Improving starch for food and industrial applications. *Current Opinion in Plant Biology*, 7 (2), 210–218, 2004.

[56] K. Krogars, O. Antikainen, J. Heinämäki, N. Laitinen and J. Yliruusi. Tablet film-coating with amylose-rich maize starch. *European Journal of Pharmaceutical Science*, 17, 23–30, 2002.

[57] A. Jansson and F. Thuvander. Influence of thickness on the mechanical properties for starch films. *Carbohydrate Polymers*, 56 (4), 499–503, 2004.

[58] R. A. Talja, H. Helén, Y. H. Roos and K. Jouppila. Effect of various polyols and polyol contents on physical and mechanical properties of potato starch-based films. *Carbohydrate Polymers*, 67 (3), 288–295, 2007.

[59] Y. Zhang and J. H. Han. Mechanical and thermal characteristics of pea starch films plasticized with monosaccharides and polyols. *Journal of Food Science*, 71 (2), E 109–118, 2006.

[60] A. Steinbüchel and S. Matsumura. *Miscellaneous biopolymers and biodegradation of synthetic polymers.* Wiley-VCH: Weinheim, Cambridge, 2003.

[61] N. Hodgkinson and M. Taylor. Thermoplastic poly (Vinyl Alcohol) (PVOH). *Materials World*, 8, 24–25, 2000.

[62] L. E. Stephans and N. Foster. Magnetization-transfer NMR analysis of aqueous poly(vinyl alcohol) gels: effect of hydrolysis and storage temperature on network formation. *Macromolecules*, 31 (5), 1644–1651, 1998.

[63] M. Shibayama, H. Kurokawa, S. Nomura, S. Roy, R. S. Stein and W. L. Wu. Small-angle neutron scattering studies on chain asymmetry of coextruded poly(vinyl alcohol) film. *Macromolecules*, 23 (5), 1438–1443, 1990.

[64] C. A. Finch. *Polyvinyl alcohol: developments.* Wiley: Chichester, New York, 1992.

[65] J. L. Valentín, D. López, R. Hernández, C. Mijangos and K. Saalwaächter. Structure of poly(vinyl alcohol) cryo-hydrogels as studied by proton low-field NMR spectroscopy. *Macromolecules*, 42 (1), 263–272, 2009.

[66] J. B. Chang, J. H. Hwang, J. S. Park and J. P. Kim. The effect of dye structure on the dyeing and optical properties of dichroic dyes for PVA polarizing film. *Dyes and Pigments*, 88 (3), 366–371, 2011.

[67] C.-C. Yang and Y.-J. Lee. Preparation of the acidic PVA/MMT nanocomposite polymer membrane for the direct methanol fuel cell (DMFC). *Thin Solid Films*, 517 (17), 4735–4740, 2009.

[68] K. Krogars, J. Heinämäki, M. Karjalainen, J. Rantanen, P. Luukkonen and J. Yliruusi. Development and characterization of aqueous amylose-rich maize starch

dispersion for film formation. *European Journal of Pharmaceutics and Biopharmaceutics*, 56 (2), 215–221, 2003.

[69] B. Blümich, J. Perlo and F. Casanova. Mobile single-sided NMR. *Progress in Nuclear Magnetic Resonance Spectroscopy*, 52 (4), 197–269, 2008.

[70] J. Perlo, F. Casanova and B. Blümich. Profiles with microscopic resolution by single-sided NMR. *Journal of Magnetic Resonance*, 176 (1), 64–70, 2005.

[71] S. Meiboom and D. Gill. Modified Spin-echo method for measuring nuclear relaxation times. *Review of Scientific Instruments*, 29 (8), 688–691, 1958.

[72] O. Neudert. Implementation, optimization and application of unconventional diffusion measurement techniques for single-sided NMR. *Masterarbeit*, Technische Physik, Technische Universität Ilmenau, 2010.

[73] S. Stapf and S. Han. *NMR imaging in chemical engineering.* Wiley-VCH, 2006.

[74] N. Bloembergen. *Nuclear magnetic resonance.* W. A. Benjamin: New York, 1961.

[75] E. L. Hahn. Spin echoes. *Physical Review*, 80 (4), 580–594, 1950.

[76] K. Saalwächter, M. Gottlieb, R. Liu and W. Oppermann. Gelation as studied by proton multiple-quantum NMR. *Macromolecules*, 40 (5), 1555–1561, 2007.

[77] H. Y. Carr and E. M. Purcell. Effects of diffusion on free precession in nuclear magnetic resonance experiments. *Physical Review*, 94 (3), 630–638, 1954.

[78] R. L. Vold, J. S. Waugh, M. P. Klein and D. E. Phelps. Measurement of spin relaxation in complex systems. *The Journal of Chemical Physics*, 48 (8), 3831, 1968.

[79] R. Kimmich and E. Anoardo. Field-cycling NMR relaxometry. *Progress in Nuclear Magnetic Resonance Spectroscopy*, 44 (3-4), 257–320, 2004.

[80] J. L. Gornall and E. M. Terentjev. Concentration-temperature superposition of helix folding rates in gelatin. *Physical Review Letters*, 99 (2), 028304-4, 2007.

[81]   A. Bigi, S. Panzavolta and K. Rubini. Relationship between triple-helix content and mechanical properties of gelatin films. *Biomaterials*, 25 (25), 5675–5680, 2004.

[82] L. Friedman and E. O. Kraemer. The structure of gelatin gels from studies of diffusion. *Journal of the American Chemical Society*, 52 (4), 1295–1304, 1930.

[83] T. Abete, G. Del, D. Serughetti, A. de, M. Djabourov and A. Coniglio. Kinetics of bond formation in cross-linked gelatin gels. *The Journal of Chemical Physics*, 125 (17), 174903 (7 pages), 2006.

[84] I. Yakimets, N. Wellner, A. C. Smith, R. H. Wilson, I. Farhat and J. Mitchell. Mechanical properties with respect to water content of gelatin films in glassy state. *Polymer*, 46 (26), 12577–12585, 2005.

[85] C.-A. Dai and M.-W. Liu. The effect of crystallinity and aging enthalpy on the mechanical properties of gelatin films. *Materials Science and Engineering: A*, 423 (1-2), 121–127, 2006.

[86] C.-A. Dai, Y.-F. Chen and M.-W. Liu. Thermal properties measurements of renatured gelatin using conventional and temperature modulated differential scanning calorimetry. *Journal of Applied Polymer Science*, 99 (4), 1795–1801, 2006.

[87] B. P. Hills. The proton exchange cross-relaxation model of water relaxation in biopolymer systems. *Molecular Physics*, 76 (3), 509–523, 1992.

[88] J. Rottstegge, B. Traub, M. Wilhelm, K. Landfester, C. Heldmann and H. W. Spiess. Investigations on the film-formation process of latex dispersions by solid-state NMR spectroscopy. *Macromolecular Chemistry and Physics*, 204 (56), 787–802, 2003.

[89] J. Mallégol, J.-P. Gorce, O. Dupont, C. Jeynes, P. J. McDonald and J. L. Keddie. Origins and effects of a surfactant excess near the surface of waterborne acrylic pressure-sensitive adhesives. *Langmuir*, 18 (11), 4478–4487, 2002.

[90] H. B. Bensusan and S. O. Nielsen. The deuterium exchange of peptide-group hydrogen atoms during the gelatin → collagen-fold transition. *Biochemistry*, 3 (9), 1367–1377, 1964.

[91] P. H. von Hippel and W. F. Harrington. Enzymic studies of the gelatin → collagen-fold transition. *Biochimica et Biophysica Acta*, 36 (2), 427–447, 1959.

[92]   J. L. Gornall and E. M. Terentjev. Universal kinetics of helix-coil transition in gelatin. *Physical Review E,* 77 (3), 031908-8, 2008.

[93]   P. J. Flory and E. S. Weaver. Helix - coil transitions in dilute aqueous collagen solutions. *Journal of the American Chemical Society*, 82 (17), 4518–4525, 1960.

[94]   D. Achet and X. He. Determination of the renaturation level in gelatin films. *Polymer*, 36 (4), 787–791, 1995.

[95]   W. F. Harrington and N. V. Rao. Collagen structure in solution. I. Kinetics of helix regeneration in single-chain gelatins. *Biochemistry*, 9 (19), 3714–3724, 1970.

[96]   L. Guo, R. H. Colby, C. P. Lusignan and A. M. Howe. Physical gelation of gelatin studied with rheo-optics. *Macromolecules*, 36 (26), 10009–10020, 2003.

[97]   K. V. R. Chary and G. Govil. *NMR in biological systems: from molecules to human.* Springer: Dordrecht, Netherlands, 2008.

[98]   J. Keeler. *Understanding NMR spectroscopy.* John Wiley and Sons: Chichester, U.K, 2010.

[99]   D. Massiot, F. Fayon, M. Capron, I. King, S. Le Calvé, B. Alonso, J.-O. Durand, B. Bujoli, Z. Gan and G. Hoatson. Modelling one- and two-dimensional solid-state NMR spectra. *Magnetic Resonance in Chemistry*, 40 (1), 70–76, 2002.

[100]   A. Jäger, G. E. Schaumann and M. Bertmer. Optimized NMR spectroscopic strategy to characterize water dynamics in soil samples. *Organic Geochemistry*, 42 (8), 917–925, 2011.

[101]   J. P. Busnel, E. R. Morris and S. B. Ross-Murphy. Interpretation of the renaturation kinetics of gelatin solutions. *International Journal of Biological Macromolecules*, 11 (2), 119–125, 1989.

[102]   M. Djabourov and P. Papon. Influence of thermal treatments on the structure and stability of gelatin gels. *Polymer*, 24 (5), 537–542, 1983.

[103]   B. Wunderlich. *Thermal analysis of polymeric materials.* Springer: Berlin, 2005.

[104] M. Itoh, Y. Okawa, H. Kobayashi, T. Ohno, Y. Okamoto and T. Katoh. The effect of the thermal history on the gelation of gelatin solution. *Journal of Photography Science*, 42, 14-17, 1994.

[105] F. Badii, C. Martinet, J. R. Mitchell and I. A. Farhat. Enthalpy and mechanical relaxation of glassy gelatin films. *Food Hydrocolloids*, 20 (6), 879–884, 2006.

[106] A. Kabalnov and H. Wennerström. Diffusion in evaporating solutions. *Soft Matter*, 5 (23), 4712–4718, 2009.

[107] T. Brand, S. Richter and S. Berger. Diffusion NMR as a new method for the determination of the gel point of gelatin. *The Journal of Physical Chemistry B*, 110 (32), 15853–15857, 2006.

[108] A. Veis, J. Anesey and J. Cohen. The long range reorganization of gelatin to the collagen structure. *Archives of Biochemistry and Biophysics*, 94 (1), 20–31, 1961.

[109] C. Peña, K. de La Caba, A. Eceiza, R. Ruseckaite and I. Mondragon. Enhancing water repellence and mechanical properties of gelatin films by tannin addition. *Bioresource Technology*, 101 (17), 6836–6842, 2010.

[110] J. F. Robyt. *Essentials of carbohydrate chemistry.* Springer: New York, 1998.

[111] S. G. Ring. Some studies on starch gelation. *Starch/Stärke*, 37 (3), 80–83, 1985.

[112] P. J. Jenkins and A. M. Donald. Gelatinisation of starch: a combined SAXS/WAXS/DSC and SANS study. *Carbohydrate Research*, 308 (1–2), 133–147, 1998.

[113] K. Tananuwong and D. S. Reid. Differential scanning calorimetry study of glass transition in frozen starch gels. *Journal of Agricultural and Food Chemistry*, 52 (13), 4308–4317, 2004.

[114] P. Chatakanonda, S. Varavinit and P. Chinachoti. Relationship of gelatinization and recrystallization of cross-linked rice to glass transition temperature. *Cereal Chemistry Journal*, 77 (3), 315–319, 2000.

[115] M. J. Tizzotti, M. C. Sweedman, D. Tang, C. Schaefer and R. G. Gilbert. New 1 H NMR procedure for the characterization of native and modified food-grade starches. *Journal of Agricultural and Food Chemistry*, 59 (13), 6913–6919, 2011.

[116] S. Park, J. O. Baker, M. E. Himmel, P. A. Parilla and D. K. Johnson. Cellulose crystallinity index: measurement techniques and their impact on interpreting cellulase performance. *Biotechnology for Biofuels*, 3 (1), 1–10, 2010.

[117] P. Le Bail, H. Bizot and A. Buléon. 'B' to 'A' type phase transition in short amylose chains. *Carbohydrate Polymers*, 21 (2-3), 99–104, 1993.

[118] M. Zhai, L. Zhao, F. Yoshii and T. Kume. Study on antibacterial starch/chitosan blend film formed under the action of irradiation. *Carbohydrate Polymers*, 57 (1), 83–88, 2004.

[119] M. M. Green, G. Blankenhorn and H. Hart. Which starch fraction is water-soluble, amylose or amylopectin? *Journal of Chemical Education*, 52 (11), 729–730, 1975.

[120] R. M. Hodge, T. J. Bastow, G. H. Edward, G. P. Simon and A. J. Hill. Free volume and the mechanism of plasticization in water-swollen poly(vinyl alcohol). *Macromolecules*, 29 (25), 8137–8143, 1996.

[121] Y. Satokawa and T. Shikata. Hydration structure and dynamic behavior of poly(vinyl alcohol)s in aqueous solution. *Macromolecules*, 41 (8), 2908–2913, 2008.

[122] Y. E. Shapiro. ^{1}H NMR self-diffusion study of morphology and structure of polyvinyl alcohol cryogels. *Journal of Colloid and Interface Science*, 212 (2), 453–465, 1999.

[123] J.-M. Petit and X. X. Zhu. ^{1}H and ^{13}C NMR study on local dynamics of poly(vinyl alcohol) in aqueous solutions. *Macromolecules*, 29 (6), 2075–2081, 1996.

[124] J.-M. Petit, X. X. Zhu and P. M. Macdonald. Solute probe diffusion in aqueous solutions of poly(vinyl alcohol) as studied by pulsed-gradient spin-echo NMR spectroscopy. *Macromolecules*, 29 (1), 70–76, 1996.

[125] N. A. Peppas. Turbidimetric studies of aqueous poly(vinyl alcohol) solutions. *Die Makromolekulare Chemie*, 176 (11), 3433–3440, 1975.

[126] H. Yang, R. Cheng, H. Xie and Z. Wang. The role of solvation on the conformational change during repeated freezing–thawing treatment to an extremely dilute aqueous solution of poly(vinyl alcohol). *Polymer*, 46 (18), 7557–7562, 2005.

[127]   M. Doi and S. F. Edwards. *The theory of polymer dynamics.* The Clarendon Press, Oxford University Press: New York, 1986.

[128]   R. Kimmich and N. Fatkullin. Polymer chain dynamics and NMR. *Advances in Polymer Science*, 170, 1–113, 2004.

[129]   C. W. Bunn. Crystal structure of polyvinyl alcohol. *Nature*, 161 (4102), 929–930, 1948.

[130]   B. B. He. *Two-dimensional X-ray diffraction.* John Wiley & Sons, 2011.

[131]   T. Miyazaki, A. Hoshiko, M. Akasaka, M. Sakai, Y. Takeda and S. Sakurai. Structure model of a poly(vinyl alcohol) film uniaxially stretched in water and the role of crystallites on the stress−strain relationship. *Macromolecules*, 40 (23), 8277–8284, 2007.

[132]   R. Ricciardi, F. Auriemma, C. de Rosa and F. Lauprêtre. X-ray diffraction analysis of poly(vinyl alcohol) hydrogels, obtained by freezing and thawing techniques. *Macromolecules*, 37 (5), 1921–1927, 2004.

[133]   D. Oakenfull and A. Scott. Gelatin gels in deuterium oxide. *Food Hydrocolloids*, 17, 207–210, 2003.

[134]   W. B. Krantz, R. J. Ray, R. L. Sani and k. J. Gleason. Theoretical study of the transport processes occurring during the evaporation step in asymmetric membrane casting. *Journal of Membrane Science*, 29 (1), 11–36, 1986.

Acknowledgements

Curriculum Vitae

Personal Data

- **Name: SUSHANTA GHOSHAL**
- **Nationality:** Bangladeshi
- **Place of Birth:** Dhaka, Bangladesh
- **Date of Birth:** 31.01.1980
- **Religion:** Hindu
- **Marital status and Sex:** Single and Male
- **E-mail:** sushanta.ghoshal@tu-ilmenau.de, sushanta@daad-alumni.de
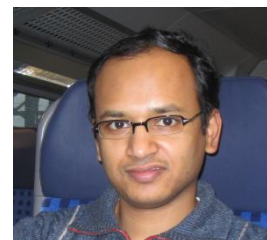
Education

Ilmenau University of Technology, Ilmenau, Germany
Ph. D. (Dr. rer. nat.)
October 2008 – March 2012
Thesis Supervisor: Prof. Dr. Siegfried Stapf.
Thesis Topic: Study of polymer film formation and their characterization using NMR, XRD and DSC.
Dissertation Date: 7th March, 2012.

University of Dhaka, Dhaka, Bangladesh
M. S. in Applied Chemistry and Chemical Technology, with thesis
June 2007
Thesis Topic: Modification of lacca (shellac) biodegradable film by grafting of acrylic monomers using gamma radiation process.

University of Dhaka, Dhaka, Bangladesh
B. Sc. (Honors) in Applied Chemistry and Chemical Technology
June 2005

Awards

- German Academic Exchange Service (DAAD) Scholarship, 2008-2012
- Best Paper Award of the Ilmenau University of Technology, 2010
- Lindau Nobel Laureates Meeting Fellowship, 2010
- Robert Bosch Fellowship, 2010
- Dhaka University Scholarship, 2005
- Dhaka Board Scholarship, 1997

Peer Reviewed Publications

17. **S. Ghoshal**, C. Mattea and S. Stapf. Concentration and humidity effects on gelatin films studied by NMR. (In preparation)

16. **S. Ghoshal**, C. Mattea, P. Denner and S. Stapf. Drying of starch biopolymer: NMR microscopy study. (In preparation)

15. **S. Ghoshal**, C. Mattea and S. Stapf, Gelatin film formation studied by high-field NMR and DSC techniques. (In preparation)

14. **S. Ghoshal**, P. Denner, S. Stapf and C. Mattea, S*tudy of the formation of Poly (vinyl alcohol) films*. Macromolecules, **45**, 1913-1923 (2012).

13. **S. Ghoshal**, P. Denner, S. Stapf and C. Mattea, *Structural and dynamical heterogeneities in PVA films induced by evaporation during the formation process.* Chemical Physics Letters, **515**, 231-234 (2011).

12. **S. Ghoshal**, C. Mattea, P. Denner and S. Stapf, *Heterogeneities in gelatin film formation using single-sided NMR*. Journal of Physical Chemistry B, **114**, 16356-16363 (2010). [Won the best paper award of TU Ilmenau]

11. **S. Ghoshal**, C. Mattea and S. Stapf, *Inhomogeneity in the drying process of gelatin film formation: NMR microscopy and relaxation study*. Chemical Physics Letters, **485**, 343-347 (2010).

10. **S. Ghoshal**, M. A. Khan, R. A. Khan, F. Gul-E-Noor and A. M. S. Chowdhury, *Study on the thermo-mechanical and biodegradable properties of shellac films grafted with acrylic monomers by gamma radiation*. Journal of Polymers and the Environment, **18(3)**, 216-223 (2010).

9. **S. Ghoshal**, M. A. Khan, F. Gul-E-Noor and R. A. Khan, *Gamma radiation induced biodegradable shellac films treated by acrylic monomer and ethylene glycol*. Journal of Macromolecular Science, Part A: Pure and Applied Chemistry, **46(10)**, 975-982 (2009).

8. M. A. Khan, **S. Ghoshal**, R. A. Khan, S. Pervin and A. I. Mustafa, *Preparation and characterization of jute fiber reinforced shellac biocomposites: effect of additive*. Journal of Chemistry and Chemical Technology, **2(3)**, 231-234 (2008).

7. F. Gul-E-Noor, M. A. Khan, **S. Ghoshal**, R. A. Khan, R. A. Mazid and A. M. S. Chowdhury, *Effect of urea on the mechanical properties of gelatin films photocured with 2-ethylhexyl acrylate*. Journal of Polymers and the Environment, **18(3)**, 224-230 (2010).

6. F. Gul-E-Noor, M. A. Khan, **S. Ghoshal**, R. A. Mazid, A. M. **S.** Chowdhury and R. A. Khan, *Grafting of 2-ethylhexyl acrylate with urea on to gelatin film by gamma radiation*. Journal of Macromolecular Science, Part A: Pure and App. Chemistry, **46(6)**, 615-624 (2009).

5. M. A. Khan, R. A. Khan, Haydaruzzaman, **S. Ghoshal**, M. N. A. Siddiky, M. Saha, *Study on the physico-mechanical properties of starch treated jute yarn reinforced polypropylene composites: effect of gamma radiation*. Journal of Polymer-Plastics Technology and Engineering, **48(5)**, 542-548 (2009).

4. R. Alam, M. A. Khan, R. A. Khan, **S. Ghoshal** and M. I. H. Mondal, *Study on the physico-mechanical properties of photo-cured chitosan films with oligomer and acrylic monomer*. Journal of Polymers and the Environment, **16**, 213-219 (2008).

3. H. U Zaman, M. A. Khan, N. Akter, **S. Ghoshal** and R. A. Khan, *Role of gamma radiation and EGDMA on the physic-mechanical properties of jute fabrics/polypropylene composites*. Polymer Composites, **32**, 1888-1894 (2011).

2. M. Rahim, K. Dey, R. A. Khan, **S. Ghoshal**, A. M. S. Chowdhury et al., *Preparation and characterization of gelatin-based PVA film: effect of gamma radiation*. International Journal of Polymeric Materials, **60**, 1056-1069 (2011).

1. S. Nahar, R. A. Khan, K. Dey, B. Sarker, A. K. Das and **S. Ghoshal**, *Comparative studies of mechanical and interfacial properties between jute and bamboo fiber reinforced polypropylene-based composites*. Journal of Thermoplastic Composite Materials. (On-line, DOI: 10.1177/0892705711404725)

PRESENTAIONS

S. Ghoshal, C. Mattea, P. Denner and S. Stapf. *A comparative study on the film formation of bio- and synthetic polymers using single-sided NMR,* Oral Session, The 11th International Conference on Magnetic Resonance Microscopy, Beijing, China. August, 2011.

S. Ghoshal, C. Mattea, P. Denner and S. Stapf. *Water dynamics in gelatin gels and films: NMR and calorimetric study*. Oral Session, International Symposium on recent advances in NMR applications to materials, Hirschegg, Austria. September, 2010.

S. Ghoshal, C. Mattea, S. Kruber, P. Denner and S. Stapf. *Drying of starch, gelatin and paint: a comparative study*. Poster Session, Magnetic Resonance in Porous Media 2010 - MRPM 10, Leipzig, Germany. September, 2010.

S. Ghoshal, C. Mattea, P. Denner and S. Stapf. *Real time investigation of the film formation of gelatin biopolymer using single-sided low-field NMR relaxometry*. Poster Session, Magnetic Resonance in Porous Media 2010 - MRPM 10, Leipzig, Germany. September, 2010.

S. Ghoshal, C. Mattea and S. Stapf. *Inhomogeneity in the drying process of gelatin film formation: NMR microscopy and relaxation study*. DAAD Exchange Program: PPP Project, State Key Laboratory of Chemical Engineering, Department of Chemical and Biochemical Engineering, Zhejiang University, Hangzhou, P. R. China. May, 2010. [Oral Presentation]

S. Ghoshal, C. Mattea and S. Stapf. *Biopolymer film study by NMR and calorimetric techniques*. Oral Session, 2nd Transylvanian NMR Workshop: "Frontiers of Magnetic Resonance Applications to Nano- and Microscopically Structured Systems", Cluj-Napoca, Cluj, Romania. September, 2009.

S. Ghoshal, C. Mattea and S. Stapf. *Gelatin film formation study by single-sided NMR*. Poster Session, AMPERE NMR School, Zakopane, Tatra, Poland. June, 2009.

S. Ghoshal, M. A. Khan, R. A. Khan and A. I. Mustafa. *Fabrication of jute-shellac green composite: effect of urea*. Oral Session, National Symposium on Advanced Materials, Bangladesh University of Engineering and Technology, Dhaka, Bangladesh. January, 2008.

S. Ghoshal, M. A. Khan, R. A. Khan, F. Gul-E-Noor, Haydaruzzaman and M. Z. I. Mollah. *Synthesis, modification and characterization of thin shellac films using acrylic monomers by gamma radiation*. Poster Session, National Conference cum Workshop on Materials

Science and Technology, Bangladesh University of Engineering and Technology, Dhaka, Bangladesh. December, 2007.

S. Ghoshal, M. A. Khan, A. I. Mustafa, R. A. Khan and F. Gul-E-Noor. *Preparation and characterization of bio-composites made of jute and shellac*. Oral Session, National Conference cum Workshop on Materials Science and Technology, Bangladesh University of Engineering and Technology, Dhaka, Bangladesh. December, 2007.

TEACHING

Ilmenau University of Technology, Ilmenau, Germany
Teaching Assistant, Institute of Physics

Physics Basic Practical for B. Sc. Students, Summer 2010
Physics Basic Practical for B. Sc. Students, Winter 2010/11
Physics Basic Practical for B. Sc. Students, Summer 2011
Physics Seminar, Winter 2011/12

Sushanta Ghoshal
Ilmenau, March 2012